GPO PRICE $ _____

CFSTI PRICE(S) $ _____

Hard copy (HC) 3.00

Microfiche (MF) 1.95

ff 653 July 65

GCA CORPORATION

Bedford, Massachusetts

[redacted]

N67 16515

(ACCESSION NUMBER)	(THRU)
131	1
(PAGES)	(CODE)
CR-81262	30
(NASA CR OR TMX OR AD NUMBER)	(CATEGORY)

FACILITY FORM 602

Prepared for

NATIONAL AERONAUTICS AND SPACE ADMINISTRATION
Headquarters
Washington, D.C. 20546

by

Dr. F. F. Marmo, Project Director and
Principal Investigator

December 1966

EXPERIMENTAL AND THEORETICAL STUDIES IN PLANETARY AERONOMY

Quarterly Progress Report

Covering the Period 17 September
through 30 November 1966

Prepared under Contract No. NASW-1283

TABLE OF CONTENTS

I. INTRODUCTION

This is the seventh Quarterly Progress Report which describes the technical progress from 17 September through 30 November 1966 under NASA Contract No. NASW-1283. Scientific investigations accomplished during the current reporting period resulted in the generation of the following papers submitted and/or accepted for publication in accredited scientific journals and/or GCA Technical Reports, or presented at scientific meetings.

Technical Papers Submitted and/or Accepted for Publication

	Publication
a. Submitted	
The Diurnal Variation of Ionospheric Temperatures (A. Dalgarno, M. B. McElroy, and J.C.G. Walker)	Planet. Space Sci.
Photoabsorption Studies of Discharged Hydrogen (R. B. Cairns and J.A.R. Samson)	Proc. of Phys. Soc.
Vacuum Ultraviolet Research (J.A.R. Samson)	Applied Optics
The Relative Photoelectric Yield and Transmittance of Aℓ Films (R. B. Cairns and J.A.R. Samson)	J. Opt. Soc. Am.
Laboratory Rate Coefficients for Positive Ion-Neutral Reactions in the Ionosphere (P. Warneck)	J. Geophys. Res.
b. Accepted	
Ion Temperatures in the Topside Ionosphere (A. Dalgarno and J.C.G. Walker)	Planet. Space Sci.
Reactions of ^1D Oxygen Atoms III. Ozone Formation in the 1470Å Photolysis of O_2 (P. Warneck and J. O. Sullivan)	J. Chem. Phys.

c. Published

Ionization Potential of O_2 (J.A.R. Samson and R. B. Cairns)	J. Opt. Soc. Am. 56, 769 (1966)
Ionization Potential of Molecular Xenon and Krypton (J.A.R. Samson and R. B. Cairns)	J. Opt. Soc. Am. 56, 1140 (1966)
Gas Analysis by Photoionization Mass Spectrometry (W. Poschenrieder and P. Warneck)	J. Appl. Phys. 37, 2812 (1966)
Total Absorption Cross Sections of CO and CO_2 in the Region 550-200Å (R. B. Cairns and J.A.R. Samson)	J. Opt. Soc. Am. 56, 526 (1966)

Technical Papers Presented at Scientific or Professional Meetings

Charge Transfer Reactions of Argon Ions at Near Thermal Energies (P. Warneck) — Prepared for presentation by P. Warneck (not presented because of illness, but paper will appear in the proceedings of the meeting) at the 19th Annual Gaseous Electronics Conference held at the Atlanta Americana Motor Hotel, Atlanta, Georgia, on October 12-14, 1966.

In Section II, technical summaries are presented on the work performed under the present contract. During the current reporting period, significant progress has been achieved in the following areas:

A. Photochemistry of planetary gases,

B. Theoretical studies,

C. Experimental investigations in the VUV (2000-1000Å) and the EUV (below 1000Å) spectral regions,

D. Planetary aeronomy.

Section III contains other pertinent information regarding presentations of papers at scientific meetings.

In compliance with the requirements of the contract, an integrated tabulation by labor category and grade of total hours expended in the execution of the contract, for the specified work interval, is included in Section IV.

II. SUMMARIES OF TECHNICAL WORK PERFORMED FOR THE PERIOD 17 SEPTEMBER THROUGH 30 NOVEMBER 1966

The technical progress accomplished during the current reporting period is discussed in the present section in four general categories: (A) photochemistry of planetary gases, (B) theoretical studies, (C) experimental investigations in the VUV (2000-1000Å) and the EUV (below 1000Å) spectral regions, and (D) planetary aeronomy.

A. PHOTOCHEMISTRY OF PLANETARY GASES

The detailed technical requirements under the general category of photochemistry of planetary gases are contained in the Statement of Work of the subject contract. Briefly, four scientific areas are specified: (1) photochemistry of planetary gases in the EUV (below 1000Å), (2) investigations of ion-molecule reactions in planetary atmospheres, (3) mass analysis of photoionization products in the VUV (2000 to 1000Å) and the EUV (below 1000Å) spectral regions, and (4) photochemical investigation on the role of minor constituents in the atmospheres of Mars and Venus.

During the current reporting period, active investigations have been conducted under Items (1) and (2), the results of which are discussed below.

1. Photochemistry of Planetary Gases in the EUV (Below 1000Å)

Two sources of difficulty in the conduct of photochemical investigations in the EUV are the general lack of optical windows and the host of problems involved in conjunction with high vacuum systems.

Alternatively, several suitable light sources are available including the helium resonance emission at 584Å and the neon emissions at 736 and 744Å. Previous experience in this laboratory indicates that utilization of microwave power results in highly-efficient excitation processes for the above resonance lines. On the basis of a preliminary investigation, it appears that the photon flux generated in conjunction with a 125-watt microtherm unit amounts to about 10^{15} and possibly as high as 10^{16} photons cm^{-2} sec^{-1}. Appropriate caution must be exercised to exclude higher spectral radiations for $\lambda\lambda > 1000$Å; e.g., the hydrogen Lyman-alpha line at 1216Å (which is a common contaminant in these light sources due to water vapor impurity). Thus, the major remaining experimental problem involves the location and suitable employment of a thin film metallic window which transmits selectively in the region of the rare gas resonance lines. In this regard, it should be recognized that only a select number of materials can be made sufficiently self-supporting to offset the adverse effects of stress, brittleness, etc. Published data suggest that both aluminum and indium thin films possess the desired mechanical characteristics. With respect to the optical properties of aluminum film, an 800Å thick film transmits about 20 percent of the incident radiation at 584Å and less than 5 percent at 740Å. Indium transmits only in the spectral region $\lambda\lambda$ 750 to 1050Å so that the lower wavelength limit is just beyond the two cited neon resonance lines. Additionally, recent investigations indicate that tin and lead transmit in the spectral region containing the two neon resonance lines, although their mechanical characteristics are not as suitable as those of aluminum and indium. Therefore, in the event that

tin or lead films are employed, they would require the mechanical support of a grid structure, thereby introducing a corresponding decrease in transmissivity.

The preliminary EUV photochemical setup is shown schematically in Figure 1. Since completion of the construction of this apparatus is not anticipated until the forthcoming reporting period, detailed discussions of general features and operation are deferred to the subsequent quarterly report.

2. Investigations of Ion-Molecule Reactions in Planetary Atmospheres

Previous laboratory investigations on ion-molecule reactions have demonstrated the feasibility of performing pertinent measurements for a number of planetary gases. In addition, several experimental problems have also been identified such as those described in the previous quarterly report.[1] The incorporation of a number of refinements into the original photoionization-mass spectrometer, ion-molecule reaction apparatus is being considered based on a careful review of the preliminary laboratory results. Accordingly, it is anticipated that a significant delay will be encountered in the resumption of the new laboratory ion-molecule reaction studies.

During the current reporting period, a critical review of past efforts has been performed on ion-molecule reactions involving planetary gases to aid in the definition of the forthcoming experimental program. The results of this critical analysis are presented below.

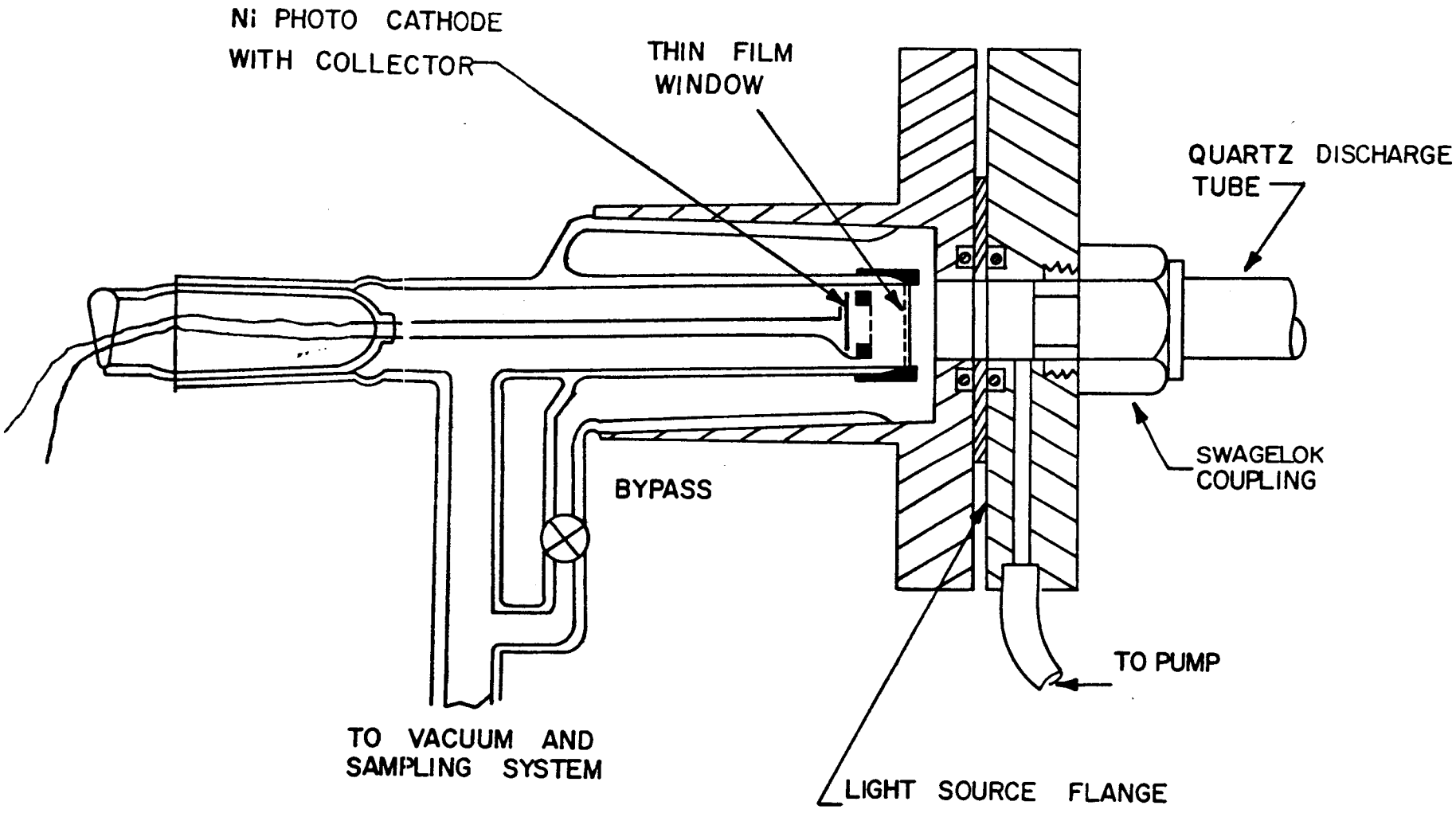

Figure 1. Photochemical setup used in conjunction with extreme ultraviolet light source. Note inserted photoelectric detector.

a. Review of laboratory rate coefficients for positive ion-neutral reactions in planetary ionospheres

It is convenient to discuss the results of the review in terms of reactions pertinent to (1) the Martian ionosphere and (2) the Earth ionosphere.

(1) Positive ion-neutral reactions in the Martian ionosphere

The two major groups which have been involved in the performance of laboratory measurements on positive ion-neutral reactions for gases present in the Martian ionosphere are the ESSA Laboratory (Boulder, Colorado) and the GCA Experimental Physics Laboratory. A summary of selected reactions which are considered to be most pertinent to the Martian ionosphere is presented in Table 1. The corresponding reaction rate coefficients (cm^3 $molecule^{-1}$ sec^{-1}) measured by the two laboratories are also tabulated. It is apparent from this tabular presentation that essential agreement exists in several cases while for a number of important reactions, there are no available data. Additionally, since the GCA data, at least, are considered to be preliminary, the specific areas requiring further careful analysis are clearly indicated.

(2) Positive ion-neutral reactions in the Earth ionosphere

A similar systematic review has been performed for positive ion-neutral reactions in the Earth ionosphere. Although more data are available, it is appropriate to summarize the results for program planning

TABLE 1

MARS IONOSPHERE REACTIONS AND RATE COEFFICIENTS
FROM TWO SOURCES

Reaction	Rate Coefficients (cm^3 $molecule^{-1}$ sec^{-1})	
	GCA	ESSA Group Boulder
$Ar^+ + O_2 \rightarrow O_2^+ + Ar$	1.1×10^{-10}	1.1×10^{-10}
$Ar^+ + CO \rightarrow CO^+ + Ar$	1.2×10^{-10}	0.9×10^{-10}
$Ar^+ + CO_2 \rightarrow CO_2^+ + Ar$	7.0×10^{-10}	7.6×10^{-10}
$Ar^+ + NO \rightarrow NO^+ + Ar$	3.9×10^{-10}	-
$Ar^+ + N_2 \rightarrow N_2^+ + Ar$	0.6×10^{-10}	6×10^{-12}
$O^+ + CO_2 \rightarrow O_2^+ + CO$	-	1.1×10^{-9}
$CO_2^+ + O \rightarrow O_2^+ + CO$	-	-
$CO_2^+ + O \rightarrow O^+ + CO_2$	-	-
$CO_2^+ + O_2 \rightarrow O_2^+ + CO_2$	-	-
$CO^+ + CO_2 \rightarrow CO_2^+ + CO$	-	-
$CO^+ + O_2 \rightarrow O_2^+ + CO$	-	-
$CO^+ + O_2 \rightarrow O^+ + CO_2$	-	-
$CO^+ + O_2 \rightarrow CO_2^+ + O$	-	-
$CO^+ + O \rightarrow O^+ + CO$	-	-
$CO_2^+ + CO_2 \rightarrow O_2^+ + 2\ CO$	-	-
$N_2^+ + CO_2 \rightarrow CO_2^+ + N_2$	9.1×10^{-10}	9.0×10^{-10}

purposes. It has been concluded that a current requirement exists for considerable laboratory investigations of pertinent positive ion-neutral reactions in the Earth ionosphere. The results of this review have been submitted for publication to the Journal of Geophysical Research as a Research Note. Since the results of the review are presented in a highly concise form, the entire note is reproduced below.

Following the initial suggestion by Bates and Massey,[2] the significance of ion-neutral reactions in controlling the abundance of ions in the Earth's ionosphere has been widely discussed in a number of theoretical papers.[3-9] Further indications for the predominant effects of ionic reactions have been provided by actual measurements of ion density profiles with rocket-borne mass spectrometers.[10-12] However, until recently, the relative importance of many reactions in the ionosphere could not be assessed because a detailed knowledge of the individual thermal rate coefficients was either lacking or rather uncertain as a review by Paulson[13] demonstrated. Since then, efforts in several laboratories have resulted in the experimental determination of many of the required rate constant values. This note will present a comparison of the various laboratory results to show that they have improved to the point where a reasonable consistency has been achieved, thereby providing atmospheric scientists with a set of acceptable thermal rate constant values for future ionospheric studies.

Table 2 summarizes the thermal energy laboratory results available at the present time for the reactions of interest to the

TABLE 2

COMPARISON OF ION-NEUTRAL REACTION RATE CONSTANTS* (cm^3 sec^{-1})

	Reaction	Transient Afterglow	Photoionization Mass Spectrometer	Flowing Afterglow
1.	$N_2^+ + O_2 \rightarrow O_2^+ + N_2$	$\sim 2(-10)^c$	$1.1(-10)^b$	$1.0(-10)^a$
2.	$N_2^+ + O_2 \rightarrow NO^+ + NO$	--	$< 3(-14)^{b**}$	--
3.	$N_2^+ + 2N_2 \rightarrow N_4^+ + N_2$	--	$8.5(-29)^b$	--
4.	$N_2^+ + NO \rightarrow NO^+ + N_2$	--	$4.8(-10)^d$	$5(-10)^a$
5.	$N_2^+ + O \rightarrow NO^+ + N$	--	--	$2.5(-10)^e$
6.	$O_2^+ + N_2 \rightarrow NO^+ + NO$	--	$< 3(-15)^{d**}$	$< 1(-15)^{f**}$
7.	$O_2^+ + NO \rightarrow NO^+ + O$	--	$7.7(-10)^d$	$8.0(-10)^a$
8.	$O_2^+ + N \rightarrow NO^+ + O$	--	--	$1.8(-10)^a$
9.	$O^+ + O_2 \rightarrow O_2^+ + O$	$2.0(-11)^j$	$2.0(-11)^g$	$4.0(-11)^h$
10.	$O^+ + N_2 \rightarrow NO^+ + O$	$2.4(-12)^j$	$4.6(-12)^g$	$3.0(-12)^i$
11.	$O^+ + NO \rightarrow NO^+ + O$	--	--	$\leq 2.4(-11)^a$
12.	$N^+ + O_2 \rightarrow NO^+ + O$	$\sim 5(-10)^c$	$1.6(-10)^g$	$\leq 5(-10)^a$
13.	$N^+ + O_2 \rightarrow O_2^+ + N$	--	$4.5(-10)^g$	$5\text{-}10(-10)^a$
14.	$N^+ + NO \rightarrow NO^+ + N$	--	$6.5(-10)^g$	$8.0(-10)^a$

*Numbers in parentheses indicate powers of ten.

**The previous upper limit [Galli *et al.* (Ref. 19)] was 2(-13).

a. [Goldan *et al.* (Ref. 16)]
b. [Warneck (Ref. 17)]
c. [Fite *et al.* (Ref. 20)]
d. [Warneck (Ref. 21)]
e. [Ferguson *et al.* (Ref. 22)]
f. [Ferguson (Ref. 8)]
g. [Warneck (Ref. 23)]
h. [Fehsenfeld *et al.* (Ref. 24)]
i. [Fehsenfeld *et al.* (Ref. 25)]
j. [Copsey *et al.* (Ref. 26)]

E and F_1 regions. No detailed discussion of these data is given here since the present intent is to stress the close agreement of the individual rate coefficient values. It is particularly significant that three distinctly different experimental methods were applied in deriving the data: (a) the transient afterglow method first described by Dickinson and Sayers,[14] (b) the steady-state afterglow flow method developed by the ESSA Laboratory at Boulder,[15,16] and (c) the photoionization mass spectrometer technique devised in this laboratory.[17,18] The data in Table 2 are grouped according to these methods. Some of the author's results are published here for the first time and will be discussed more fully in a later paper. Additional scattered results are available from electron impact mass spectrometer experiments, but these refer usually to nonthermal conditions and only the upper limit values obtained by Galli et al.[19] for Reactions (2) and (6) are considered here. As a basis for comparison, a brief description of the three principally employed methods appears desirable.

In the steady-state afterglow system, a fast flow of helium is discharged to produce He^+ and $He(2^3S)$, and these species are converted to the primary ions of interest by rapid reactions with nitrogen or oxygen, admixed through a nozzle into the flow tube behind the discharge. Secondary reactions with gases added through a second inlet further downstream are observed with a quadrupole mass spectrometer located at the end of the tube. The reaction time is given by the ratio of distance between neutral gas inlet and sampling point to the prevalent linear gas flow rate. Total pressures are in the vicinity of one torr.

The transient afterglow method differs from the flowing afterglow technique in that the decay of the ion concentration following the application of a brief discharge pulse is observed directly as a function of time over several hundred microseconds with a fast response mass spectrometer attached to the vessel containing the ionized gas. A helium buffer is frequently applied to minimize diffusion losses of ions to the walls of the container.

The photoionization mass spectrometer technique has been implemented only recently and a detailed description of the method will be published elsewhere.[17] However, the basic instrumentation has been described by Poschenrieder and Warneck.[18] Primary ions are formed in the ionization box of a mass spectrometer by a beam of vacuum ultraviolet radiation, and these ions undergo reactions as they travel toward the sampling orifice in the presence of a constant repeller field. Through the use of photoionization instead of the more commonly employed electron impact mode of ion formation, one achieves a convenient control of the primary processes by a choice of the ionizing wavelength. In addition, a new technique has been employed for the determination of ion residence times in the box, using a pulsed light source, so that reaction rate constants can be obtained. The pressure range is 0.01 to 0.2 torr. From considerations of the energy and the motion of the reaction ions at low repeller fields and a critical analysis of ion pulse shapes, it can be shown that the reactions proceed in the thermal energy range, corresponding to ion temperatures 400 to 2000^{o}K.

Table 2 demonstrates the good agreement obtained for the individual rate constants by the three experimental methods. In the majority of cases, the values differ by less than a factor of two, and for Reactions (1), (4), (7), and (14) the agreement is much better. Accordingly, confidence can be placed also in those values which have been determined by only one method so far, although their redetermination certainly would be desirable. The upper limit values for Reactions (2) and (6) have been lowered by at least an order of magnitude from their previous upper limits established by Galli et al.[19] The important reactions, (9) and (10), have been under discussion for some time. For Reaction (9), the photoionization technique gives better agreement with the transient afterglow method than with the flowing afterglow method, but the over-all agreement is still satisfactory. For Reaction (10), the previous value obtained with the transient afterglow method[27] was about one order of magnitude greater than that obtained with the other two methods, but the more recent unpublished results by the same group[26] for single discharges in place of repetitive discharge operation gave values substantially in agreement with the other two. Finally, Schmeltekopf et al.[28] have recently shown that the rate of Reaction (10) increases for vibrationally-excited N_2 as a function of vibrational temperature. An extrapolation toward 300°K yields $k_{10} \approx 2 \times 10^{-12}$ cm^3/sec in agreement with their earlier determination for the reaction under thermal conditions and with the values given by the other two methods. In summary, then, it appears that a satisfactory set of rate constant values for these atmospheric reactions has been established.

B. THEORETICAL STUDIES

The specific requirements under the general category of theoretical studies are contained in the Statement of Work of the subject contract. Briefly, four scientific areas are specified: (1) cooling rates of hot electrons in the Earth's atmosphere, (2) the role of ion cooling and thermal conduction on electron temperatures in the Earth's atmosphere, (3) electron impact studies on the diurnal variation of observed airglow, and (4) theoretical investigation of photon scattering by atmospheric gases. During the present reporting period, an active investigation has been performed on Item (1). Since this item has now been completed, the results have been submitted for publication in Planetary and Space Sciences in a paper entitled "The Diurnal Variation of Ionospheric Temperatures" by A. Dalgarno et al. As such, the material will not be published as a GCA Technical Report so that considerable delay is anticipated before the complete results are available in published form. Accordingly, the full text of the original article is reproduced below.

1. The Diurnal Variation of Ionospheric Temperatures

a. Introduction

It has been established by direct measurements using probes carried on rockets and satellites[29-35] and by ground-based measurements using incoherent backscatter techniques[36-40] that the electron temperature exceeds the neutral particle temperature at altitudes above about 120 km during the day. Measurements using the backscatter technique also show that the ion temperature exceeds the neutral

particle temperature above about 300 km and apparently tends toward the electron temperature at great heights.

Theoretical studies[41-43] indicate that solar ultraviolet radiation provides a major heat source. The ambient electrons are heated by elastic collisions with fast photoelectrons, and the positive ions are heated by collisions with hot ambient electrons.[42,44] The early theoretical studies assumed a local equilibrium. Hanson[42] noted, however, that thermal conduction in the electron gas would modify the temperature profile at great heights, and Geisler and Bowhill[45] confirmed the importance of conduction.

This study was stimulated by the availability of detailed observational data on the diurnal variations of electron and ion temperatures. Simultaneous measurements of electron density are also available and afford an opportunity of extensively testing the theoretical model. In particular, it should be possible to determine whether additional heat sources are required.

b. Model atmospheres

To represent the structure and variations in the neutral component of the upper atmosphere, we adopt the model of Jacchia[46] with a trivial modification[47] which allows us to use the analytic expressions introduced by Bates[48] (cf. Stein and Walker, Ref. 49). Jacchia's model reflects satellite drag data on solar cycle, short period solar activity, semi-annual, diurnal, and geomagnetic activity variations in atmospheric density, as shown in Table 3.

TABLE 3

Neutral atmosphere model, July 1963

Altitude km	T_n °K	$n(N_2)$ cm^{-3}	$n(O_2)$ cm^{-3}	$n(O)$ cm^{-3}	$n(He)$ cm^{-3}
120	355	4.00(11)*	7.50(10)	7.60(10)	3.40(7)
140	516	6.44(10)	9.81(9)	2.28(10)	2.21(7)
160	605	1.78(10)	2.32(9)	1.02(10)	1.71(7)
180	655	6.10(9)	6.87(8)	5.35(9)	1.41(7)
200	683	2.30(9)	2.27(8)	3.01(9)	1.21(7)
220	699	9.18(8)	7.96(7)	1.76(9)	1.05(7)
240	708	3.77(8)	2.89(7)	1.06(9)	9.17(6)
270	715	1.03(8)	6.54(6)	5.00(8)	7.58(6)
300	718	2.87(7)	1.52(6)	2.41(8)	6.31(6)
400	720	4.57(5)	1.34(4)	2.26(7)	3.48(6)
500	720	8.24(3)	1.36(2)	2.28(6)	1.96(6)
600	720	1.67(2)	1.58	2.45(5)	1.13(6)
			1600 EST		
120	355	4.00(11)	7.50(10)	7.60(10)	3.40(7)
140	564	6.34(10)	9.76(9)	2.17(10)	2.11(7)
160	681	1.91(10)	2.55(9)	1.01(10)	1.64(7)
180	746	7.26(9)	8.54(8)	5.60(9)	1.37(7)
200	782	3.06(9)	3.20(8)	3.35(9)	1.18(7)
220	802	1.36(9)	1.28(8)	2.08(9)	1.04(7)
240	814	2.26(8)	5.26(7)	1.33(9)	9.25(6)
270	822	2.02(8)	1.44(7)	6.92(8)	7.83(6)
300	826	6.66(7)	2.06(6)	3.67(8)	6.67(6)
400	829	1.82(6)	6.65(4)	4.69(7)	3.98(6)
500	829	5.58(4)	1.24(3)	6.39(6)	2.42(6)
600	829	1.89(3)	2.58(1)	9.23(5)	1.49(6)

*$4.00(11) \equiv 4.00 \times 10^{11}$

TABLE 3 (Continued)

Neutral atmosphere model, July 1963

Altitude km	T_n °K	$n(N_2)$ cm^{-3}	$n(O_2)$ cm^{-3}	$n(O)$ cm^{-3}	$n(He)$ cm^{-3}
		1900 EST			
120	355	4.00(11)	7.50(10)	7.60(10)	3.40(7)
140	548	6.38(10)	9.78(9)	2.21(10)	2.14(7)
160	655	1.88(10)	2.48(9)	1.01(10)	1.66(7)
180	715	6.89(9)	7.99(8)	5.53(9)	1.38(7)
200	749	2.81(9)	2.88(8)	3.24(9)	1.19(7)
220	767	1.21(9)	1.10(8)	1.98(9)	1.04(7)
240	778	5.36(8)	4.37(7)	1.24(9(	9.23(6)
270	786	1.64(8)	1.13(7)	6.27(8)	7.76(6)
300	789	5.14(7)	3.01(6)	3.23(8)	6.56(6)
400	792	1.19(6)	4.06(4)	3.75(7)	3.83(6)
500	792	3.10(4)	6.27(2)	4.65(6)	2.27(6)
600	792	8.94(2)	1.09(1)	6.14(5)	1.37(6)

For the neutral particle composition at 120 km, the number densities used by Jacchia,

$$n(O_2|120) = 7.5 \times 10^{10}\ cm^{-3} \quad ; \quad n(N_2|120) = 4.0 \times 10^{11}\ cm^{-3}$$

$$n(O|120) = 7.6 \times 10^{10}\ cm^{-3} \quad ; \quad n(He|120) = 3.4 \times 10^{7}\ cm^{-3} \quad ,$$

are generally consistent with values derived by Hinteregger, Hall, and Schmidtke[50] from ultraviolet attenuation data and with direct mass spectrometric measurements,[35,51-59] except that Jacchia's model contains more nitrogen.

Our calculations refer to a quiet, undisturbed mid-latitude ionosphere in 1963, a period during which solar flux measurements were carried out by Hinteregger, Hall, and Schmidtke[50] and during which electron temperature and density measurements were carried out by Evans.[60]

c. Model ionospheres

The calculations of heat input are sensitive to the ambient electron density. Between 200 km and 700 km, we adopted electron density profiles given by Evans.[60] These data represent mean diurnal variations for April, July, and November 1963. Below 200 km, we adopted similar monthly averages derived by Wright (private communication, 1965) from ionosonde data at Fort Monmouth. Above 700 km, we extrapolated Evans' data, assuming a constant scale height. The detailed electron distributions are given in an appendix.

d. Electron heating

To compute the electron heating rates, we followed the procedures described by Dalgarno, McElroy, and Moffett[43] with one improvement. Dalgarno et al.[43] introduced the simplifying concept of a critical energy which specified the maximum energy transferred by a photoelectron to the ambient electron gas. Electron collisions were assumed negligible above and dominant below this critical energy. In connection with a study of dayglow produced by photoelectron impact,[61] it was necessary to modify the program to take detailed account of all the energy loss processes and, incidentally, to compute the heating rates directly. The more accurate procedure showed that the critical energy concept underestimated the heating rate by about a factor of two. In predicting the heating rate, we included the contribution from metastable species and from vibrationally-excited nitrogen molecules.[43]

The solar fluxes were taken from the tabulation of Hinteregger et al.[50] Their data are strongly weighted by measurements taken in July 1963. The absorption cross sections for O_2 and N_2 were also taken from Hinteregger et al.[50] For atomic oxygen, we used the absorption cross sections computed by Dalgarno, Henry, and Stewart.*[62]

The diurnal variation of the heating rate, $Q_{e(z)}$, at various altitudes, z, is shown in Figure 2, and more detailed results are tabulated in the appendix. The asymmetry about noon is largely due to the asymmetry in the neutral particle atmosphere, but some effect also occurs because of the variation in electron density.

*Their calculations ignore autoionizing transitions. The recent experiments of Samson and Cairns[63] indicate that the theory underestimates the cross sections at selected wavelengths by factors of about two.

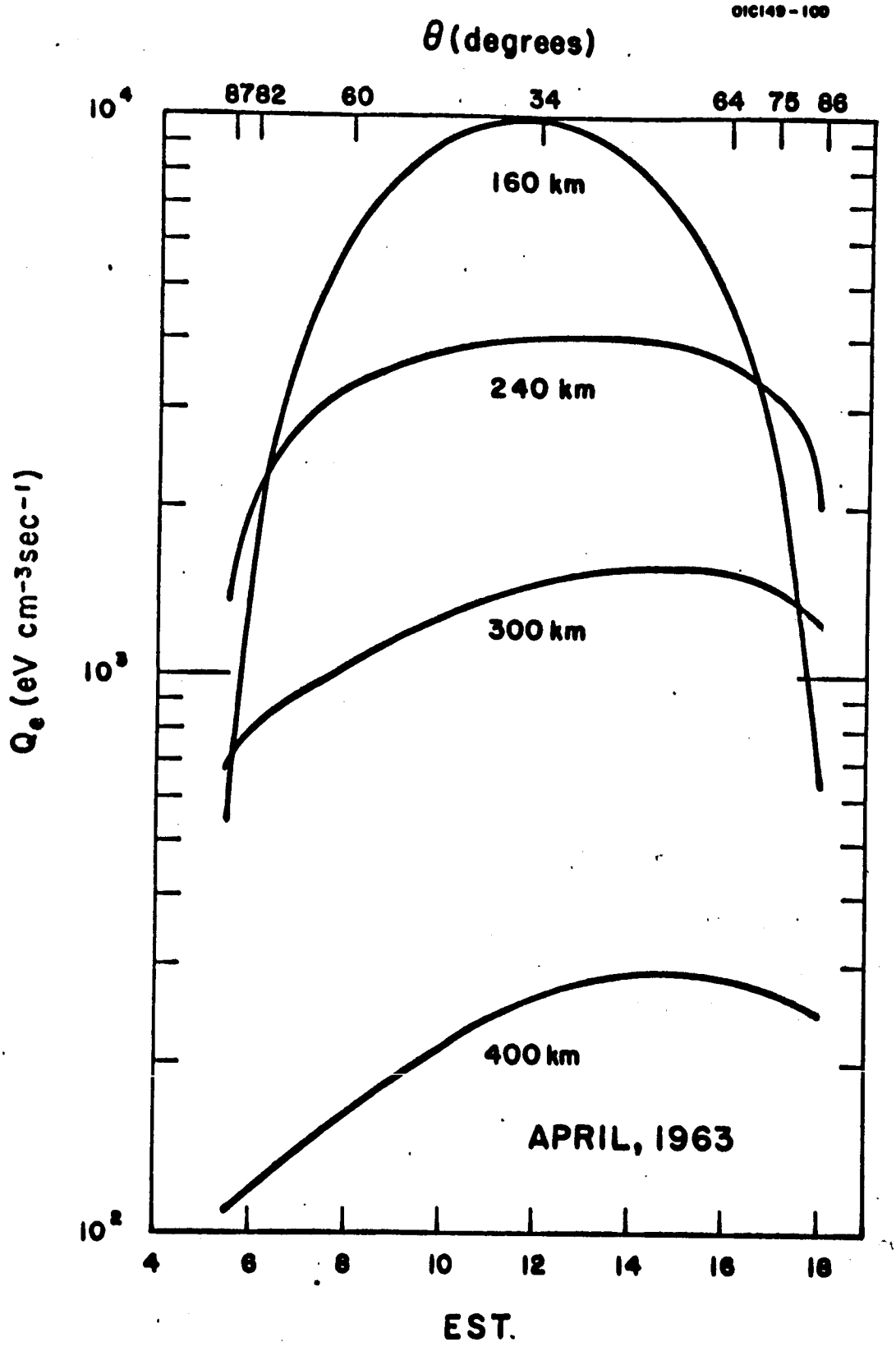

Figure 2. Electron heating rate Q_e at various altitudes as a function of Eastern Standard Time and solar zenith angle (θ).

In calculating the heat fluxes, we supposed that energy is deposited locally. Geisler and Bowhill[45] estimated the contribution from escaping photoelectrons, and their calculations show that it is negligible below 350 km. Above 350 km, conduction is important, and non-local heating does not significantly alter the temperature profile.[45]

e. Electron cooling

The hot electrons cool through elastic collisions with the positive ions and through elastic and inelastic collisions with the neutral particles. The rate at which the electron gas loses heat to a positive ion mixture of O^+, He^+, and H^+ is given approximately by

$$L_e = \frac{5 \times 10^{-7} (T_e - T_i)}{T_e^{3/2}} n_e \left\{ n(O^+) + 4n(He^+) + 16n(H^+) \right\} \text{ eV cm}^{-3} \text{ sec}^{-1} \quad (1)$$

where T_i is the positive ion temperature. In practice, the different positive ions have different temperatures at high altitudes, but the effect on the electron temperature is negligible.

The important cooling processes at low altitudes are elastic collisions, rotational and vibrational excitation of N_2 and O_2, and excitation of atomic oxygen to the ^1D level. For elastic collisions, we adopted the formulae given by Dalgarno et al.[43] adding a contribution from elastic collisions with helium for which we used the formula

$$L(He) = 2.3 \times 10^{-17} n_e \, n(He) \, T_e^{\frac{1}{2}} (T_e - T_n) \text{ eV cm}^{-3} \text{ sec}^{-1} \quad (2)$$

where T_n is the neutral particle gas temperature.

For rotational excitation of N_2, we adopted the formula of Dalgarno and Henry,[64] which allows for the dependence of cross section on electron temperature. The contribution to cooling by rotational excitation of O_2 is uncertain.[64-67] To describe it, we used without modification a formula quoted by Hanson.[42] This formula is consistent with earlier laboratory data of Phelps (cf. Hanson, Ref. 42) and introduces little uncertainty in the calculated electron temperature.

Dalgarno et al.[43] noted the possible importance of vibrational excitation as a cooling mechanism at high temperatures, and Dalgarno and Henry[64] used theoretical cross sections obtained by Chen[68] to compute the efficiency of cooling through excitation of the first vibrational level of N_2. They showed that it is more efficient than rotational cooling when T_e exceeds $1500^{\circ}K$. We supplemented the calculations of Dalgarno and Henry[64] by adding a contribution from excitation of the second vibrational level of N_2. We ignored vibrational excitation of O_2, the possible error in T_e being no larger than that introduced by uncertainty concerning the role of rotational excitation.

Dalgarno and McElroy[69] discussed the importance of the process

$$e + O(^3P) \rightarrow e + O(^1D)$$

as a cooling mechanism at high temperatures. They estimated its importance using cross sections presented by Seaton.[70] For this study, we adopted the more accurate data of Smith, Henry, and Burke[71] which give an efficiency about 20 percent larger than the earlier value.

The positive ion gas is heated by collisions with the hot electrons and cooled by collisions with the neutral particles. An expression for the energy loss of the positive ions has been given by Brace, Spencer, and Dalgarno,[34] and the ion temperature is readily obtained by equating this energy loss to the heat gain (1) from the electron gas. If, as we assume, only O^+ ions are present in significant quantity, the ion temperature is given by

$$T_i = T_n + \frac{5 \times 10^{-7} (T_e - T_n)}{T_e^{3/2}} n_e^2 \left\{ \frac{5 \times 10^{-7} n_e^2}{T_e^{3/2}} + n_e \left[9 \times 10^{-14} n(O) + 6 \times 10^{-14} n(N_2) + 6 \times 10^{-15} n(He) \right] \right\}^{-1} \quad (3)$$

f. Thermal conduction

Da Rosa[72] has shown that the electron temperature responds rapidly to diurnal changes. It is, therefore, adequately described by the time-independent heat equation

$$- \frac{d}{dz} \kappa \frac{dT_e}{dz} = Q_e(z) - L(z|T_e) \quad (4)$$

where κ is the coefficient of thermal conductivity. For a completely ionized plasma, κ is given by

$$\kappa_c = 7.7 \times 10^5 T_e^{5/2} \sin^2 I \quad (5)$$

where I is the geomagnetic dip angle (cf. Spitzer, Ref. 73). Geisler and Bowhill[45] and da Rosa[72] assumed that $\kappa = \kappa_c$. The thermal conductivity is, however, affected by the presence of the neutral particles, and we took κ as the harmonic mean

$$\kappa^{-1} = \kappa_c^{-1} + \kappa_n^{-1} \tag{6}$$

where κ_n is the conductivity due to collisions of the electrons with the neutral particles. For κ_n, we adopted the formula

$$\kappa_n = 3.2 \times 10^7 \frac{T_e\, n_e}{\upsilon_{en}} \sin^2 I \tag{7}$$

in which υ_{en} is the electron-neutral collision frequency,[74-77]

$$\upsilon_{en} = 1.7 \times 10^{-11}\, n(N_2)\, T_e + 3.8 \times 10^{-10}\, n(O_2)\, T_e^{\frac{1}{2}} + 1.4 \times 10^{-10}\, n(O)\, T_e^{\frac{1}{2}}. \tag{8}$$

Numerical solutions of the heat balance equation were obtained using a Runge-Kutta technique. We assumed a vanishing conductive flux at the top of the atmosphere and adopted as boundary conditions

$$L(120|T_e) = Q_e(120) \text{ and } \left.\frac{dT_e}{dz}\right]_\infty = 0. \tag{9}$$

g. Results and discussion

The important role of thermal conduction above 200 km in limiting the rise of T_e at high altitudes is illustrated in Figures 3 and 4 which compare the altitude profiles when thermal conduction is ignored and when it is included. In harmony with the conclusions of Geisler and Bowhill[45] and da Rosa,[72] we find that thermal conduction causes the electron gas to be essentially isothermal above 300 km if (as our calculations assume) there is no conductive flux into the ionosphere from above. Our results differ from those of Geisler and Bowhill[45] and of da Rosa[72] in that we do not find

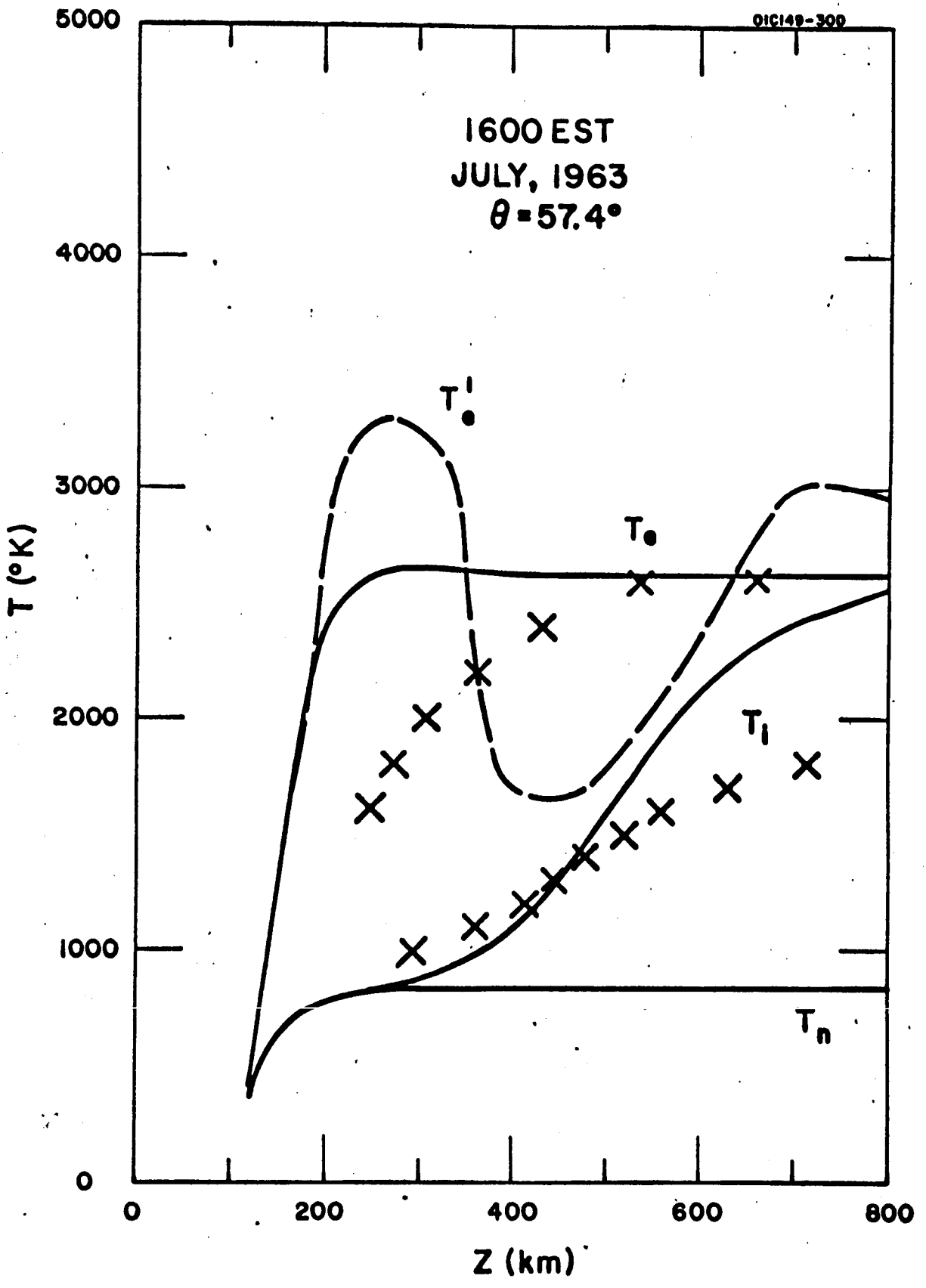

Figure 3. Profiles of electron, ion and neutral temperature (T_n) T_e' is the theoretical electron temperature with thermal conduction ignored. T_e is the temperature when conduction is considered and T_i is the ion temperature. The electron and ion temperatures measured by Evans[60] are indicated by X.

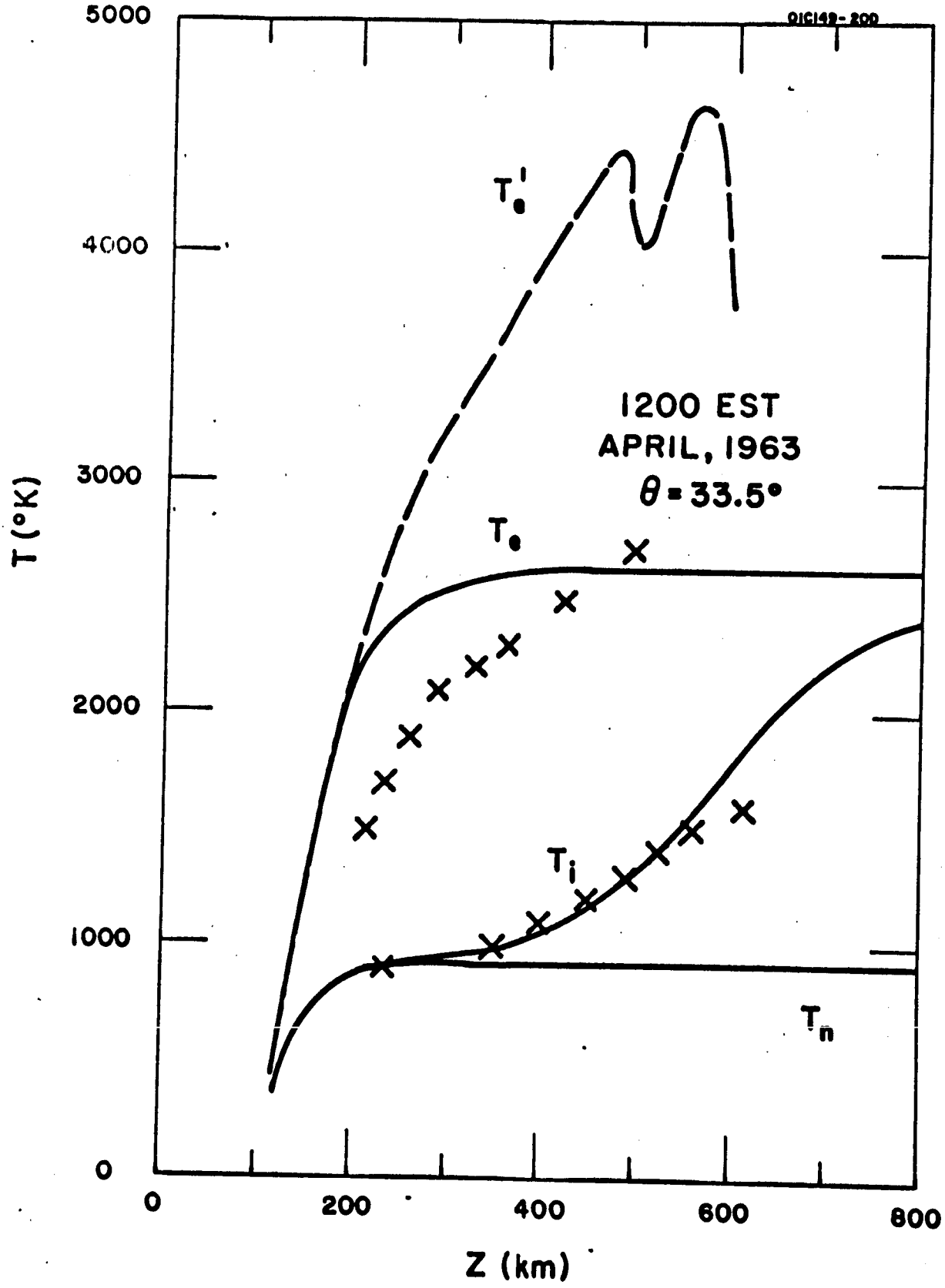

Figure 4. Profiles of electron, ion and neutral temperature (T_n). T_e' is the theoretical electron temperature with thermal conduction ignored. T_e is the temperature when conduction is considered and T_i is the ion temperature. The measured electron and ion temperatures[60] are indicated by X.

that the electron temperature is less than the gas temperature at any time. Their contrary conclusion is based upon calculations which ignore the effect on thermal conduction of collisions between the electrons and the neutral particles, and the difference probably stems from this omission.

At altitudes above about 700 km, our calculations underestimate the ion temperature since we ignored the role of hydrogen and helium ions which provide closer thermal contact between electrons and ions. This effect would increase the theoretical ion temperatures by less than $100^{o}K.$ (78)

We computed 21 altitude profiles for different times of the day during the months of April, July, and November 1963, two of which are compared with experimental profiles of Evans (60) in Figures 3 and 4. In all 21 cases, the ion temperatures agree within 25 percent with the experimental data. However, larger differences occur between the calculated and measured electron temperatures.

All of Evans' profiles show a positive electron temperature gradient at higher altitudes where the theoretical profiles are isothermal. The disagreement may not be significant since the backscatter temperature determinations are sensitive to assumptions about ion compositions and may be in error at higher altitudes where He^{+} is relatively more abundant. (79) A positive electron temperature gradient would imply a high altitude source such as conduction from the protonosphere.

The theoretical and experimental electron temperatures differ also at low altitudes. Thus, the experimental electron temperatures are less than the theoretical values and decrease rapidly with decreasing altitude between 300 and 200 km where the theoretical temperatures vary slowly. It is not possible to reconcile the backscatter temperatures measured at low altitudes with ultraviolet heating of the electron gas. The ultraviolet heat source peaks at around 200 km — well below the altitude at which the backscatter electron temperatures drop towards the neutral gas temperature.

Evidence supporting the theoretical profile is provided by measurements of electron temperatures and densities during a rocket flight in the mid-afternoon of April 18, 1963.[35] We calculated the electron temperature profile consistent with N_2 densities measured on the rocket flight. Our results are compared with the measured temperature profiles in Figure 5. The agreement is close at altitudes between 140 km and the peak of the rocket trajectory at 330 km. This comparison suggests that the rocket data and the backscatter data are not mutually consistent, the discrepancy failing to emerge fully from a direct comparison of the two sets of data[80] because the common altitude region was small. The rocket flight occurred during a period of high magnetic activity corresponding to an A_p index of 30. The close agreement between theory and observation suggests that no additional selective heating source was present for the electron gas.* The theory reproduces well the shape of

*A discrepancy between theory and measurement <u>below</u> 140 km has been found on most rocket flights.[35,81] In order to resolve it, it may be necessary to postulate a heat source at low altitudes in addition to that provided by solar ultraviolet radiation.

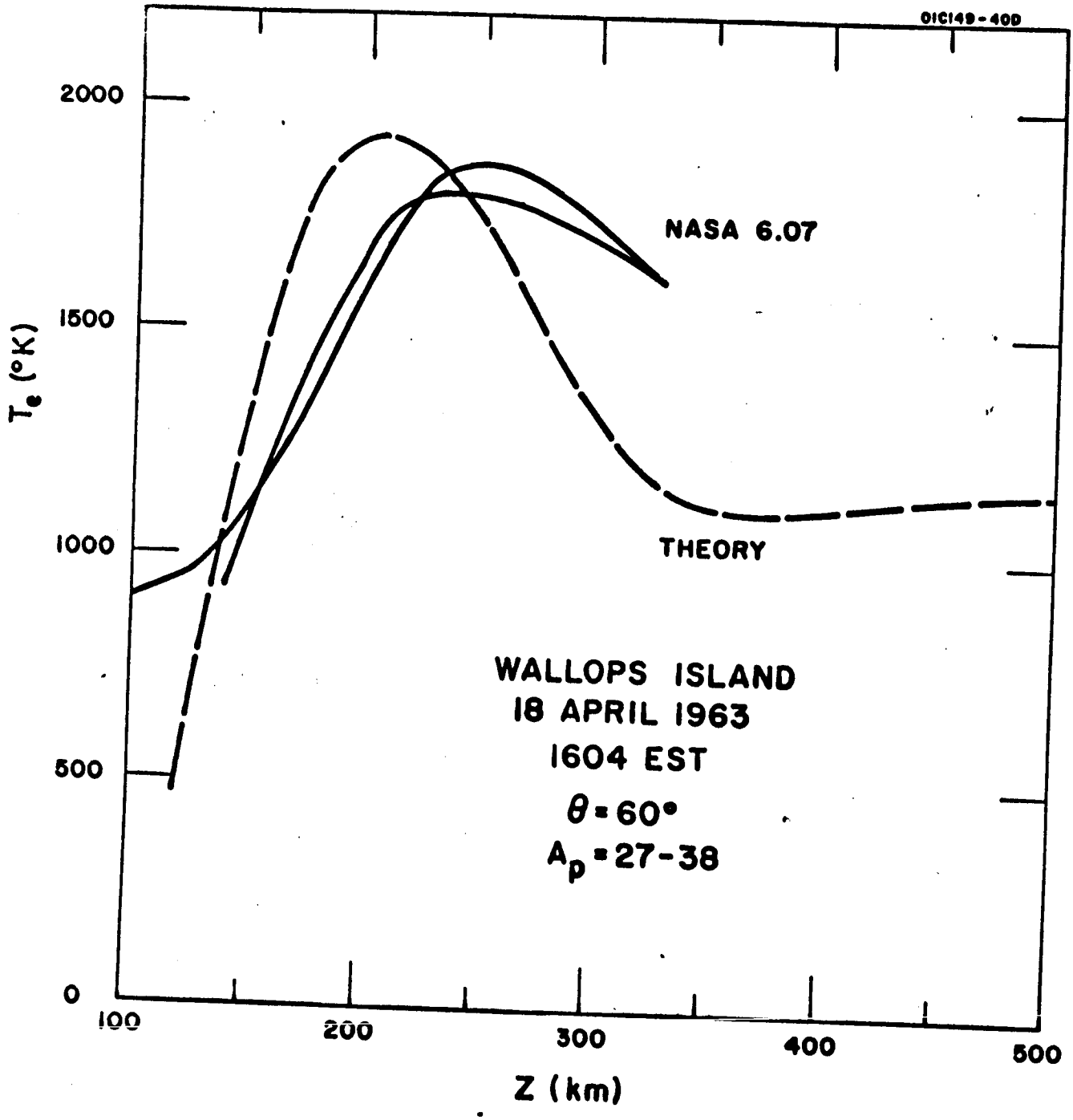

Figure 5. Comparison of theoretical electron temperature profile with the rocket measurement of Spencer, Brace, Carigan, Taeusch and Niemann.(35)

electron temperature profiles measured on earlier rocket flights reported by Brace, Spencer, and Carignan[31] and by Spencer et al.[35] It underestimates the magnitudes of the temperatures, as is to be expected since the calculations use ultraviolet flux values measured in July 1963, and the earlier rocket flights occurred at times of greater solar activity.

The theoretical profiles of T_e usually intersect the backscatter profiles obtained by Evans[60] at an altitude in the region of 400 km (cf. Figures 3 and 4). Figure 6 compares the theoretical and observed diurnal variations at 400 km in April, July, and November 1963. The observations show marked differences from month to month which are closely reproduced by the theory. The uncertainties in the adopted photoionization cross sections may introduce errors of up to 20 percent in the magnitudes of T_e, but they do not modify significantly the shape of the diurnal variation at any given altitude. Thus, the close agreement is unlikely to be fortuitous, and a reanalysis of the backscatter data would seem desirable. It may be possible to resolve the discrepancies which exist at other altitudes by allowing for the presence of minor ions.

The ratio of T_e/T_i is given by the analyses of backscatter data, and we show a typical theoretical profile in Figure 7. In harmony with profiles derived from backscatter data[38,60] and from a theoretical analysis of satellite data,[34] T_e/T_i passes through a maximum value of about 2 at an altitude near 350 km.

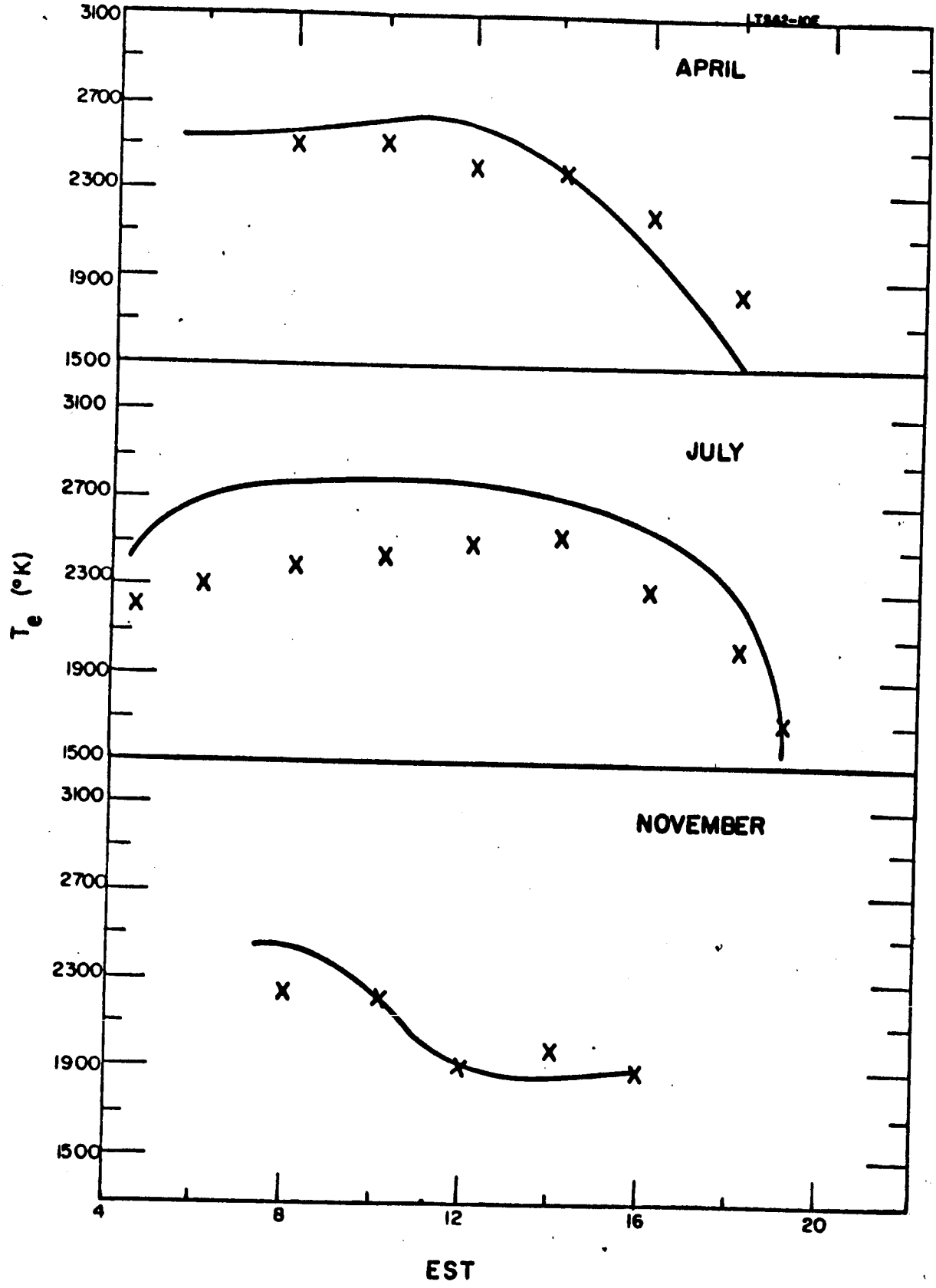

Figure 6. Theoretical and observed diurnal variations of electron temperature at 400 km. The measurements(60) are indicated by X.

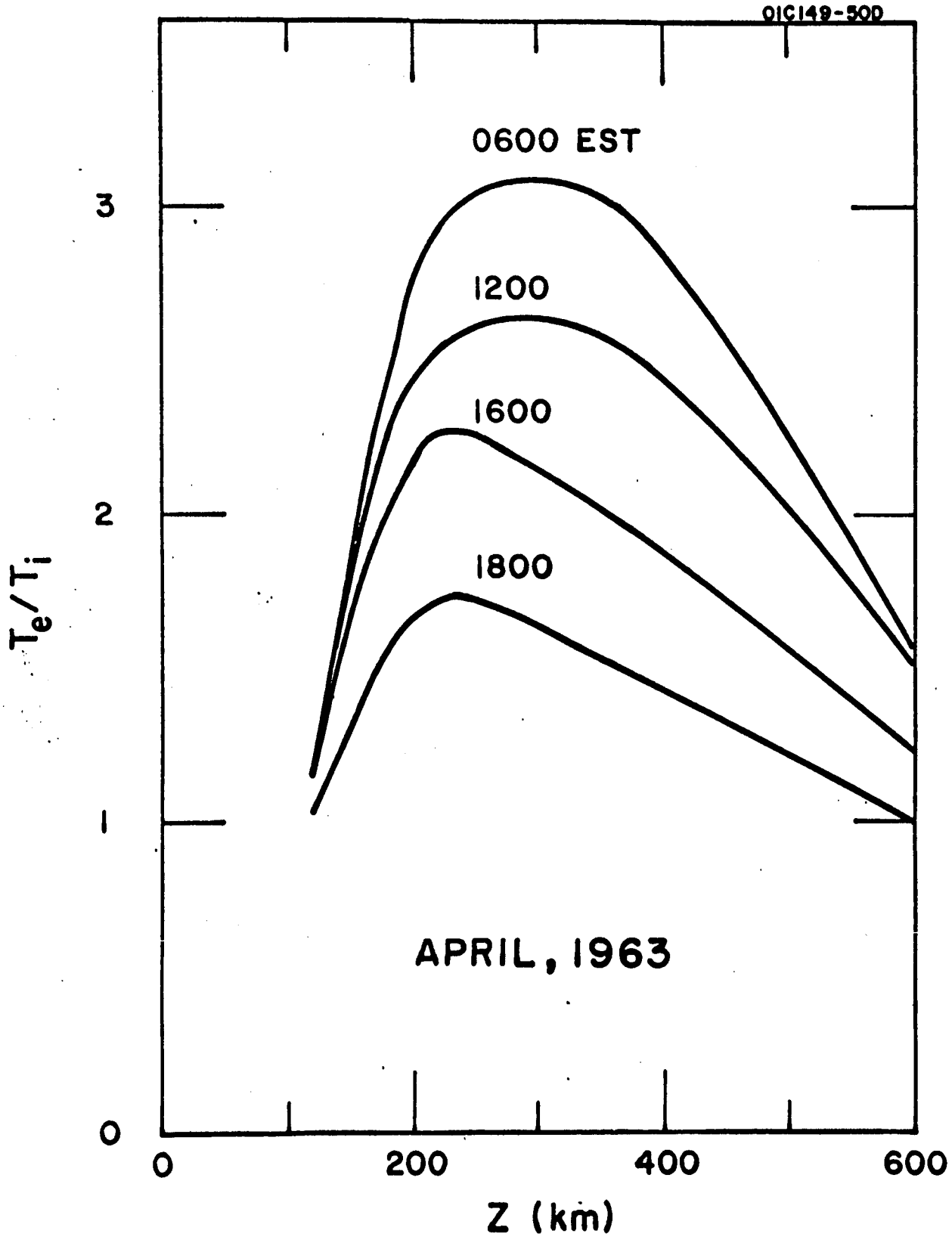

Figure 7. Profiles of the theoretical electron-ion temperature ration.

We present in Figures 8, 9, and 10 the theoretical average diurnal variations of T_e at various altitudes for the months of April, July, and November 1963. It appears that T_e rose rapidly at dawn to a broad maximum substantially in excess of the neutral particle temperature at altitudes above 150 km and then fell rapidly at dusk. Contained within the broad maximum were local variations of T_e which reflected local variations in electron density. Thus, the unusually low temperatures at high altitudes at noon in November correspond to an F-region peak electron density of 6.5×10^5 cm^{-3} whereas the corresponding density in April was 4×10^5 cm^{-3} and in July, 3×10^5 cm^{-3}. The inverse relationship of electron temperature and density has been verified experimentally by Brace, Spencer, and Dalgarno.[34]

A detailed tabulation of the computed electron and ion temperatures is presented in the appendix.

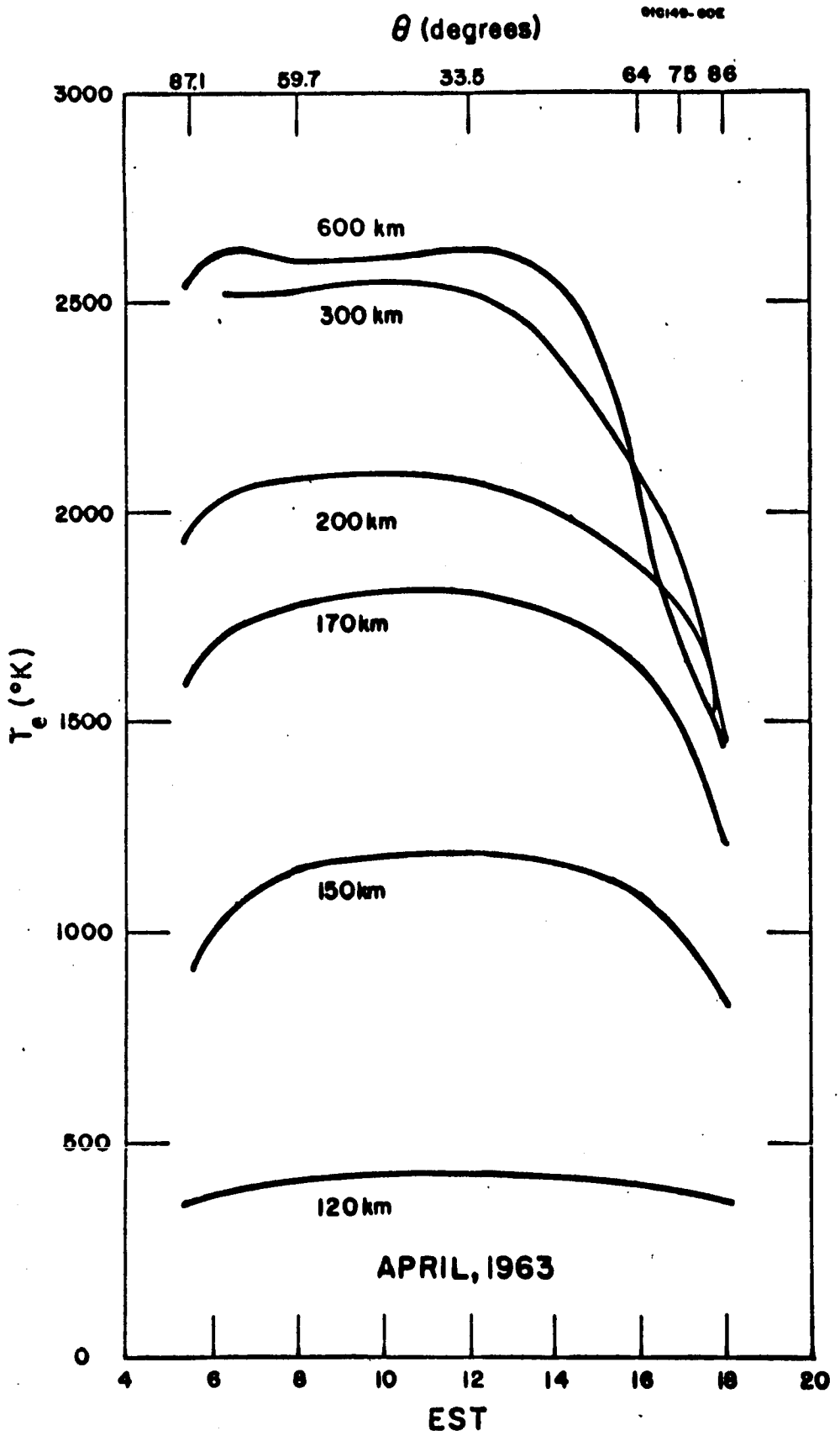

Figure 8. Theoretical electron temperatures at various altitudes as a function of Eastern Standard Time and solar zenith angle (θ).

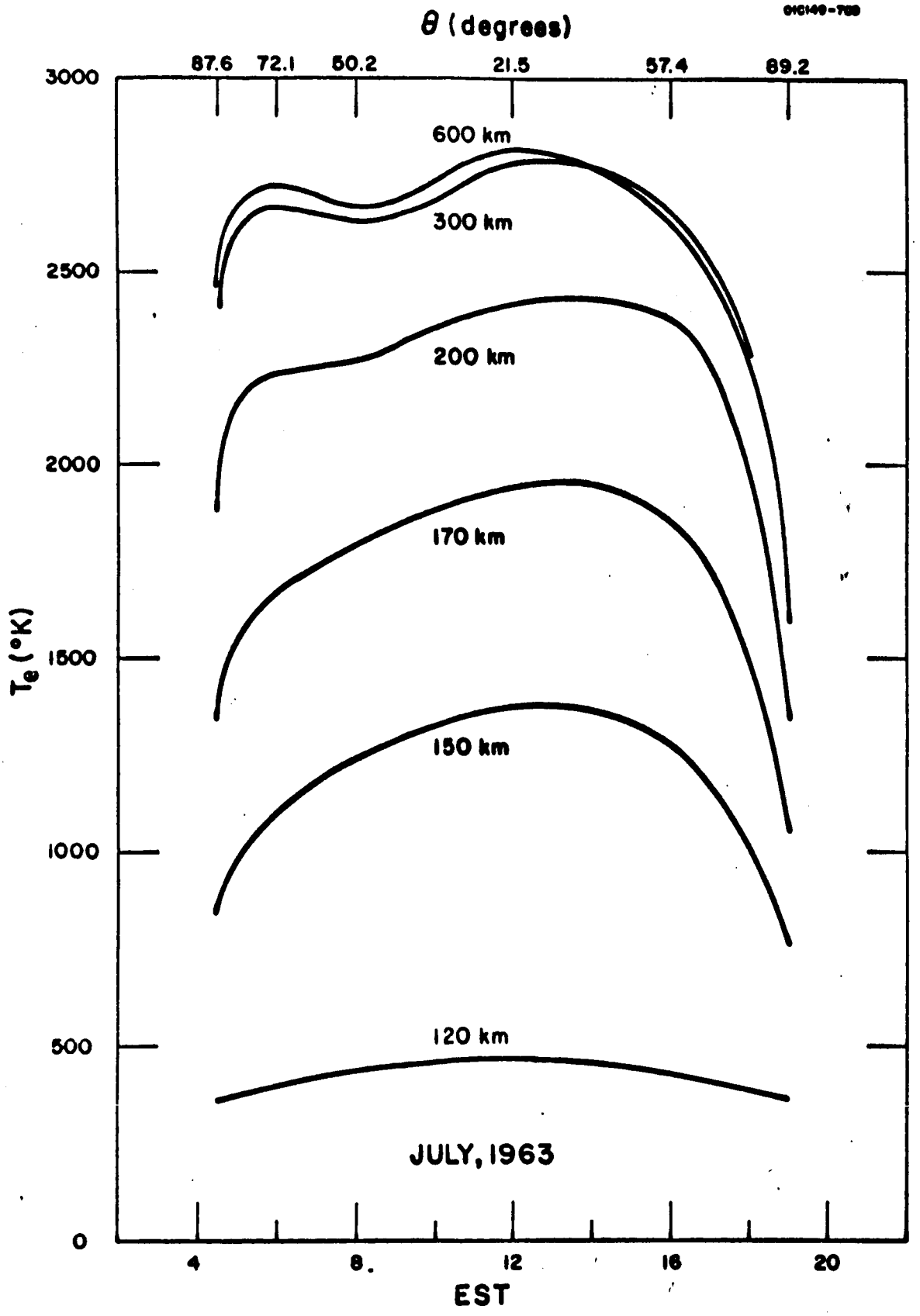

Figure 9. Electron temperatures at various altitudes as a function of Eastern Standard Time and solar zenith angle (θ).

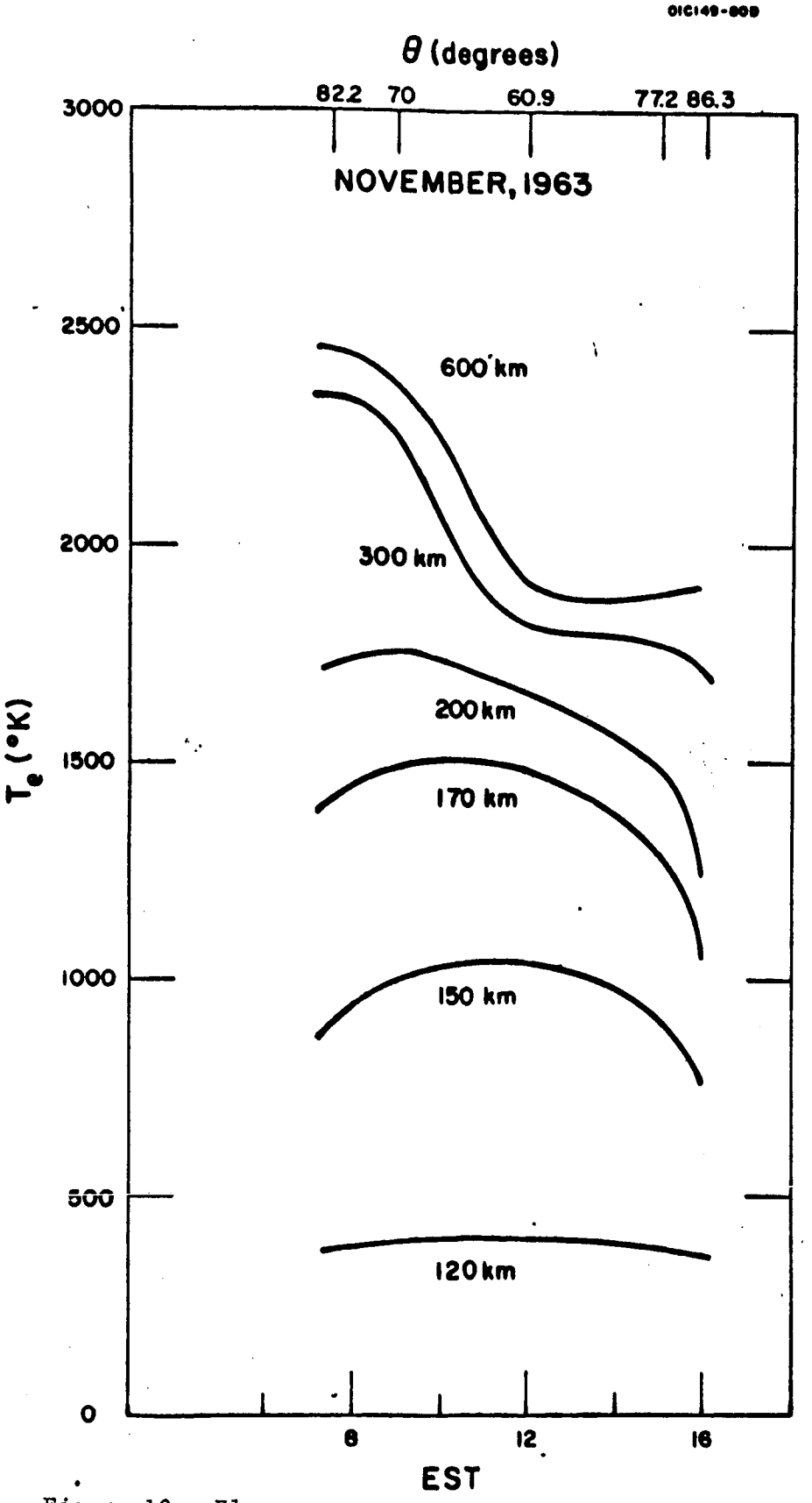

Figure 10. Electron temperatures at various altitudes as a function at Eastern Standard Time and solar zenith angle (θ).

Appendix

Electron densities, electron heating rates, electron temperatures and ion temperatures as a function of Eastern Standard Time (EST).

Table A1

April, 1963

Z	Ne	$Q_e$ev	T_e	T_i	N_e	$Q_e$ev	T_e	T_i
km	cm^{-3}	$cm^{-3}sec^{-1}$	^oK	^oK	cm^{-3}	$cm^{-3}sec^{-1}$	^oK	^oK
	0530 EST		$T_\infty^* = 788^o$		0800 EST		$T_\infty = 820^o$	
120	1.2(4)	7.27(1)	365	355	9.4(4)	3.56(3)	415	355
140	2.2(4)	3.15(2)	720	540	1.1(5)	5.17(3)	940	560
160	3.2(4)	5.43(2)	1220	640	1.6(5)	6.25(3)	1440	670
180	4.4(4)	8.31(2)	1800	700	2.1(5)	6.45(3)	1830	740
200	6.2(4)	1.07(3)	1980	740	2.7(5)	5.55(3)	2100	780
220	8.5(4)	1.27(3)	2160	760	3.3(5)	4.41(3)	2270	800
240	1.3(5)	1.36(3)	2280	770	3.4(5)	3.22(3)	2370	820
260	1.4(5)	1.23(3)	2360	780	3.2(5)	2.26(3)	2450	830
300	9.7(4)	6.77(2)	2460	800	2.3(5)	1.04(3)	2530	860
400	3.9(4)	1.07(2)	2530	860	1.1(5)	1.60(2)	2590	980
500	1.9(4)	1.72(1)	2540	1070	5.8(4)	2.73(1)	2600	1330
600	1.0(4)	3.34(0)	2540	1510	2.8(4)	5.19(0)	2600	1820
	1200 EST		$T_\infty = 917^o$		1600 EST		$T_\infty = 921^o$	
120	1.6(5)	8.21(3)	436	355	8.4(4)	2.85(3)	409	355
140	2.0(5)	9.43(3)	980	600	1.1(5)	4.03(3)	910	600
160	2.3(5)	1.00(4)	1470	740	1.5(5)	4.69(3)	1350	740
180	2.6(5)	8.97(3)	1860	820	1.9(5)	5.14(3)	1690	820
200	3.2(5)	7.18(3)	2110	860	2.5(5)	4.98(3)	1900	860
220	3.6(5)	5.46(3)	2270	890	3.2(5)	4.37(3)	2020	890
240	3.9(5)	4.05(3)	2380	910	4.1(5)	3.68(3)	2080	910
260	3.9(5)	2.94(3)	2450	930	4.8(5)	2.89(3)	2090	930
300	3.2(5)	1.46(3)	2530	950	4.7(5)	1.55(3)	2090	970
400	1.6(5)	2.63(2)	2610	1050	2.5(5)	2.86(2)	2070	1100
500	8.6(4)	5.27(1)	2620	1300	1.4(5)	5.76(1)	2070	1370
600	5.1(4)	1.15(1)	2620	1750	7.4(4)	1.23(1)	2070	1670

*T_∞ is the neutral temperature in the exosphere

Table A1 (Continued)

April, 1963

Z	Ne	$Q_e$ev	T_e	T_i	N_e	$Q_e$ev	T_e	T_i
km	cm^{-3}	$cm^{-3}sec^{-1}$	^oK	^oK	cm^{-3}	$cm^{-3}sec^{-1}$	^oK	^oK
	1700 EST		$T^*_\infty = 907^o$		1800 EST		$T_\infty = 890^o$	
120	4.9(4)	1.20(3)	394	355	2.0(4)	1.40(2)	366	355
140	8.2(4)	2.01(3)	820	600	4.3(4)	4.25(2)	700	590
160	1.1(5)	2.55(3)	1220	730	5.5(4)	6.41(2)	1040	720
180	1.5(5)	3.02(3)	1530	810	8.4(4)	9.29(2)	1250	790
200	2.2(5)	3.40(3)	1720	850	1.4(5)	1.18(3)	1400	830
220	3.1(5)	3.43(3)	1830	880	2.5(5)	1.57(3)	1490	860
240	4.3(5)	3.20(3)	1870	900	4.0(5)	1.95(3)	1530	880
260	4.8(5)	2.60(3)	1880	920	4.8(5)	1.90(3)	1550	900
300	4.8(5)	1.45(3)	1860	960	4.9(5)	1.25(3)	1540	940
400	2.5(5)	2.69(2)	1780	1080	2.5(5)	2.48(2)	1510	1050
500	1.3(5)	5.27(1)	1720	1290	1.3(5)	4.77(1)	1470	1220
600	7.0(4)	1.28(1)	1670	1640	7.0(5)	1.13(1)	1430	1420

*T_∞ is the neutral temperature in the exosphere

Table A2

July 1963

Z	Ne	$Q_e$ev	T_e	T_i	N_e	$Q_e$ev	T_e	T_i
km	cm^{-3}	$cm^{-3}sec^{-1}$	^oK	^oK	cm^{-3}	$cm^{-3}sec^{-1}$	^oK	^oK
	0430 EST		$T_\infty = 716^o$		0600 EST		$T_\infty = 734^o$	
120	2.4(4)	6.85(1)	359	355	7.0(4)	1.69(3)	393	355
140	4.0(4)	3.26(2)	650	512	9.0(4)	2.97(3)	863	520
160	5.4(4)	5.48(2)	1100	601	1.2(5)	3.88(3)	1400	613
180	6.8(4)	8.63(2)	1560	651	1.6(5)	4.48(3)	1900	667
200	8.3(4)	1.11(3)	1890	680	1.8(5)	4.04(3)	2230	698
220	9.4(4)	1.28(3)	2100	698	1.9(5)	3.10(3)	2420	718
240	9.5(4)	1.20(3)	2220	710	1.9(5)	2.27(3)	2530	732
260	9.0(4)	9.86(2)	2310	719	1.7(5)	1.56(3)	2600	744
280	8.5(4)	7.56(2)	2360	728	1.5(5)	1.04(3)	2640	755
300	7.7(4)	5.36(2)	2390	737	1.3(5)	6.95(2)	2670	768
340	5.7(4)	2.47(2)	2430	762	1.0(5)	3.08(2)	2700	805
400	2.9(4)	7.06(1)	2450	814	6.6(4)	9.15(1)	2710	917
	1200 EST		$T_\infty = 809^o$		1600 EST		$T_\infty = 829^o$	
120	1.3(5)	9.09(3)	466	355	9.1(4)	3.87(3)	423	355
140	1.7(5)	1.14(4)	1100	553	1.1(5)	5.54(3)	1010	562
160	1.9(5)	1.20(4)	1680	665	1.3(5)	6.43(3)	1580	678
180	2.1(5)	9.54(3)	2160	728	1.5(5)	6.42(3)	2090	744
200	2.4(5)	6.70(3)	2420	766	1.7(5)	5.24(3)	2380	782
220	2.6(5)	4.58(3)	2570	789	2.0(5)	3.95(3)	2530	806
240	2.7(5)	3.19(3)	2660	806	2.5(5)	3.04(3)	2600	824
260	2.8(5)	2.23(3)	2720	821	2.9(5)	2.26(3)	2630	840
280	2.6(5)	1.52(3)	2750	836	3.1(5)	1.62(3)	2650	859
300	2.4(5)	1.03(3)	2770	852	3.1(5)	1.14(3)	2650	881
340	2.0(5)	4.84(2)	2790	901	2.7(5)	5.47(2)	2650	940
400	1.2(5)	1.54(2)	2800	1000	2.0(5)	1.85(2)	2640	1090

Table A2 (Continued)

July 1963

Z	Ne	$Q_e$ev	T_e	T_i	Ne	$Q_e$ev	T_e	T_i
km	cm^{-3}	$cm^{-3}sec^{-1}$	^oK	^oK	cm^{-3}	$cm^{-3}sec^{-1}$	^oK	^oK
	1800 EST		$T_\infty = 811^o$		1900 EST		$T_\infty = 792^o$	
120	4.9(4)	8.06(2)	381	355	2.7(4)	2.50(1)	356	355
140	6.2(4)	1.40(3)	796	554	3.4(4)	1.97(2)	623	545
160	8.4(4)	1.97(3)	1260	666	4.4(4)	3.01(2)	912	652
180	1.1(5)	2.43(3)	1680	729	6.8(4)	5.33(2)	1170	713
200	1.4(5)	2.72(3)	1960	766	1.2(5)	7.43(2)	1350	748
220	2.0(5)	2.69(3)	2120	789	2.0(5)	1.04(3)	1470	771
240	2.5(5)	2.40(3)	2210	807	2.8(5)	1.35(3)	1540	789
260	3.0(5)	1.94(3)	2250	825	3.4(5)	1.36(3)	1580	808
280	3.2(5)	1.45(3)	2280	844	3.7(5)	1.15(3)	1590	830
300	3.2(5)	1.04(3)	2280	869	3.8(5)	8.88(2)	1590	858
340	2.8(5)	5.05(2)	2280	934	3.1(5)	4.53(2)	1580	919
400	1.8(5)	1.65(2)	2280	1070	1.8(5)	1.48(2)	1590	1030

Table A3

November 1963

Z	Ne	$Q_e$ev	T_e	T_i	N_e	$Q_e$ev	T_e	T_i
km	cm^{-3}	$cm^{-3}sec^{-1}$	^oK	^oK	cm^{-3}	$cm^{-3}sec^{-1}$	^oK	^oK
	0730 EST		T = 793°		0800 EST		T = 804°	
120	3.5(4)	4.51(2)	375	355	5.6(4)	9.82(2)	383	355
140	5.4(4)	9.15(2)	730	550	7.8(4)	1.69(3)	760	550
160	8.6(4)	1.44(3)	1120	650	1.2(5)	2.36(3)	1150	660
180	1.5(5)	1.90(3)	1460	710	2.1(5)	2.99(3)	1490	720
200	2.5(5)	2.41(3)	1750	750	3.0(5)	3.43(3)	1770	760
220	2.8(5)	2.53(3)	1970	770	3.4(5)	3.30(3)	1980	780
240	2.6(5)	2.19(3)	2130	790	3.3(5)	2.64(3)	2130	800
260	2.1(5)	1.64(3)	2210	800	2.9(5)	1.94(3)	2230	810
300	1.3(5)	7.99(3)	2350	820	1.8(5)	9.09(2)	2340	840
400	5.6(4)	1.23(2)	2430	900	7.7(4)	1.38(2)	2420	930
500	3.0(4)	2.06(1)	2450	1160	4.2(4)	2.33(1)	2440	1240
600	1.7(4)	3.98	2450	1660	2.3(4)	4.47	2440	1740
	0900 EST		T_∞ = 827°		1200 EST		T_∞ = 887°	
120	7.7(4)	2.01(3)	396	355	1.1(5)	3.51(3)	405	355
140	1.1(5)	3.22(3)	820	560	1.5(5)	4.91(3)	870	590
160	1.6(5)	4.03(3)	1220	680	2.0(5)	5.71(3)	1260	720
180	2.5(5)	4.73(3)	1540	740	2.9(5)	6.22(3)	1520	790
200	3.8(5)	4.86(3)	1770	780	4.1(5)	5.91(3)	1670	830
220	4.3(5)	4.23(3)	1950	810	5.3(5)	5.13(3)	1740	860
240	4.2(5)	3.21(3)	2080	830	6.4(5)	4.08(3)	1770	890
260	3.7(5)	2.28(3)	2170	840	6.4(5)	2.97(3)	1780	910
300	2.7(5)	1.08(3)	2270	870	4.8(5)	1.44(3)	1820	940
400	1.1(5)	1.65(2)	2350	980	1.9(5)	2.38(2)	1890	1050
500	5.8(4)	2.87(1)	2370	1300	1.0(5)	4.53(1)	1910	1290
600	3.4(4)	5.61	2370	1790	5.8(4)	9.40	1920	1600

Table A3 (Continued)

November 1963

Z	Ne	$Q_e$ev	T_e	T_i	Ne	$Q_e$ev	T_e	T_i
km	cm^{-3}	$cm^{-3}sec^{-1}$	^oK	^oK	cm^{-3}	$cm^{-3}sec^{-1}$	^oK	^oK
	1500 EST		$T_\infty = 893^o$		1600 EST		$T_\infty = 884^o$	
120	7.0(4)	1.13(3)	381	355	4.5(4)	1.70(2)	361	355
140	9.2(4)	1.69(3)	760	590	6.0(4)	4.25(2)	670	590
160	1.4(5)	2.27(3)	1090	720	9.1(4)	6.43(2)	900	720
180	2.1(5)	2.75(3)	1330	800	1.8(5)	9.50(2)	1090	790
200	3.2(5)	3.27(3)	1490	840	2.9(5)	1.28(3)	1240	830
220	4.5(5)	3.55(3)	1600	870	3.9(5)	1.76(3)	1380	860
240	5.7(5)	3.26(3)	1660	890	4.9(5)	2.01(3)	1500	880
260	6.0(5)	2.61(3)	1700	910	5.2(5)	1.89(3)	1590	900
300	4.6(5)	1.38(3)	1770	940	3.8(5)	1.16(3)	1730	930
400	1.9(5)	2.42(2)	1860	1050	1.5(5)	2.21(2)	1870	1020
500	1.0(5)	4.69(1)	1880	1280	8.0(4)	4.28(1)	1900	1240
600	5.8(4)	9.82	1880	1570	5.0(4)	9.02	1910	1570

C. EXPERIMENTAL INVESTIGATIONS IN THE VUV (2000-1000Å) AND THE EUV (BELOW 1000Å) SPECTRAL REGIONS

A detailed specification of the experimental investigations to be performed in the VUV (2000-1000Å) and EUV (below 1000Å) under the current program are contained in the Statement of Work. The five planned laboratory investigations are: (1) measure absorption and photoionization cross sections for atomic atmospheric species in the VUV and EUV, (2) measure the kinetic energy and spatial distribution of ejected photoelectrons due to VUV and EUV photoionization, (3) design, develop, and construct new experimental devices such as windows, filters, counters, etc., if and when necessary for proper performance of the VUV and EUV investigations, (4) measure the spectral variation of the ionization potential and photoionization efficiency of a number of planetary gases in the EUV, and (5) measure ionic mobility of selected planetary gases for wavelengths in the EUV.

It can be seen from the above that Items (4) and (5) involve laboratory investigations which are performed solely in the EUV region. To gain access to this spectral region, it is necessary to first design, develop, construct, fabricate, and test a suitable grazing incidence monochromator. At present, only initial design criteria have been established so that no EUV laboratory investigations are being conducted. Accordingly, during the current reporting period, experimental studies in the VUV region under Items (1), (2), and (3) have been performed as discussed below.

1. Absorption and Photoionization Cross Sections of Atomic H, O, and N in the VUV

The measurement of photoionization cross sections of atomic hydrogen has been discussed in the previous Quarterly Progress Report.[1]

During the current reporting period, additional experiments have been performed on discharged nitrogen in an effort to measure the photoionization cross sections of atomic nitrogen. However, due to the presence of several metastable species in discharged nitrogen, it has not been possible to successfully extract the atomic cross section from the observed data. It is interesting to note that Henry[82] has recently published a further theoretical estimate of this cross section, which is in relatively good agreement (for $\lambda\lambda < 500\text{Å}$) with one-half the σ-values of N_2 as measured by this laboratory.[83] Henry[82] notes that a useful guide to the L_1-absorption cross section is obtained by assuming that $\sigma(N) = \frac{1}{2}\sigma(N_2)$ where the experimental values for $\frac{1}{2}\sigma(N_2)$ of Samson and Cairns[83] are represented by crosses in Figure 11. As can be seen in this figure, he concludes that the dipole-length (σ_{DL}) formalism is in better agreement with the experimental values than the dipole-velocity (σ_{DV}) formalism for intermediate energies. This conclusion is in essential agreement with the approach adopted in this laboratory as discussed in the previous Quarterly Progress Report.[1] Additionally, a recent laboratory experiment by Carroll et al.[84] has yielded new data on the continuous absorption of atomic nitrogen and has resulted in the identification of a new Rydberg series for the spectral region $\lambda\lambda$ 694 to 612Å.

For the case of atomic oxygen, a new Rydberg series has been identified[85] which can now be compared with the GCA cross-section data[86] to derive new information for this parameter.

Additionally, experimental studies of autoionization in atomic species have recently been pursued on an accelerated basis by

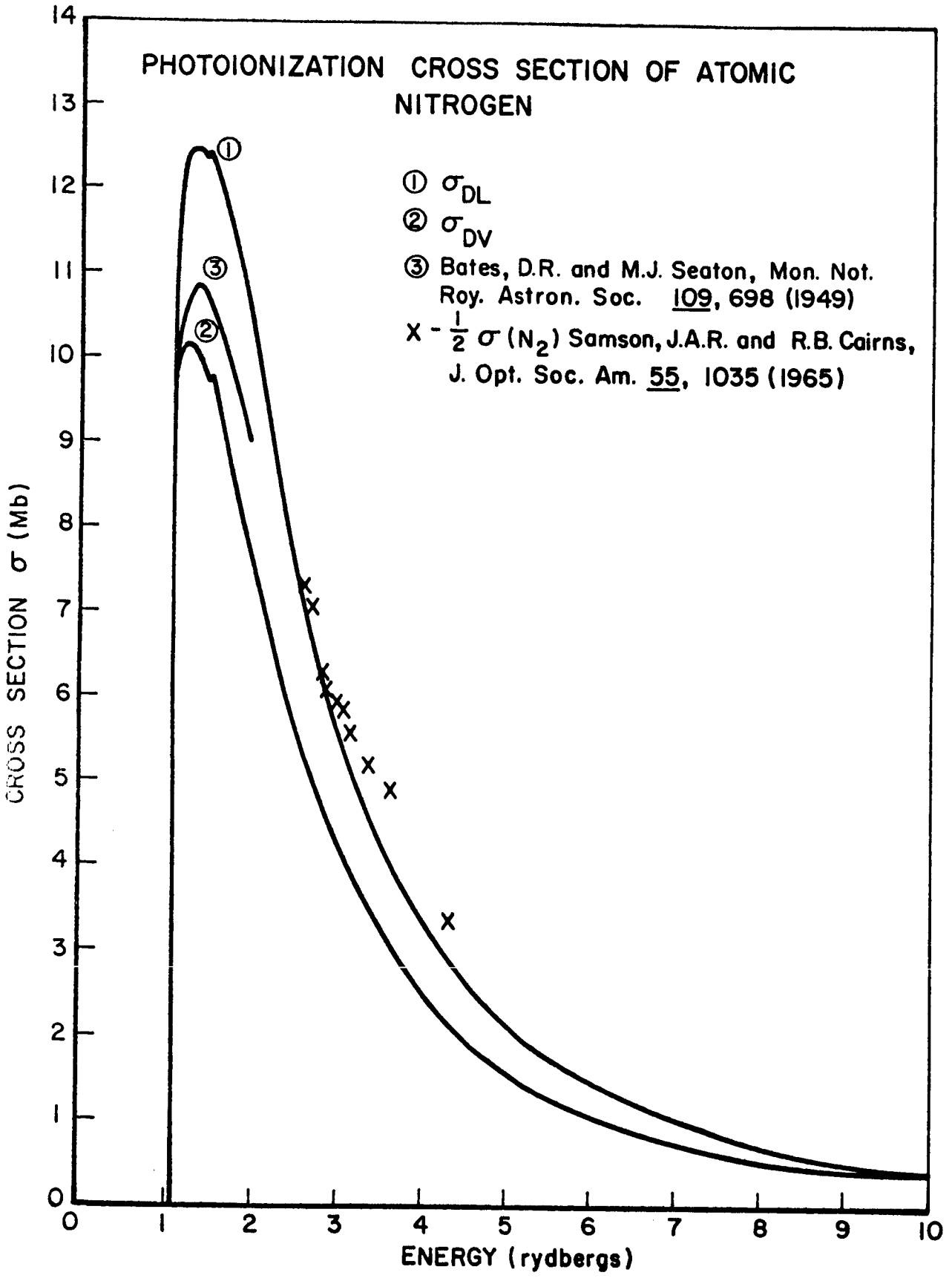
PHOTOIONIZATION CROSS SECTION OF ATOMIC NITROGEN
① σ_{DL}
② σ_{DV}
③ Bates, D.R. and M.J. Seaton, Mon. Not. Roy. Astron. Soc. 109, 698 (1949)
X - $\frac{1}{2}\sigma(N_2)$ Samson, J.A.R. and R.B. Cairns, J. Opt. Soc. Am. 55, 1035 (1965)
CROSS SECTION σ (Mb)
ENERGY (rydbergs)
0
1
2
3
4
5
6
7
8
9
10
11
12
13
14

Figure 11

several laboratories including GCA. Specifically, an important program under the present contract involves the identification and the measurement of the pertinent cross sections associated with autoionization bands in both atomic oxygen and nitrogen.

It is planned to summarize the GCA results and those of other laboratories with respect to a careful tabulation of the wavelengths of expected autoionized lines in atomic oxygen and nitrogen and to publish this review as a GCA Technical Report.

2. The Kinetic Energy and Spatial Distribution of Ejected Photoelectrons Due to VUV Photoionization

A major effort under the present program involves the measurement of the kinetic energy and spatial distribution of ejected photoelectrons due to EUV photoionization. Although the grazing incidence monochromator required for this study has not been fabricated, it should be recognized that this EUV program represents a logical extension of the previous VUV studies which have been performed in this laboratory under past programs and during the current reporting period. A review article, which has been prepared to summarize these VUV results, has served to identify the EUV problems to further define the projected laboratory program. The article, entitled "Vacuum Ultraviolet Research" by J.A.R. Samson, has been submitted as an invited paper to the Journal of Applied Optics and, as such, will not appear in print for some time. For this reason, the article is reproduced below in its entirety.

a. Vacuum ultraviolet research

The vacuum ultraviolet region of the spectrum covers the wavelength range from about 2 to 2000Å. This is the region where air is strongly absorbing; thus, vacuum spectrographs and monochromators should be evacuated to a low pressure to avoid reducing the intensity of the incident radiation. Pressures in the range 10^{-5} to 10^{-6} torr are suitable for most applications. The absorption of monochromatic radiation is given by the Lambert-Beer Law

$$I = I_o \exp(-\sigma n L), \tag{10}$$

where I_o is the initial intensity of the radiation, and I is the intensity after traveling a distance L through a gas of density $\underline{n}$ molecules/cc. The constant σ is the absorption cross section of the gas and is a function of the wavelength. For air, σ is equal to 23 Mb at a wavelength of 584Å (1 megabarn = 10^{-18} cm^2). Thus, 63 percent of 584Å radiation will be absorbed in traveling a distance of 1 m through air at a pressure of 12μ.

The vacuum ultraviolet region was discovered by Viktor Schumann in the 1890's. Using the first vacuum spectrograph and specially prepared emulsions, Schumann photographed the H_2 spectrum down to 1267Å. This short wavelength limit was imposed by the transmittance of his fluorite prism. The invention of the concave grating by Rowland in 1882 and its application to vacuum ultraviolet radiation by Lyman in 1904 heralded the beginning of research in the vacuum ultraviolet. These early investigations were mostly concerned with the emission spectra of

the elements providing information about the energy levels of atoms. The discovery of the resonance series of atomic hydrogen by Lyman provided experimental verification of the Bohr theory of the atom. In addition to providing information on molecular structure, vacuum ultraviolet radiation is now being used as a research tool in plasma physics, solid state physics, photochemistry, upper atmosphere, solar, and stellar physics.

Many reviews have been written on vacuum ultraviolet spectroscopy, most of which contain discussions of the instrumentation necessary for work in this spectral region.[87-103] Thus, the present review will concentrate on the applications of vacuum ultraviolet radiation to various areas of research. No attempt will be made to cover all the uses of vacuum ultraviolet radiation, but rather the aim is to illustrate the usefulness of this radiation to fundamental research. The Proceedings of the First International Conference on Vacuum Ultraviolet Radiation Physics provides an excellent cross section of the type of research currently in progress.[104]

(1) Vacuum ultraviolet interactions with gases

The onset energies for many important interactions between radiation and gases occur at wavelengths less than 2000Å. Such interactions include excitation, dissociation, ionization, dissociative ionization, and multiple electron excitations. In the past, most information concerning the structure of atoms and molecules has been obtained from

studying emission and absorption spectra. This has been a successful and major area of study for a long time and continues to be so. However, in recent years, many methods have been devised for studying the individual absorption processes. The main avenues open for investigating these specific absorption processes are: (a) the identification of ionized fragments along with measurements of their appearance potentials and their kinetic energies, (b) the measurement of the kinetic energies of photoelectrons, and (c) the observation of fluorescent radiation. These items are discussed in more detail below.

(a) Photoionization - mass spectrometry. The feasibility of using vacuum ultraviolet radiation to produce a measurable ionization within the ion chamber of a mass spectrometer was first demonstrated by Lossing and Tanaka[105] and independently by Herzog and Marmo.[106] These early experiments used undispersed radiation. However, with improved techniques in the production and dispersion of vacuum ultraviolet radiation, it was possible to combine a monochromator with a mass spectrometer.[107,108] Figure 12 shows a typical experimental arrangement. With such a combination, both the parent ions and fragment ions produced by photoionization can be identified unambiguously. Several groups[109-117] are currently using a monochromator-mass spectrometer combination for studying ionization potentials, fragmentation onset potentials, fragmentation ratios, and ion-molecule reactions.[117] For studying ion-molecule reactions, the use of vacuum ultraviolet radiation is particularly advantageous since (a) the ion chamber remains at room temperature, (b) it is generally possible to ionize only one molecular species in a gas mixture, and (c) if the wavelength of the ionizing radiation

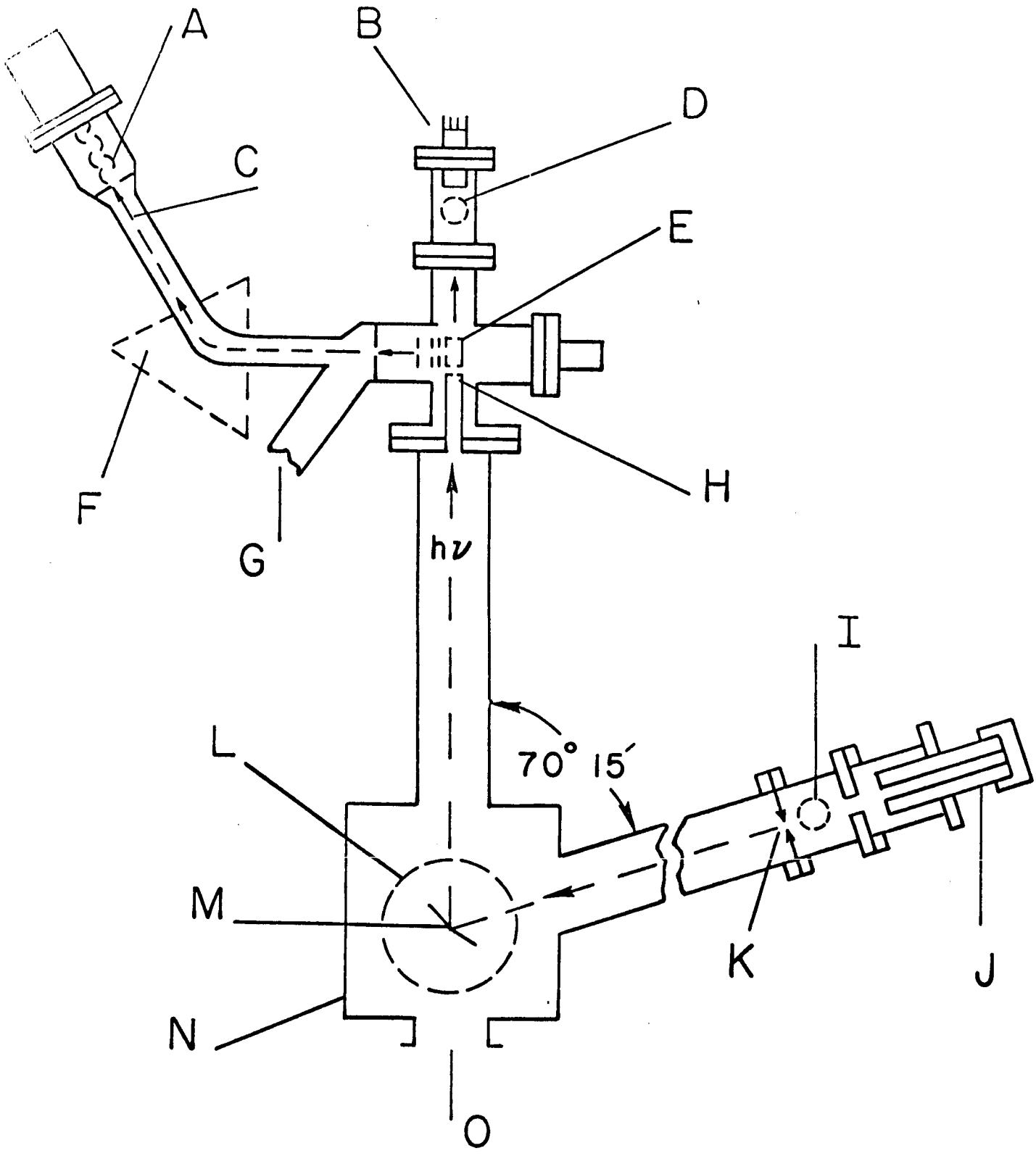

Figure 12. Vacuum monochromator and mass spectrometer. A, electron multiplier ion detector; B, photomultiplier radiation monitor; C, ion beam; D, G, I, O, to pumping systems; E, ion chamber; F, permanent magnet; H, monochromator exit slit; J, light source; K, monochromator entrance slit; L, grating turntable; M, grating; N, Seya type vacuum monochromator

is near the ionization threshold of the molecule, the molecular ion will be formed in its ground state. The same advantages hold true for measuring the mobilities of ions,[118] particularly if the mobility of an ion in a gas mixture is desired.

Very little work has been done on measuring the kinetic energies of the fragment ions produced in the photoionization process.[119]

(b) Photoelectron spectroscopy. Perhaps the most important technique for studying specific absorption processes is that of photoelectron spectroscopy. This technique entails the measurement of the kinetic energies of the ejected photoelectrons. The energy E of a photoelectron is given by $E = h\nu - I_j$, where $h\nu$ represents the photon energy and I_j represents the ionization potential of the j^{th} excited state of the ion. In argon, for instance, the removal of an outer p-electron can leave the ion in its $^2P_{3/2}$ ground state or in the $^2P_{1/2}$ excited state. The energy separation of these two states is 0.18 eV; thus, two groups of photoelectrons will be produced differing in energy by 0.18 eV. For molecules, many groups of electrons with specific energies may be formed depending on the initial photon energy.

Photoelectron spectroscopy was first described by Vilesov et al.[120] in 1961 and later independently by Turner and his associates.[121-125] Vilesov et al. operated at wavelengths longer than the LiF cutoff (1040Å) studying the electron energy spectrum as a function of wavelength from organic compounds. Turner has used undispersed radiation

from a helium discharge which at wavelengths shorter than 1200Å produces primarily the 584Å He I resonance line. Other groups[126-130] have started measuring electron energy spectra as a function of wavelength below 1000Å.

Electrostatic and magnetic focusing techniques have been used to analyze electron energy spectra. However, the simplest analyzer utilizes a retarding potential between two grids. Figure 13 shows the spherical analyzer used by Frost et al.[131] A variable retarding potential can be applied either between the spherical grids or between the outer grid and the spherical collector. Two hollow metal tubes at the same potential as the inner grid allow the radiation to enter the analyzer creating photoelectrons in a small volume element at the center of the concentric spheres. Thus, the photoelectrons will always travel in a direction normal to the retarding potential. To obtain more sensitivity, the solid spherical collector can be replaced by an electron multiplier.[130] Typical results obtained by Samson and Cairns[130] using dispersed 584Å radiation to ionize N_2 are shown in Figure 14. With zero retarding potential, the photoelectron current is a maximum. As the retarding potential increases, a reduction occurs in the photoelectron current at a potential just equal to the kinetic energy of the electrons comprising that particular group. Thus, a series of steps can be observed, the magnitude of which are a measure of the number of ions produced in the corresponding excited states. The vibrational structure of the $A\ ^2\Pi_u$ state is clearly visible. Data of this nature are very important to atmospheric studies.

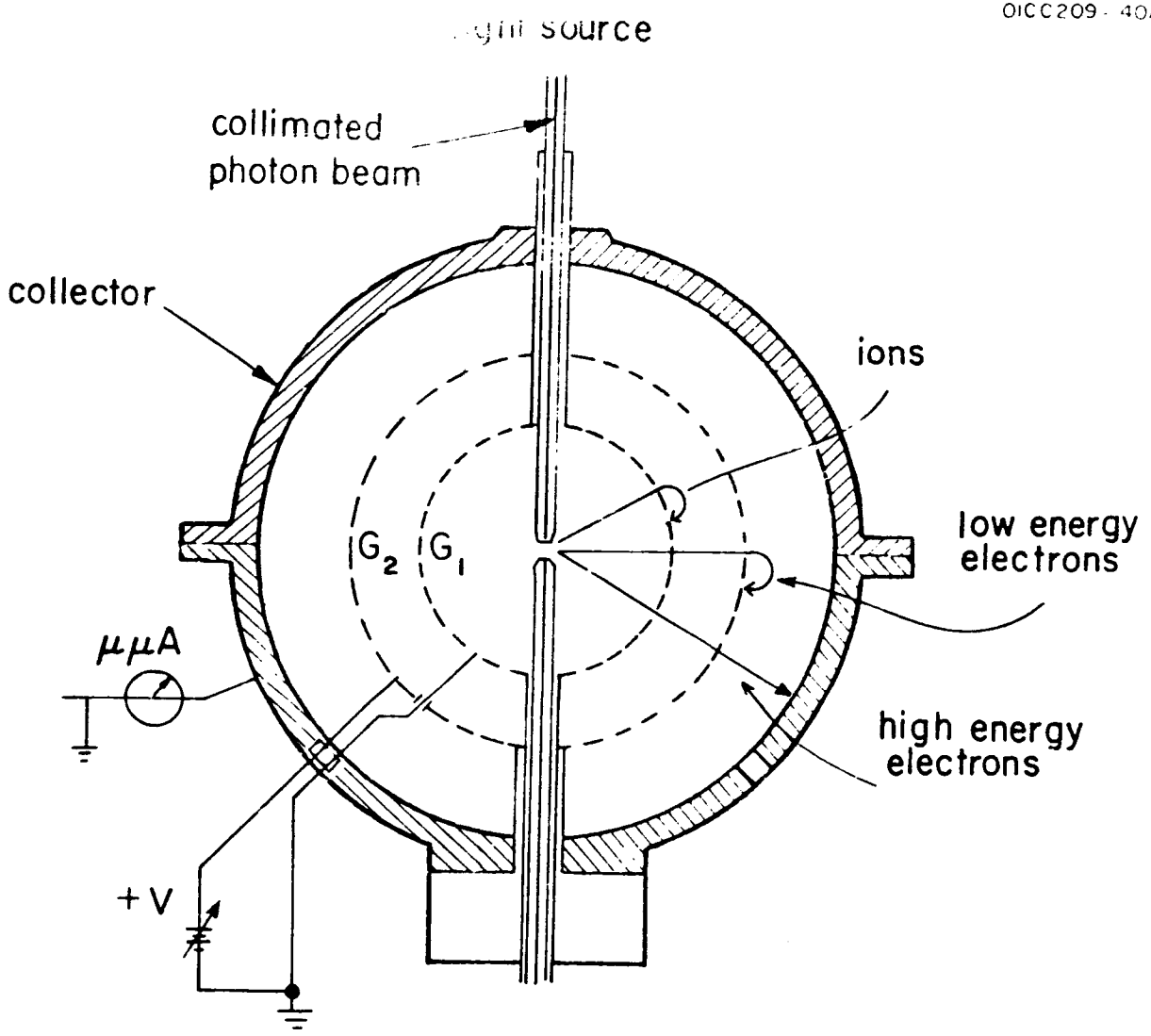

Figure 13. Electron energy analyzer. G_1 and G_2 are spherical screens surrounded by a solid spherical collector. The retarding potential V analyzes the energies of the electrons between G_2 and the collector (Courtesy D. Frost).(131)

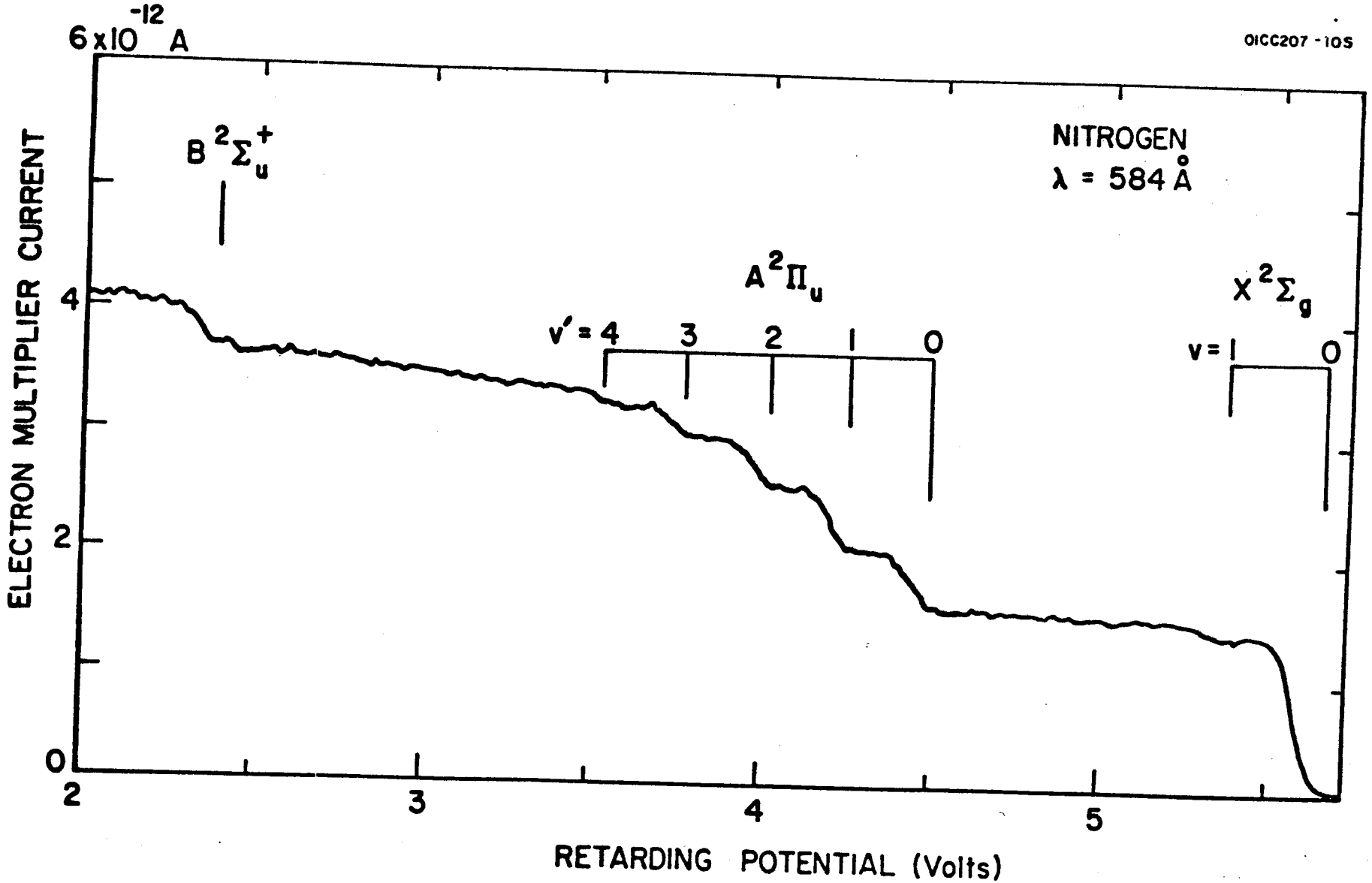

Figure 14. Electron energy spectrum of N_2 irradiated by 584Å. The step heights are proportional to the number of ions formed in these specific states.

At higher photon energies (primarily below 50Å), Carlson and Krause[132,133] have studied the charge distribution of the resulting ions and have used the measured kinetic energies of the photoelectrons to give more accurate values of the binding energies in the L shell of atoms.

The angular distribution of photoelectrons ejected from atoms has been predicted[134] to have the form $\alpha + \beta \sin^2 \theta$, where θ is the angle between the direction of the incident radiation and the ejected electron, and α and β are different matrix elements. No relation has been predicted for molecules. Measurements of the angular distribution have been made for atoms in the X-ray region and good agreement obtained with theory. Recently, Berkowitz and Ehrhardt[135] have measured the angular distribution for electrons ejected from Ar and Xe using 584Å radiation. Their results are in general agreement with theory. However, their preliminary measurements using N_2O have indicated a distribution which is nearly isotropic. In addition to the theoretical importance for establishing the angular distribution of ejected photoelectrons, this knowledge is again extremely important to problems of the upper atmosphere. A non-isotropic distribution means that the vertical flux of photoelectrons differs between noon and sunset and, thus, the electron heating of the atmosphere also changes.[136]

(c) Fluorescent radiation. In addition to studying the kinetic energies of electrons, it is possible to identify excited states of the ions by observing the fluorescent radiation emitted by the de-excitation

of these states. Figure 15 shows a hypothetical diagram for the absorption of 584Å radiation where both fluorescence and photoelectron ejection can occur. In the diagram, X is considered to be the ground state of the molecule with an ionization potential of 11 eV and X^+ is the ground state of the ion. The absorption of the 584Å radiation will be divided among the various vibrational and electronic states. The energy difference between an excited state energy level and the photon energy represents the energy carried away by the photoelectron. This energy difference is shown to the right of the diagram. Simultaneously with photoelectron ejection, the excited states will decay emitting fluorescent radiation. This is shown schematically on the left of the diagram.

Combining two monochromators, Schoen et al.[137] observed quantitatively the fluorescent radiation from $N_2^+(B\ ^2\Sigma_u^+)$. With higher resolution, Judge et al.[138] resolved the vibrational structure of the first negative band system of N_2^+; namely, $B\ ^2\Sigma_u^+ \rightarrow X\ ^2\Sigma_g$. Although observation of fluorescent radiation from excited ions yields similar information on Franck-Condon factors and on the specific absorption processes as measurements on the kinetic energies of the photoelectrons, the fluorescent technique has the advantage of higher resolution, especially if a spectrograph is used to photograph the fluorescent radiation. The method of exciting fluorescent radiation by the use of a monochromatic beam of vacuum ultraviolet radiation provides a less ambiguous method for analyzing rotational and vibrational structure than the conventional method using a gas discharge. In addition, it provides one of the few

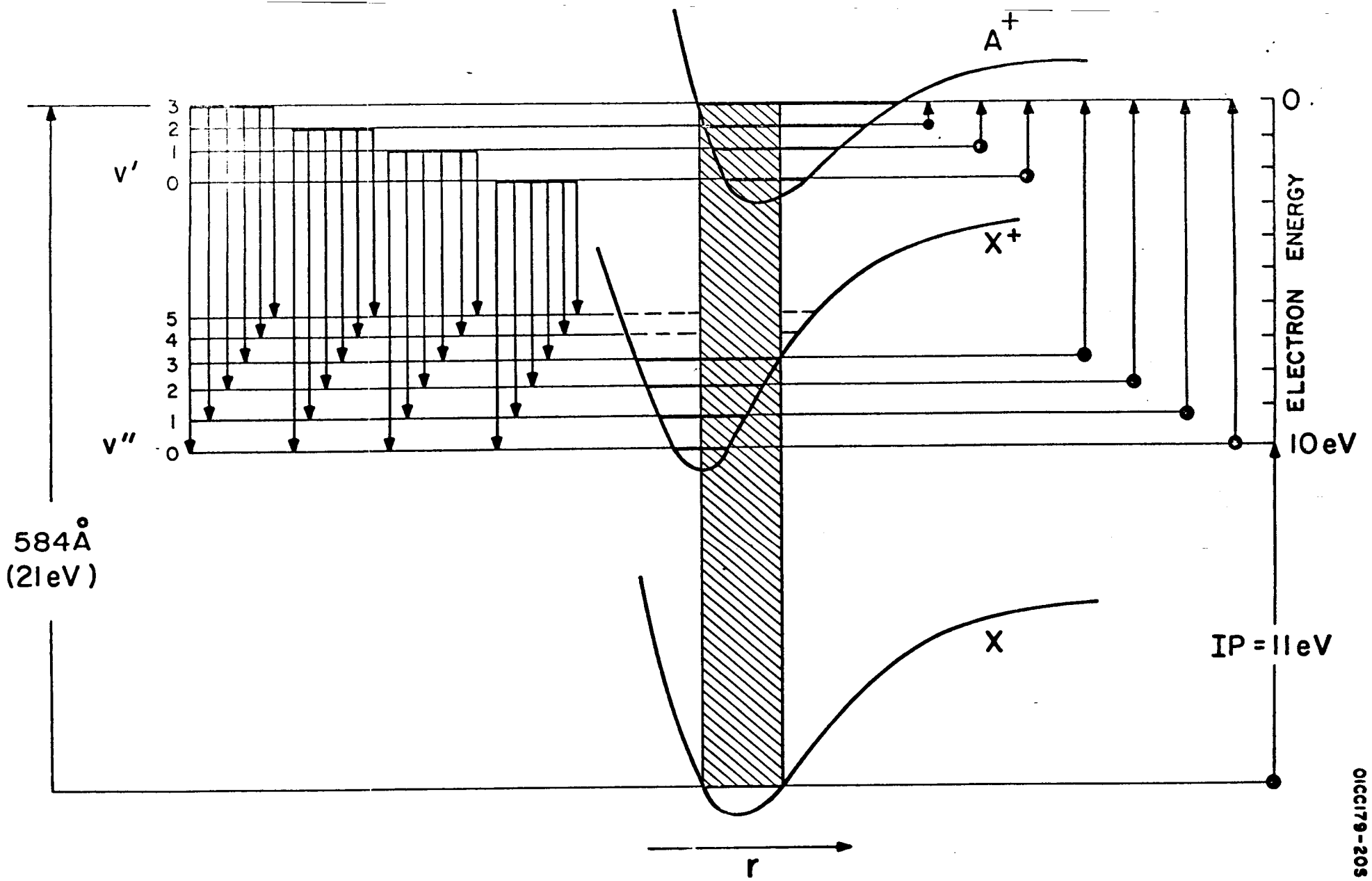

Figure 15. Potential energy curves for a hypothetical molecule illustrating the production of fluorescence and photoelectrons due to the absorption of 584Å radiation.

direct methods for observing specific absorption processes when the absorbed radiation does not ionize the gas. This additional technique to photochemistry has been demonstrated by Becker and Welge[139] and by Beyer and Welge.[140]

(2) Vacuum ultraviolet interactions with solids

When radiation is incident on a solid, a fraction will be reflected (R), transmitted (T), and absorbed (A). The total interaction is expressed by the relation R + T + A = 1. The structure and optical properties of solids can be studied by measuring these parameters.

(a) Reflectance. The reflectance of an absorbing material is given by the generalized Fresnel equations; namely,

$$R_{\perp} = \frac{a^2 + b^2 - 2a \cos\theta_i + \cos^2\theta_i}{a^2 + b^2 + 2a \cos\theta_i + \cos^2\theta_i} \tag{11}$$

and

$$R_{\parallel} = R_{\perp} \frac{a^2 + b^2 - 2a \sin\theta_i \tan\theta_i + \sin^2\theta_i \tan^2\theta_i}{a^2 + b^2 + 2a \sin\theta_i \tan\theta_i + \sin^2\theta_i \tan^2\theta_i} \tag{12}$$

where

$$2a^2 = [(n^2 - k^2 - \sin^2\theta_i)^2 + 4n^2k^2]^{\frac{1}{2}} + (n^2 - k^2 - \sin^2\theta_i)$$

and

$$2b^2 = [(n^2 - k^2 - \sin^2\theta_i)^2 + 4n^2k^2]^{\frac{1}{2}} - (n^2 - k^2 - \sin^2\theta_i).$$

n is the real part of the index of refraction and k is the extinction coefficient. The complex index of refraction is equal to $(n - ik)$. The

angle of incidence is denoted by θ_i. Thus, in principle, the optical constants $\underline{n}$ and $\underline{k}$ could be obtained from Eqs. (11) and (12) by simply measuring the reflectance of a material using plane polarized radiation. In practice, unpolarized or partially polarized radiation is used, and the reflectance is then measured at two or more angles of incidence.[141] The reflectance R is related to Eqs. (11) and (12) by the relation,

$$R = 1/2\, R_{\perp} (1 + P) + 1/2\, R_{\parallel} (1 - P), \tag{13}$$

where P is the degree of polarization. The optical constants of aluminum as obtained by Hunter[142] are shown in Figure 16. Although several groups[142-148] are involved with measurements of optical constants, very few data exist, especially at wavelengths below 500Å.

(b) Transmittance. The transmission onset for a metal has been predicted to occur at the plasma frequency ν_p given by

$$\nu_p = (ne^2/\pi m)^{\frac{1}{2}}, \tag{14}$$

where $\underline{n}$ is the number of electrons participating in the plasma oscillations.[149,150] For many metals, the experimental values for the onset of transmission are in good agreement with Eq. (14) when $\underline{n}$ is taken to be the number of valence electrons.[151-153] However, in other metals such as gold and silver, there is no agreement. Assuming the validity of Eq. (14), measurements of ν_p should provide information of the number of electrons participating in the plasma oscillations. The inverse process of exciting plasma oscillations by bombarding thin metal foils with 60 to 100 keV electrons and observing the radiation produced by the

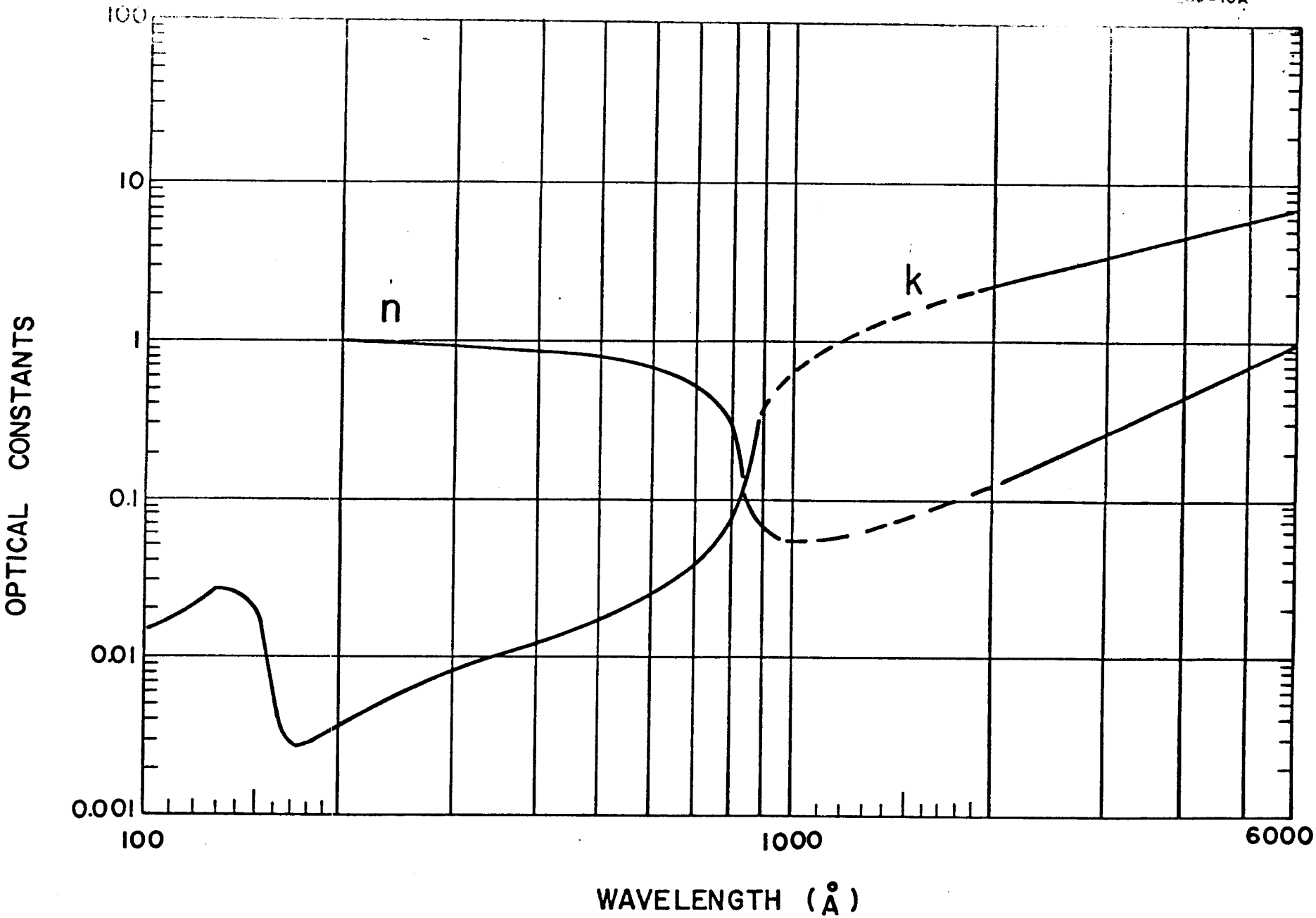

Figure 16. Optical constants of aluminum between 100 and 6000Å (courtesy W.R. Hunter).[142]

decay of the oscillations has been investigated by Arakawa et al.[154] Bombarding aluminum, they observed a continuum between 750 and 950Å with a maximum at 815Å. For aluminum, Eq. (14) predicts a plasma oscillation at 775Å, while the onset for transmission occurs at about 800Å.

Most metals exhibit sharp decreases in transmission at shorter wavelengths. These decreases may be due to interband transitions[155] or to the ejection of electrons from inner shells. To locate the position of these "edges" and to determine ν_p, it is necessary to obtain only relative transmittance data. Generally, however, the transmittance is measured absolutely in order to calculate the absorption coefficient of the solid as a function of wavelength.

(c) Absorptance. Measurements of the absorptance $A = 1 - R - T$ and of the absorption coefficient $\underline{k}$ defined by $kx = \ell n(I_o/I)$, where x is the thickness of the solid, and I_o and I are the intensities of the radiation entering and leaving the solid, respectively, can provide information on the band structure in dielectric and semiconducting crystals.[95,156-158] Knowledge of the absorption bands of crystals can be increased by measuring the absorption as a function of temperature or studying the effects of X-irradiation on the absorptance.

If the incident radiation is sufficiently energetic, the absorption interaction manifests itself partially by the appearance of photoelectrons. In certain crystals, photoconductivity effects or luminescence may also be observed.[159] Thus, studies of

these specific interactions will lead to a more complete understanding of the solid state structure. Photoelectrons ejected from a metal by low energy vacuum ultraviolet radiation originate from the filled conduction band, as shown in Figure 17. More energetic radiation can eject an electron from perhaps the L-shell. If such a vacancy is created, it can be filled by any electron from the conduction band. The radiation which is emitted in this "de-excitation" process is not monochromatic, but is spread out onto a band of frequencies. The width of this emission band is equal to the width of the conduction band. This is shown schematically to the right of Figure 17. The intensity of the emission as a function of frequency is related to the population density N(E) of the energy states in the conduction band.[101] Returning to the photoelectrons ejected from the conduction band, an analysis of their kinetic energies should also give information of N(E) provided these primary energies are not changed by collisions within the volume of the metal.[160-162]

These are only a few of the applications of vacuum ultraviolet radiation to basic research problems; many more exist. On the practical side, greater use is being made of this spectral region. As an immediate example, consider the problem of identifying trace impurities of CO in N_2. Since the difference in their molecular weights is only one part in 10^4, a very high resolution mass spectrometer is required to separate the two masses. However, if vacuum ultraviolet radiation is used to ionize the gas within the mass spectrometer ion chamber, a wavelength can be chosen which will ionize CO but not N_2, since their ionization potentials differ by about 1.4 eV (90Å). Thus, a very simple mass spectrometer can be used to identify the presence of CO in nitrogen.

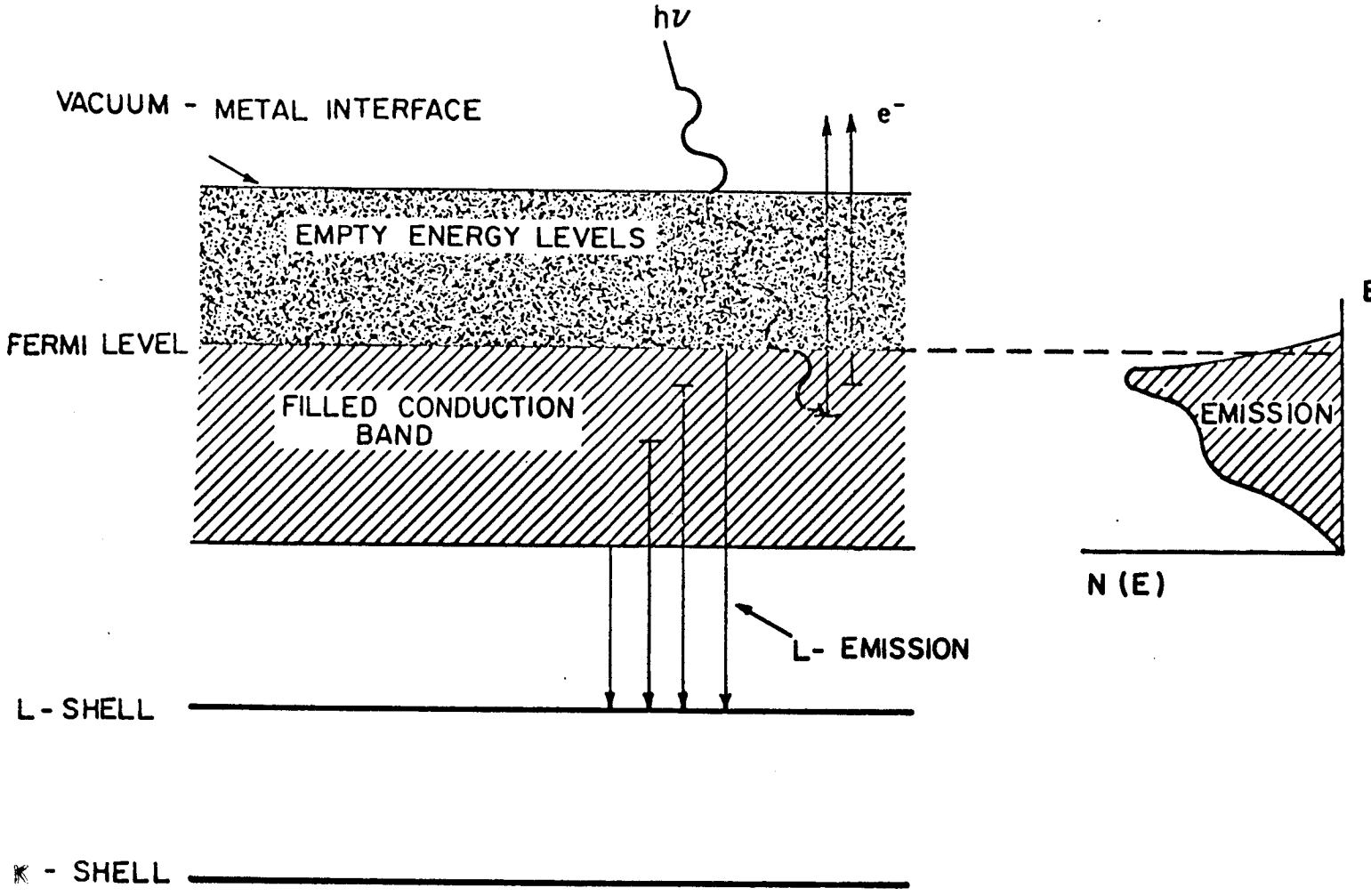

Figure 17. Energy levels in a metal. Electron transitions to a vacancy in the L-shell give rise to a continuum band of radiation, the distribution of which is related to N(E), the population density of the energy states in the conduction band.

3. The Relative Photoelectric Yield and Transmittance of Aluminum Films

A requirement under the current program involves the design, development, and construction of new experimental devices such as windows, filters, counters, etc., if and when necessary, for proper performance of the VUV and EUV investigations. During the current quarter, measurements have been performed of the transmittances and the photoelectric emissions from both the front and back faces of two unsupported thin aluminum films, 1380 and 470Å thick. The ultimate objective of the work is two-fold. First, the magnitude of the photoelectric emission from the back face is a parameter of interest in the design of certain photon detectors, e.g. ionization chambers, which might utilize thin metal films as selective filters. Second, the combined transmittance-photoemission data might contribute to an increased understanding of the processes of photon absorption and electron excitation and ejection from metals.

In Figure 18 are shown the transmittances of the two films in the wavelength region 720 to 400Å. The transmittances do not increase monotonically toward shorter wavelengths, but have structure similar to that reported by Hunter[163] and by Rustgi.[164] The transmittance data could not be quantitatively accounted for if the two films were assumed to be of pure aluminum since, at any given wavelength, different values of the absorption coefficient μ_{Al} were obtained. It is known that evaporated aluminum films exposed to air at atmospheric pressure rapidly form Al_2O_3 surface layers which have a terminal thickness.[165] Either interference effects due to reflections at the air-Al_2O_3 and Al_2O_3-Al boundaries

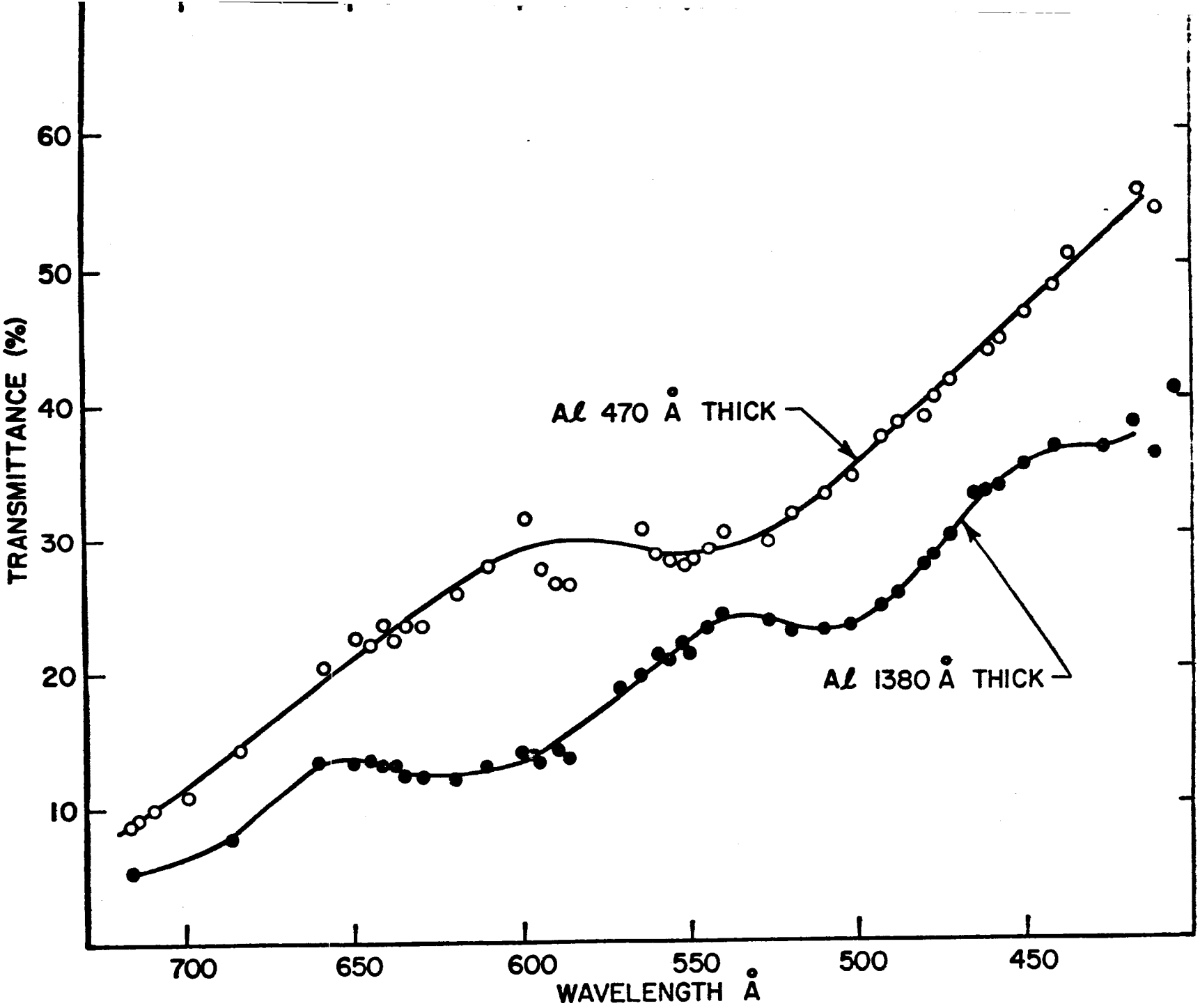

Figure 18. The transmittance of thin unsupported Aℓ films.

or suitably varying absorption coefficients μ_{Al} and $\mu_{Al_2O_3}$ could then give rise to the periodic structure in the transmission curves and could account for the dependence of this structure on the film thickness. While the photoelectric emission measurements, described in the following paragraph, support the contention of Hunter[164] that the structure is due to interference effects, it is worth noting that if boundary reflections are small and can be ignored, the coefficient μ_{Al} can be calculated from the data given in Figure 18 since

$$\mu_{Al} = \frac{1}{(1380 - 470)10^{-8}} \left[\ell n \frac{I_o}{I_{1380}} - \ell n \frac{I_o}{I_{470}} \right] \text{ cm}^{-1}$$

where I_o is the intensity of radiation incident upon the films and I_{1380} and I_{470} are the intensities of radiation transmitted through the 1380 and 470Å thick films, respectively. To obtain this expression, all the oxide surface layers were assumed to have the same thickness. Values of μ_{Al} calculated at all the measured wavelengths were within the range 9 to 2 x 10^4 cm^{-1}. These values are to be compared with published values of about 7 x 10^4 cm^{-1} at 720Å, dropping to about 4 x 10^4 cm^{-1} at 400Å.[166]

In Figures 19a and 19b are shown, as a function of wavelength, relative values of the photoelectric yields from both the front and back faces of the thin aluminum films. As was expected, the yield from the front face attained maximum values and from the back face minimum values at wavelengths where the transmittance was minimal. If the observed variations in transmittance and, hence, in yield were due to changes in the effective absorption coefficient of the Al-Al_2O_3 film, the photoelectric yield of a thick opaque Al_2O_3 surfaced Al photocathode should

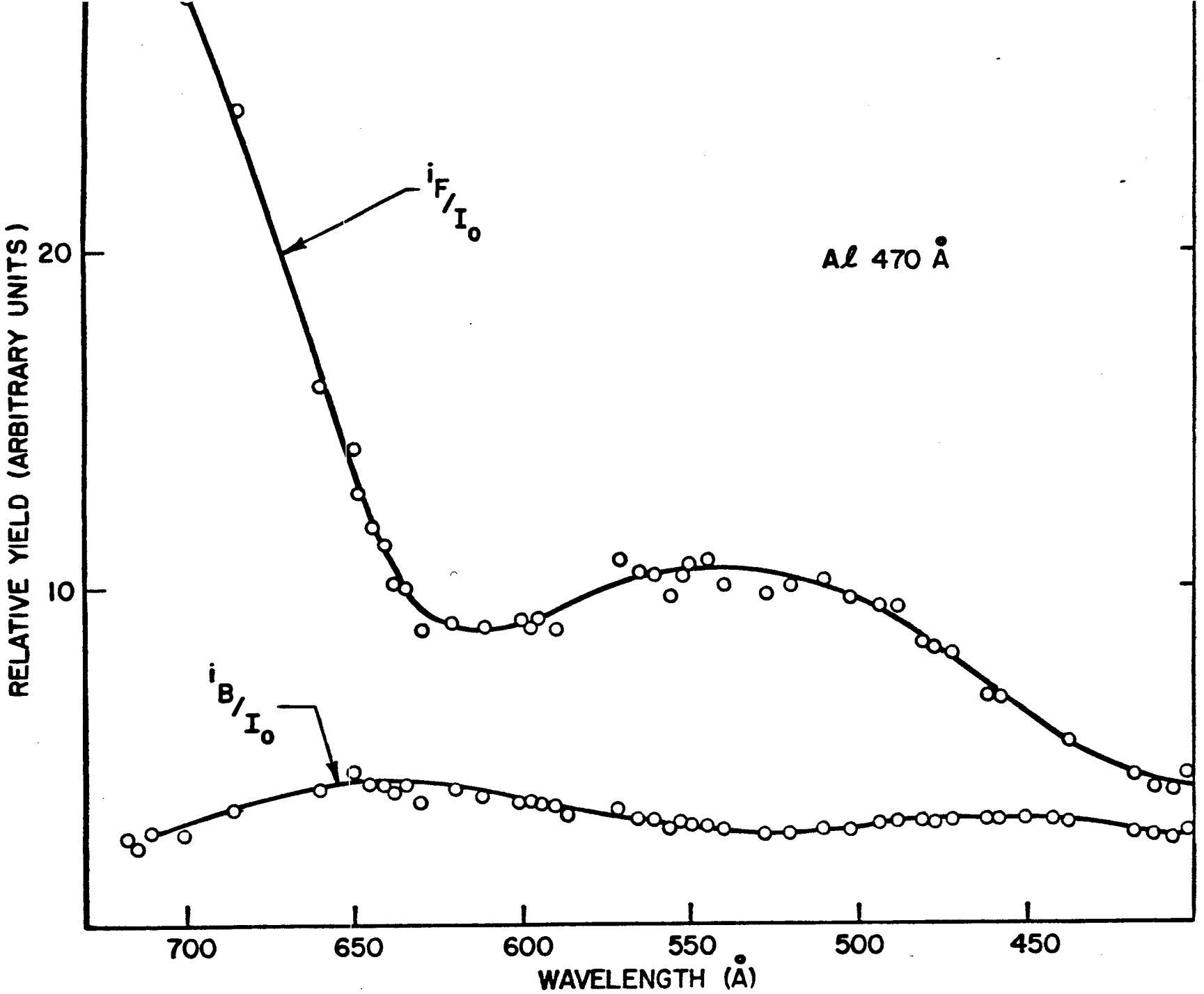

Figure 19a. The relative photoelectric yield from the front fact (i_F/I_o) and from the back face (i_B/I_o) of a 470Å thick Aℓ film.

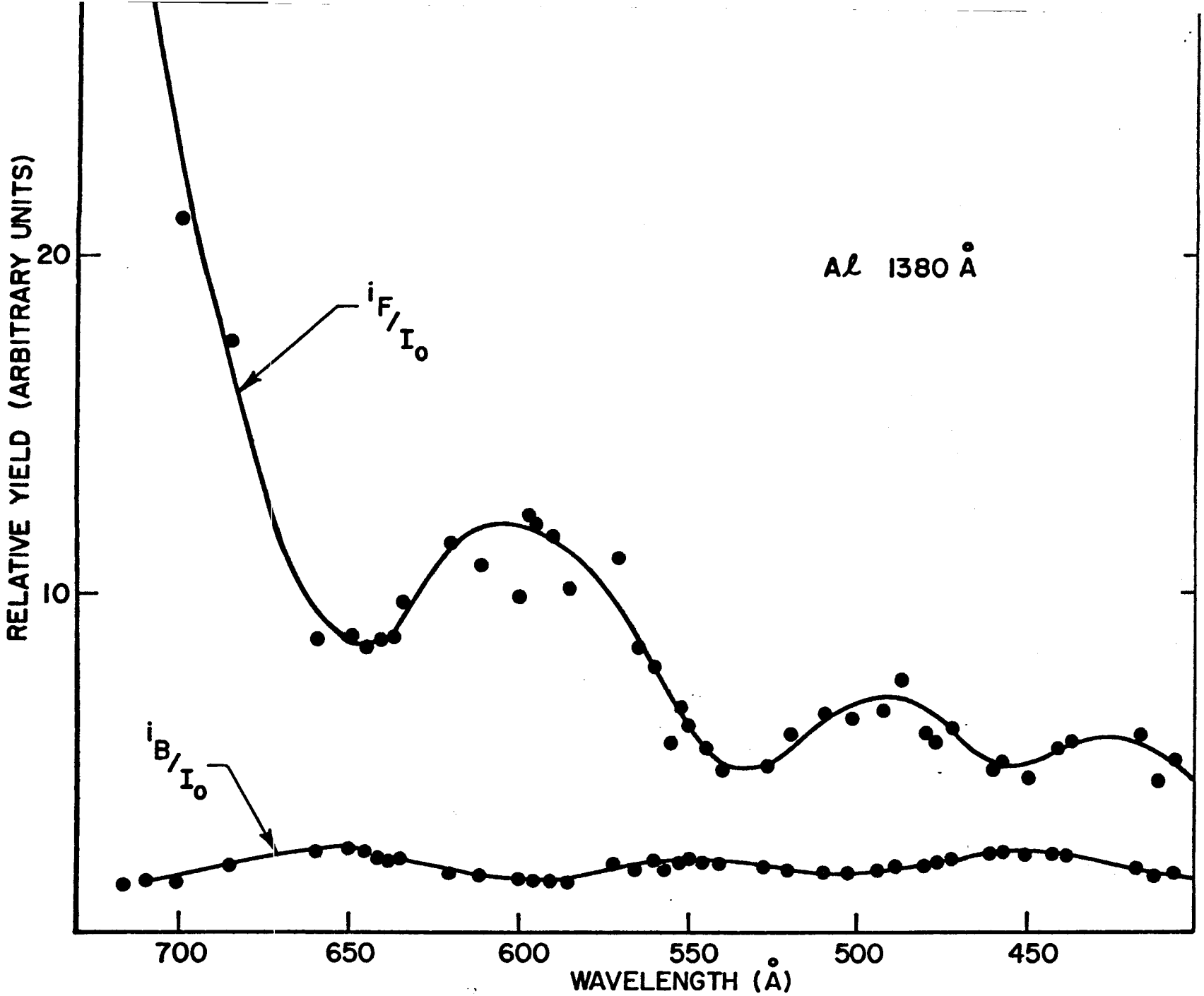

Figure 19b. The relative photoelectric yield from the front face (i_F/I_o) and from the back face (i_B/I_o) of a 1380Å thick Al film.

also vary periodically with wavelength. However, if the periodic variation of yield of the thin films is due to interference effects, no similar variations would be expected for a thick opaque photocathode. An absence of such fine structure has been reported for Aℓ photocathodes[167] which supports the fact that interference effects account for the detailed shape of both the yield and transmission curves of the thin films.

D. THEORETICAL AND EXPERIMENTAL PLANETARY AERONOMY

For convenience, the results which have been achieved under planetary aeronomy are under theoretical and experimental investigations.

1. Theoretical Investigations in Planetary Aeronomy

The specified theoretical planetary aeronomy tasks under the current contract include the following investigations: (a) the observation of noctilucent clouds in planetary atmospheres, (b) the role of interplanetary debris in planetary atmospheres, (c) the role of fluorescence in planetary atmospheres due to EUV photoionization, and (d) the role of fluorescence in planetary atmospheres due to the solar wind alpha particle.

During the current reporting period, significant progress has been achieved under Item (a), as reported below.

a. On the observation of noctilucent clouds in planetary atmospheres

A task under the current program involves investigation of noctilucent clouds in the Earth and planetary atmospheres. In a recent

paper,[168] Marmo et al. have demonstrated the feasibility of performing global observations on noctilucent clouds in the Earth's atmosphere using a satellite-borne spectrophotometer operating in the vacuum ultraviolet spectral region at about 1800Å. During the current reporting period, a similar study was performed to evaluate the feasibility of photographically observing noctilucent clouds in the Earth's atmosphere from an orbiting satellite. Additionally, an opportunity to perform a meaningful experiment aboard the Gemini XII mission had become available. To the best of our knowledge, the investigative results reported herein were employed in planning and executing the sunrise-dust photographic experiment of Gemini XII. The preliminary examination of the problem was predicated on an overhead illuminating sun situation which is reported in detail below. Although the results of this study indicate that valuable data could be obtained from an experiment of this configuration, it was decided to perform sunrise observations for several reasons to be examined in greater detail in a subsequent section.

For the overhead sun situation, a number of experimental constraints were imposed such as the availability of a specific experimental camera probe and a limited involvement by the astronaut. Specifically, these constraints included:

1. performance of the experiment during the solar-illuminated portion of the pertinent orbit,

2. the somewhat restrictive Gemini XII orbital geometry, which is discussed in greater detail below,

3. the experimental instrumentation is a camera equipped with LiF-quartz lenses which transmit to wavelengths as low as 2000Å,

4. the lens speed, focal length, film type, and filter availability are established, as discussed below,

5. astronaut demands limit the experimental extent to no more than five successive exposures.

The overhead illumination analysis indicates that even under the above constraints, a meaningful experiment can be performed involving the photographic observation of terrestrial dust in the ultraviolet region of the spectrum, i.e., about 2250 to 2450Å. This capability will be demonstrated in the following discussions which represent the initial GCA input into the proposed Gemini XII experiment.

The measurement of several dust configurations could be attempted, and it appears that solar-illuminated noctilucent clouds afford the highest probability of success in the present case. The possibility of observing other dust manifestations (such as those observed by Fiocco et al.[169]) ultimately depends on the sensitivity of the experimental technique involved. It will be shown subsequently that while successful photography of noctilucent clouds appears quite high, there is a finite possibility that other dust configurations may also be observed (including ultra-thin noctilucent clouds) where the local particulate number density amounts to only about 1 cm^{-3}. The following sections include brief technical discussions on the salient features of the proposed experiment.

(1) General remarks on the nature and occurrence of noctilucent clouds

Although an extensive discussion of the many scientific aspects of noctilucent clouds is inappropriate here, selected features are presented which bear on the character, nature, and occurrence of such clouds since these aspects are of prime importance in determining the probability of observing noctilucent clouds. Most of the descriptive material included in the present section has been extracted from Soviet 1957-1958 IGY data[170] because it represents a relatively-large data sample which was readily available.

Although the occurrence and sightings of noctilucent clouds are relatively rare events, a contributing factor may involve the fact that ground-based observations are only possible during morning and evening twilight conditions. To emphasize this point, the frequency of appearance of noctilucent clouds is shown in Figure 20 as a function of solar depression angle. It is evident that for all practical purposes, noctilucent clouds are generally observed only when the solar depression angle is between 6 and 16 degrees with maximum observation occurring between 8 and 12 degrees. Clearly, the time duration for which these conditions exist in a given day is a function of both latitude and season. For example, at latitudes of 63, 56, 50, and 30 degrees, the maximum Earth-based viewing time periods for a given twilight are 3, 2, 1, and 1/2 hour, respectively. This is considered to be a basic factor which influences the observed latitudinal variation of the frequency of sightings of noctilucent clouds as shown in Figure 21. On the other

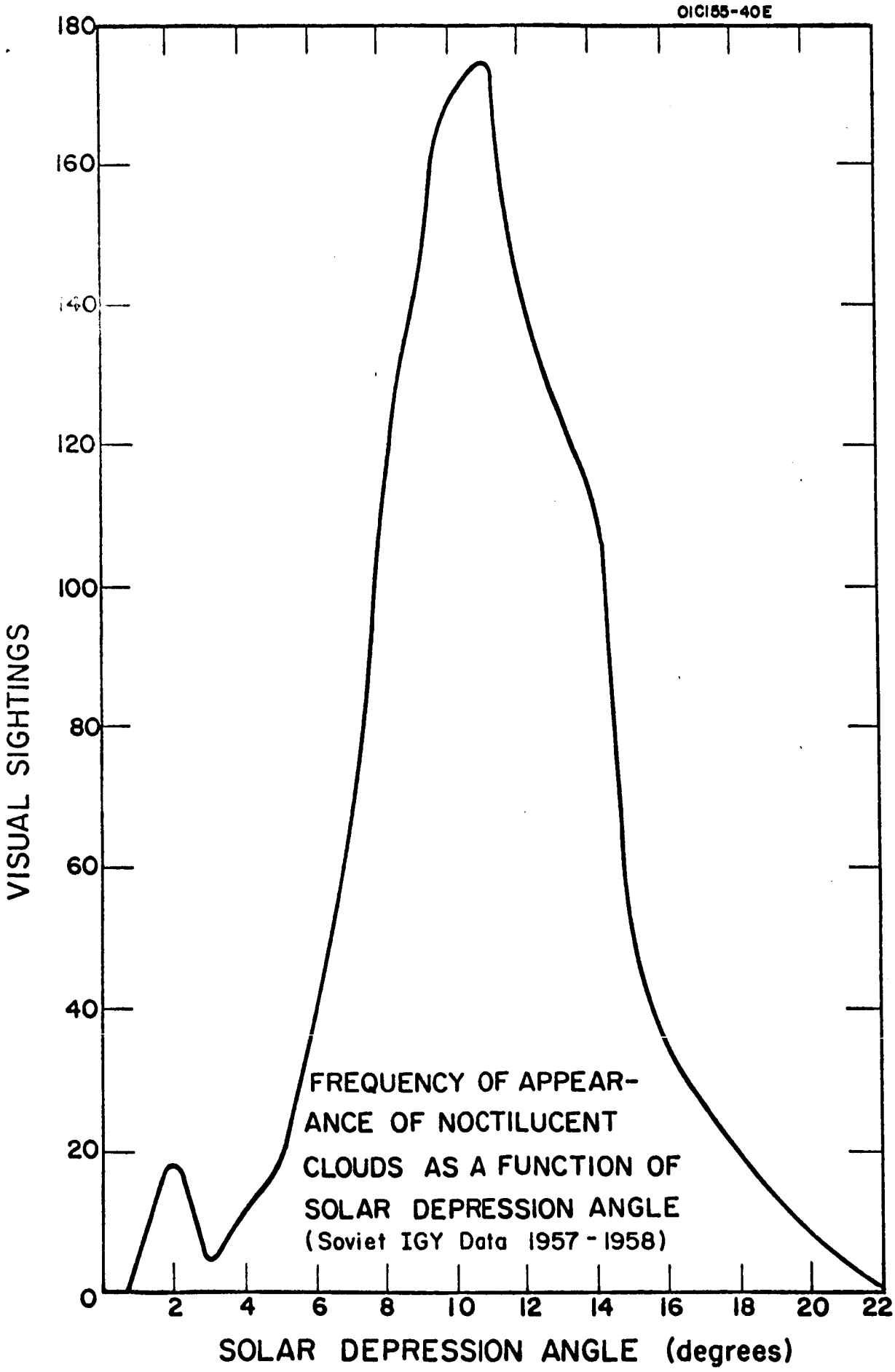
01C155-40E
VISUAL SIGHTINGS
180
160
140
120
100
80
60
40
20
0
2
4
6
8
10
12
14
16
18
20
22
SOLAR DEPRESSION ANGLE (degrees)
FREQUENCY OF APPEAR-
ANCE OF NOCTILUCENT
CLOUDS AS A FUNCTION OF
SOLAR DEPRESSION ANGLE
(Soviet IGY Data 1957 - 1958)

Figure 20

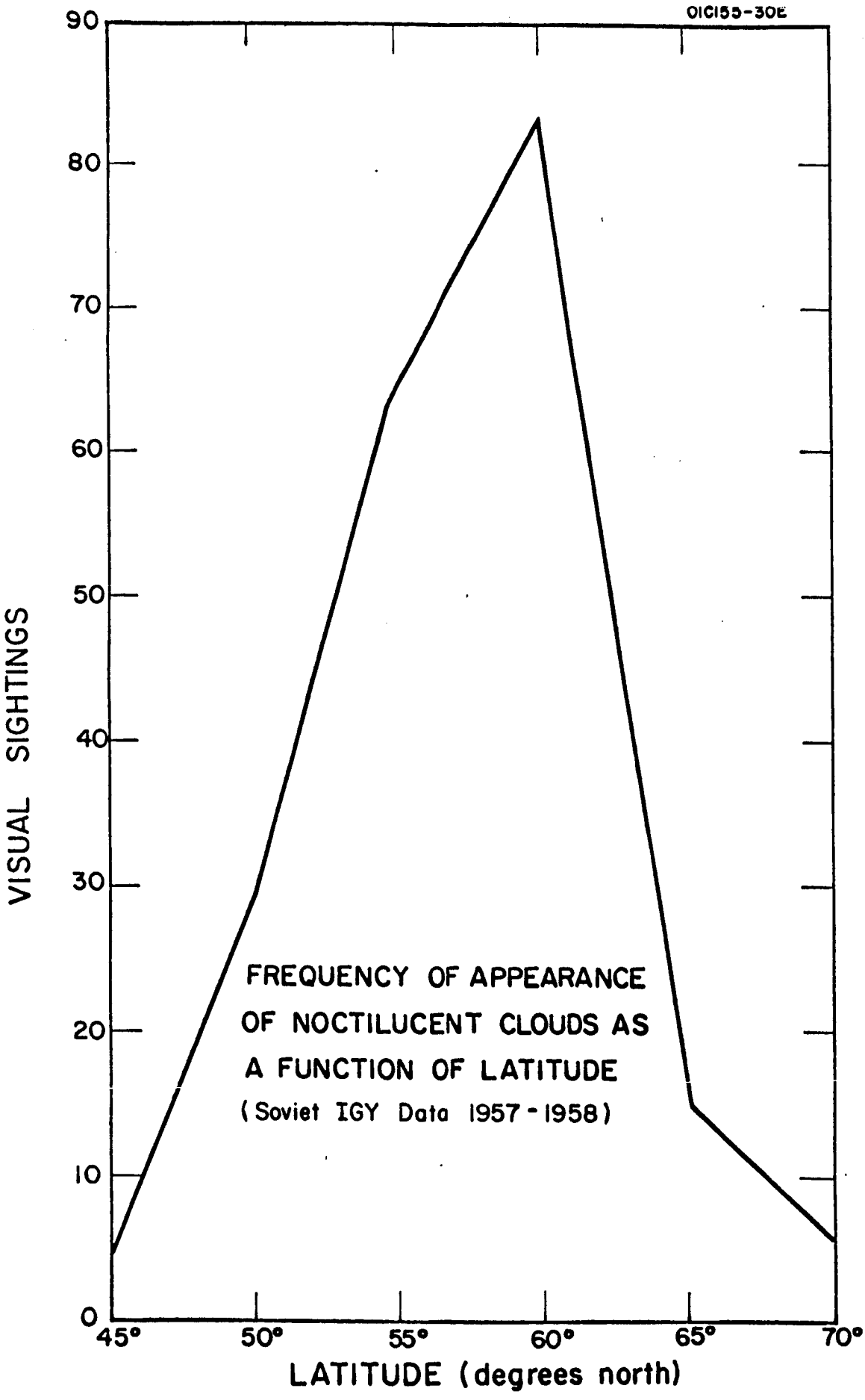
01C155-30E
VISUAL SIGHTINGS
90
80
70
60
50
40
30
20
10
0
45°
50°
55°
60°
65°
70°
LATITUDE (degrees north)
FREQUENCY OF APPEARANCE
OF NOCTILUCENT CLOUDS AS
A FUNCTION OF LATITUDE
(Soviet IGY Data 1957 - 1958)

Figure 21

hand, it should be pointed out that there are scientific reasons for expecting that noctilucent clouds are formed preferentially at high latitudes. For similar reasons, cloud formation at high latitudes is facilitated during the summer months. Without discussing the scientific justification for this behavior, it is appropriate to illustrate this fact by the data shown in Figure 22 which give the seasonal frequency of sightings of noctilucent clouds. The data quoted herein represent Northern hemisphere observations, although it can be anticipated that similar results pertain during the Southern hemisphere summer. It should also be noted that noctilucent clouds are consistently observed to occur at an altitude of about 80 km within a spread of a very few kilometers. Additionally, the vertical extent of the clouds are only observed to be about 1 to 2 km.

A diurnal variation of the frequency and duration of noctilucent clouds has also been observed. It has been established that the ratio of morning-to-evening twilight sightings is about a factor or two. Deirmendjian and Vestine[171] have explained this predominance of morning appearances by the existence of more favorable pre-dawn hour conditions for water condensation. An alternative explanation for the observed morning twilight preference involves the fact that the relative number of meteoric impacts increases toward morning due to the dynamics of the Earth-meteors system.

Two important parameters required to calculate the expected signal strengths from solar-illuminated noctilucent clouds are

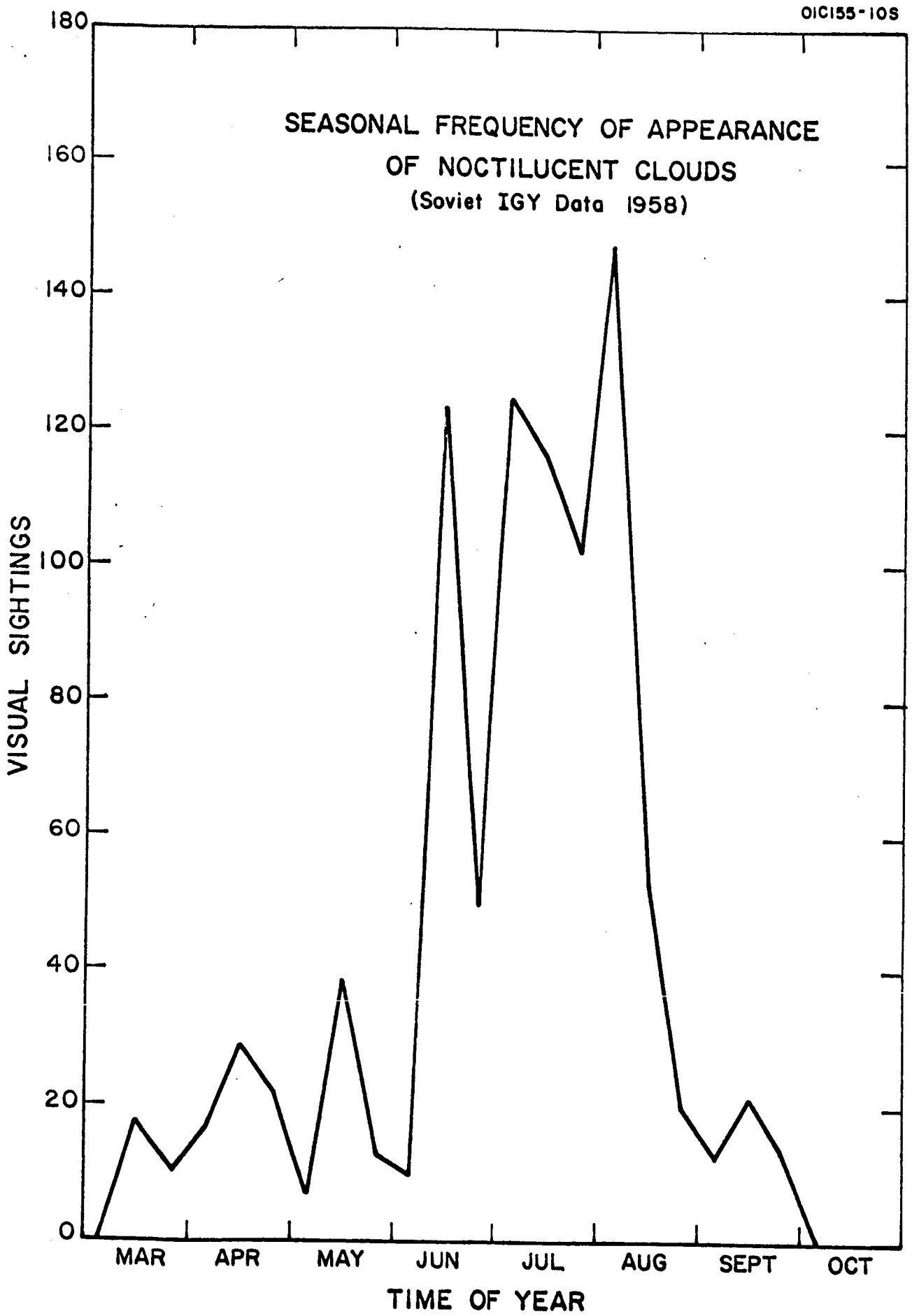
OICI55-IOS
SEASONAL FREQUENCY OF APPEARANCE
OF NOCTILUCENT CLOUDS
(Soviet IGY Data 1958)
VISUAL SIGHTINGS
180
160
140
120
100
80
60
40
20
0
MAR
APR
MAY
JUN
JUL
AUG
SEPT
OCT
TIME OF YEAR

Figure 22

the observed column count and size distribution of the particles. The best available data are those due to Hemenway et al.[172] who collected particles in situ by means of a rocket probe intentionally directed through noctilucent clouds. Two measured size distributions corresponding to different rocket flights are shown in Figure 23. It can be seen that only about 1 percent of the collected particles have a diameter of less than 0.05 microns while about 1 percent have diameters exceeding 0.3 microns. Hemenway has noted that most of the particles with diameters greater than 0.02 microns were ice-coated at the time of collection with the coating diameter about five times greater than that of the nucleus. Since the proposed observations involve wavelengths of about 2300Å, it is evident, from the range of measured cloud particle sizes, that the application of Mie scattering theory is required.

(2) Geometric constraints imposed by orbital characteristics

For the present calculation, the orbital characteristics of Gemini XII have been assumed fixed according to the following specifications: (a) the orbital inclination will be about 28.9 degrees and (b) a circular orbit is achieved at an altitude of 160 nautical miles, or about 300 km. In accordance with the data of Figures 20, 21, and 22, it is pertinent to investigate the probability of successfully observing noctilucent clouds under the above constraints. In the spectral region of interest, ozone absorption precludes observation of altitudes below about 60 km. Accordingly, this altitude has been considered to be a lower limit for line-of-sight observations from the satellite. Another

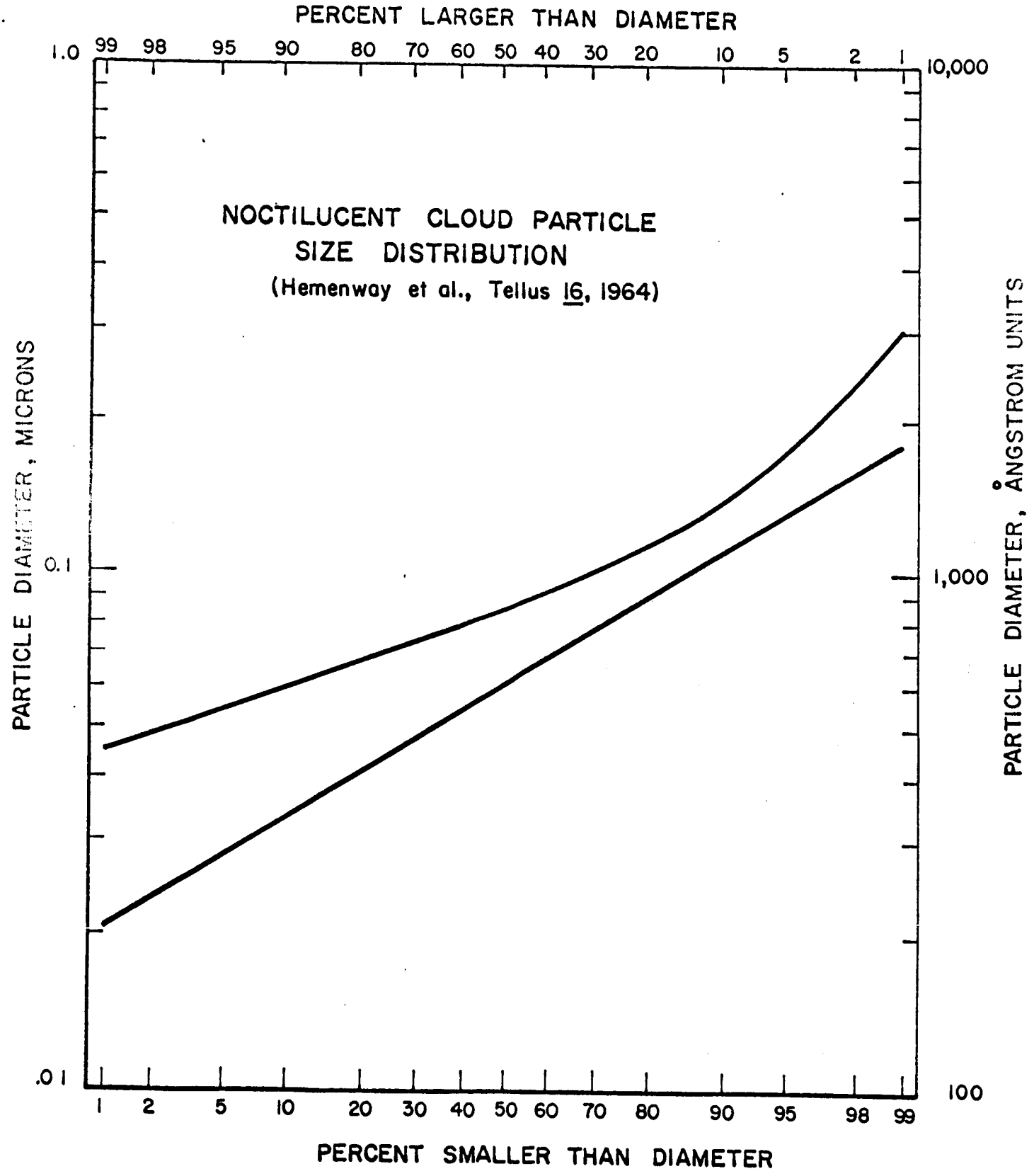
PERCENT LARGER THAN DIAMETER
1.0 99 98 95 90 80 70 60 50 40 30 20 10 5 2 1
10,000
NOCTILUCENT CLOUD PARTICLE
SIZE DISTRIBUTION
(Hemenway et al., Tellus 16, 1964)
PARTICLE DIAMETER, MICRONS
0.1
.01
1,000
100
PARTICLE DIAMETER, ÅNGSTROM UNITS
1 2 5 10 20 30 40 50 60 70 80 90 95 98 99
PERCENT SMALLER THAN DIAMETER

Figure 23

constraint imposed by a 60-km ultraviolet screening height and the Earth-sun geometry which pertain for the projected satellite flight schedule times is that the highest northern latitude which is sunlit at 80 km is only about 76 degrees, while at the South Pole this altitude is solar-illuminated. For the present orbit, however, whether the observations are performed in a northerly direction from 28.9°N or southerly direction from 28.9°S, the highest observable latitude for which an 80-km altitude tangency can be achieved aboard Gemini XII is only 43.6 degrees. Accordingly, with all other things equal, it would probably be more advantageous to observe in a northerly direction since the opportunity for ground observer verification is higher. These observations should optimumly be performed during morning twilight hours as discussed previously. If the planned operational satellite altitude is considerably higher than 300 km, a correspondingly higher probability of successful observation of noctilucent clouds could be anticipated since one could in principle probe a northern latitude as high as 76°. If the opportunity to probe still higher latitudes becomes available, southerly directed observations would clearly be pertinent for the present time of year.

(3) General features of the available optical probe

The optical instrumentation involved in the proposed experiment is the vacuum ultraviolet camera to be used principally by Dr. Carl Henize for the performance of stellar photography during the Gemini XII nightside orbits. The pertinent optical characteristics[173] of this instrument are specified below:

1. the camera is equipped with LiF-quartz lenses which transmit down to about 2000Å as illustrated in Figure 24 where the solid curve is supplied by the manufacturer and the dotted curve is an adjustment due to Henize on the basis of laboratory measurements.

2. the camera is equipped with an f 3.3 lens of 73 mm focal length,

3. the film format dimensions are about 70 mm by 48 mm,

4. Kodak IO film is employed in a magazine which accommodates five exposures,

5. a VUV filter is available (Thin Film Products, Inc.) whose transmission characteristics[174] are shown in Figure 25.

6. the convolved product of the transmissivities of the Thin Films filter and that of the camera furnished by the manufacturer is illustrated in Figure 26. It is evident that, for all practical purposes, the experimental observations are limited to the spectral region λλ 2250 to 2450Å.

(4) Background and signal calculations

The background and signal calculations described below will be employed subsequently to establish the feasibility of photographically recording solar-illuminated noctilucent clouds and other terrestrial dust layers in the ultraviolet spectral region.

(a) Background calculations. The background intensity varies in a complex manner as a function of the observer-look angle and the solar zenith and azimuth angles. For the present purpose, a simplified and representative geometrical configuration has been

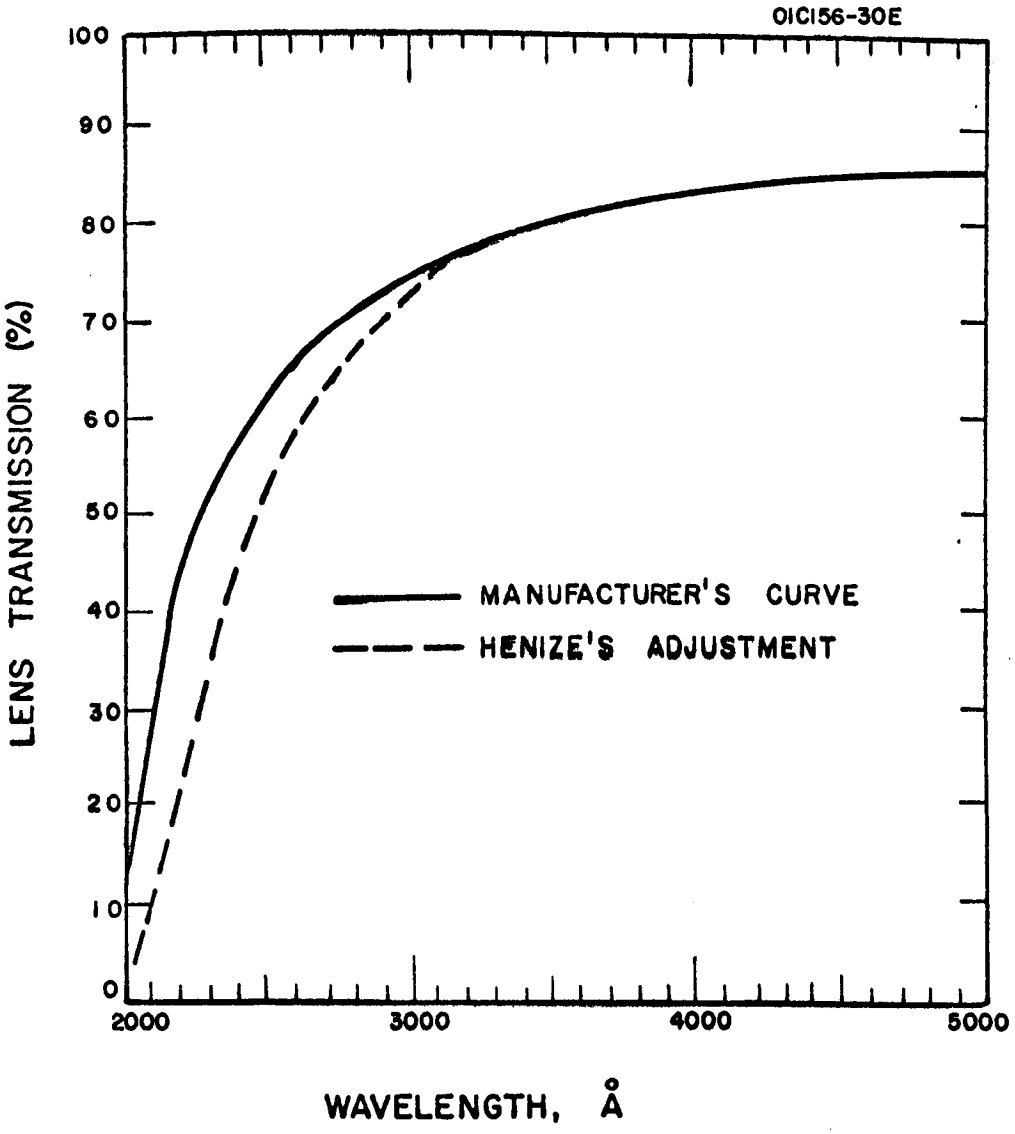
01C156-30E
100
90
80
70
60
50
40
30
20
10
0
LENS TRANSMISSION (%)
MANUFACTURER'S CURVE
HENIZE'S ADJUSTMENT
2000
3000
4000
5000
WAVELENGTH, Å

Figure 24

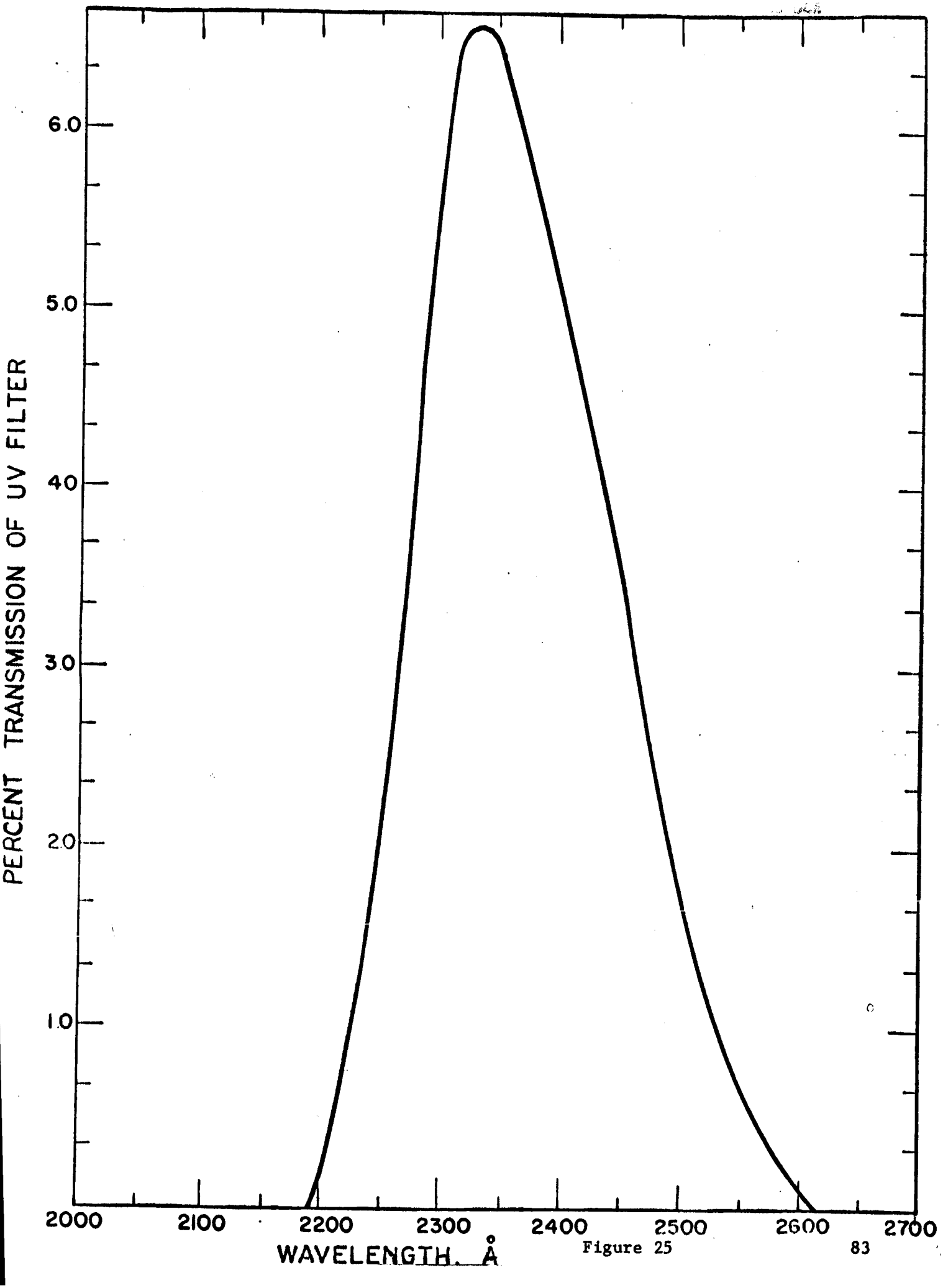
PERCENT TRANSMISSION OF UV FILTER
6.0
5.0
4.0
3.0
2.0
1.0
2000
2100
2200
2300
2400
2500
2600
2700
WAVELENGTH, Å

Figure 25

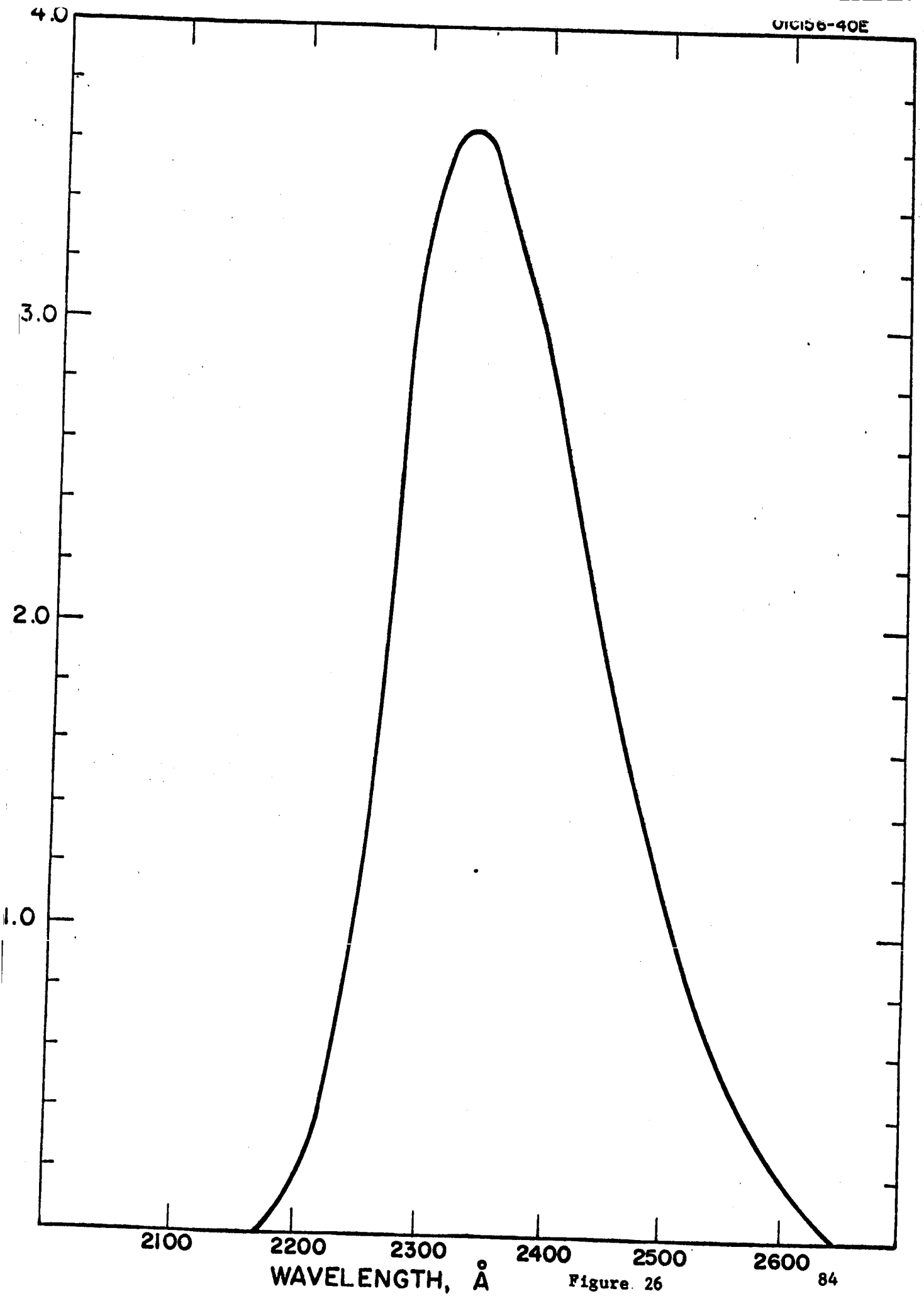

Figure 26

assumed to obtain background estimates from which a series of recommended exposure times can be derived. The assumed geometry involves a solar zenith angle of 90 degrees and an observation line-of-sight which is tangent to the Earth's surface at an altitude of 80 km.

For ray paths tangent to altitudes above 80 km, the background photon emission rate (Φ_h) was determined from the first-order formula:[175]

$$\Phi_h = P(\psi)\ \phi_s\ \sigma_r\ n_h\ H\ \Delta\lambda\sqrt{\frac{2\pi(R + h)}{H}}$$

where

ϕ_s = solar flux $\frac{\text{photons}}{\text{cm}^2\text{-sec-Å}}$

σ_r = Rayleigh scattering cross section $\frac{\text{cm}^2}{\text{mol}}$

n_h = the ambient number density at the level of tangency, h

H = ambient scale height

R = radius of the Earth

$\Delta\lambda$ = spectral bandpass of system = 200Å

$P(\psi)$ = Rayleigh phase function = $3/4(1 + \cos^2 \psi)$.

The Rayleigh phase function depends upon the scattering angle, ψ (which has been assumed to be 90°), so that $P(\psi)$ has a minimum value of 3/4.

For tangent altitudes below 80 km, the important role of ozone absorption must be considered. To estimate the background emission rates at these low altitudes, the following approximate numerical approach was employed. Above the 30 km level (below which

virtually no radiation penetrates), the ozone concentration profile can be approximated by an exponential decrease law with an effective scale height of 5 km.[176] For the present calculation, a striated atmosphere consisting of 5-km altitude increments has been assumed. Starting from a point P in the accompanying figure along the path BP to the observer at B, which makes an angle θ with the local horizontal through P,

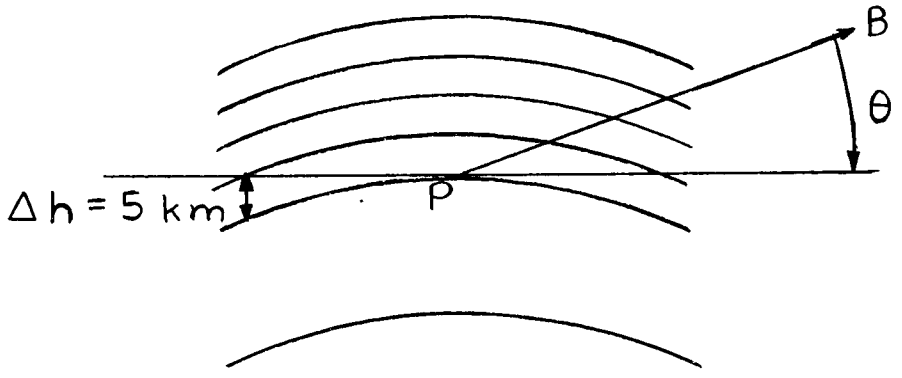

the emission rate as seen from B, (Φ_θ), is given by

$$\Phi_\theta = \sum_i \Phi_i$$

where the index, i, refers to the ith altitude increment, and

$$\Phi_i = P(\psi)\ \Phi_s\ \sigma_r (n_o \bar{H})_i\ \bar{F}_{\theta_i} \exp(-\tau_{v_i}) \exp(-\tau_{\theta_i})$$

where

$$\tau_{\theta_i} = F_{\theta_i}\ \tau_{v_i}$$

and

$$\tau_{v_i} \cong (n_i H_o)\, \sigma_a$$

where

$H_o \equiv$ ozone profile scale height (5 km)

$n_i \equiv$ ozone number density at the bottom of the ith altitude increment

$\sigma_a \equiv$ mean value of the ozone absorption cross section over the spectral bandpass taken to be 6.3×10^{-18} cm^2.[177]

The quantity τ_{v_i} represents the vertical optical depth for the illuminating solar flux. The quantity τ_{θ_i} represents the optical depth along the ray BP, while the quantity F_{θ_i} is Swider's angular enhancement factor.[175] The quantity $P(\psi)\phi_s\sigma_r$ was calculated to be 8.66×10^{-14} photons/sec-Å.

The results of employing this approximate calculation are summarized in Figures 27 and 28. In the former, the background emission rate in kilorayleighs is plotted against two scales: (a) the distance on the film format in millimeters and (b) the angular displacement in degrees from the center line-of-sight. For ready reference, the 80 km altitude above the Earth's surface is denoted by a solid line intersecting the curve. In Figure 28, the background emission rate is shown as a function of the tangent altitude. It can be seen that considerable brightness exists at the 80 km level over the restricted experimental bandpass amounting to several hundred kilorayleighs. It will be shown subsequently that this background level can be observed photographically using reasonable exposure times. The above results also indicate that the real Earth horizon cannot be distinguished since ozone absorption precludes its detection. The shape

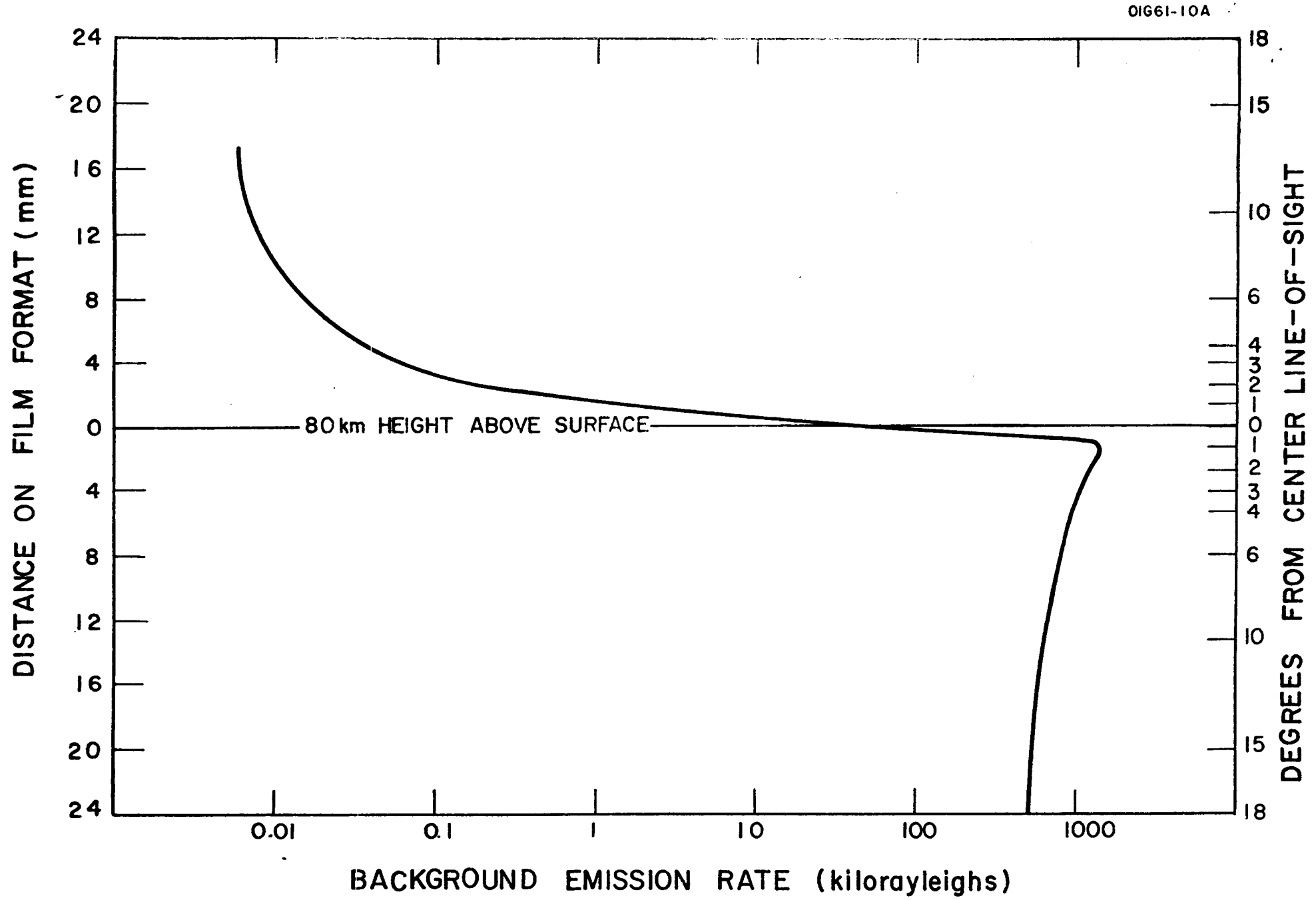
01G61-10A
DISTANCE ON FILM FORMAT (mm)
24
20
16
12
8
4
0
4
8
12
16
20
24
80 km HEIGHT ABOVE SURFACE
0.01
0.1
1
10
100
1000
BACKGROUND EMISSION RATE (kilorayleighs)
DEGREES FROM CENTER LINE-OF-SIGHT
18
15
10
6
4
2
0
2
4
6
10
15
18

Figure 27

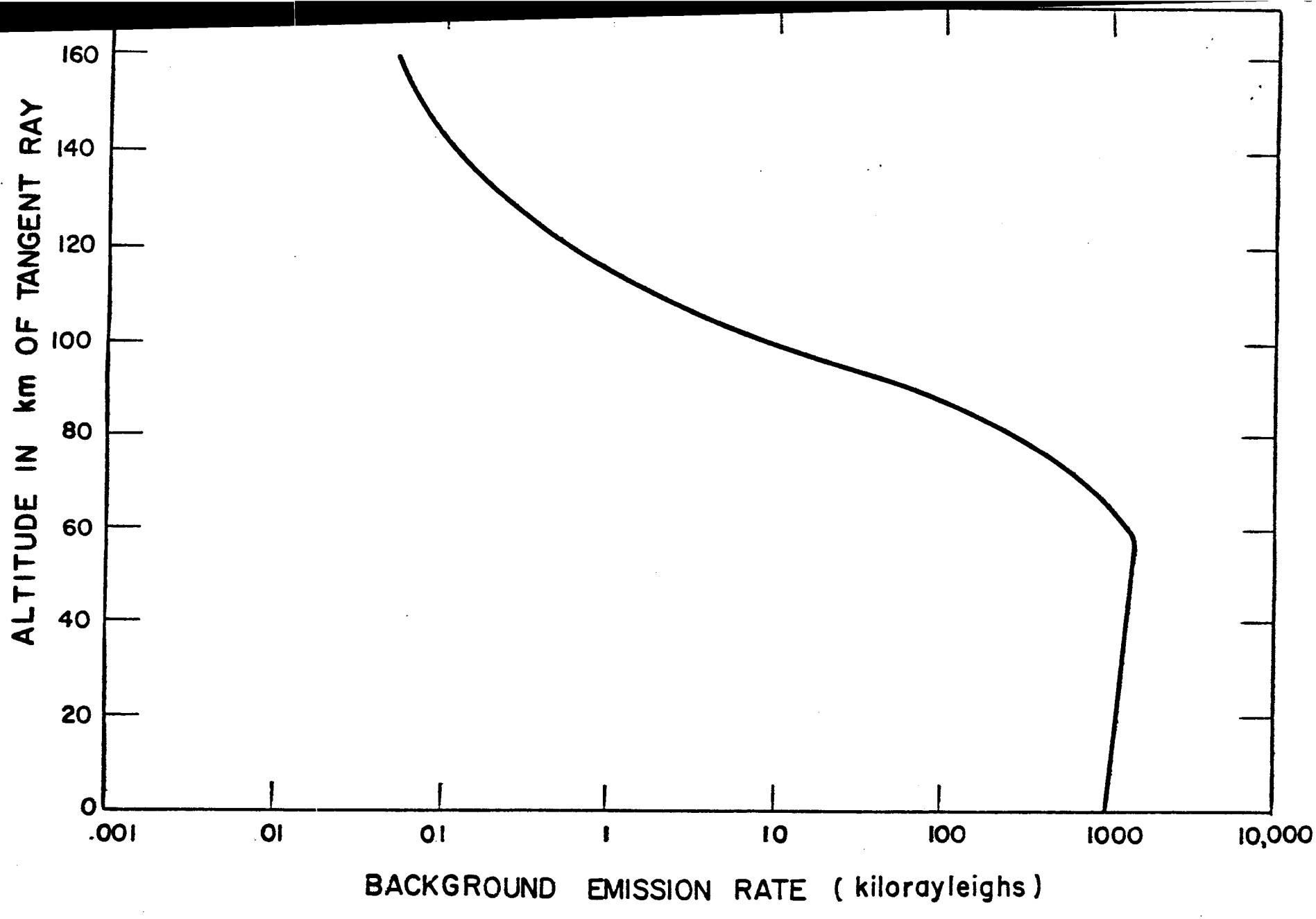
ALTITUDE IN km OF TANGENT RAY
160
140
120
100
80
60
40
20
0
.001
.01
0.1
1
10
100
1000
10,000
BACKGROUND EMISSION RATE (kilorayleighs)

Figure 28

of the background emission curve of Figure 27 is indicative of the expected photographic format results. It can be seen that under proper exposure (on the straight portion of the gamma curve), a rather sharp break in film blackness will be experienced at about the 60 km level. Specifically, at an angular excursion on the film of about one degree above this level, the intensity can be seen to decrease by about two orders of magnitude. Finally, the background intensity at 80 km is at most only about an order of magnitude less than the values at lower tangent altitudes. As such, a considerable advantage is gained by operation in the $\lambda\lambda$ 2250 to 2450Å spectral region rather than in the visible region where the ratio of background intensities at 80 km to that at the Earth's surface could be as much as three orders of magnitude. Operation in the visible region introduces problems involving the capability of the system to maintain proper exposure over the broad intensity range as well as secondary scattering effects from the relatively-bright surface region on the photographic film.

(b) Signal characteristics. In this section, estimated signal intensities from a typical solar-illuminated noctilucent cloud are calculated to determine the feasibility of performing successful photographic observations against the pertinent background discussed above. In the present analysis, the following assumptions have been made: (a) the observation line-of-sight is tangent to the mean resident altitude of noctilucent clouds, i.e. 80 km; (b) spherically-shaped cloud particles and distributed according to the average of the two distributions shown in Figure 23;

and (c) a cloud thickness of 2 km with a uniform particle number density of 50 cm^{-3} resulting in a vertical column count of 10^7 cm^{-2} which is representative of the in situ rocket collection results of Hemenway et al.[172] In the above tangent ray geometry, an enhancement factor of 160 is realized for the ray penetrating the cloud at an altitude of 80 km. In other words, the effective tangent ray column count is N_T = 1.6×10^9 particles/cm^2. Estimates of the Mie scattering efficiency must now be calculated for the assumed solar-illuminated noctilucent cloud configuration. For the present purpose, an approximation due to Penndorf[178] is employed involving the angular Mie scattering cross section, defined by

$$\sigma_\theta(x,m,\theta) = \pi r^2 I_\theta(x,m,\theta) \quad (cm^2\text{-ster}^{-1}) \tag{15}$$

where

$x = 2\pi r/\lambda$ = scattering parameter

r = radius of sphere

λ = wavelength

m = refractive index of the sphere = $n - ik$

θ = angle between the directions of the incident and scattered rays.

In addition,

$$I_\theta(x,m,\theta) = \frac{1}{2\pi x^2} [I_1(x,m,\theta) + I_2(x,m,\theta)] \quad (ster^{-1}) \tag{16}$$

where I_1 and I_2 are termed the intensity functions. Physically, I_1 and I_2 are proportional to the intensity of a plane polarized wave having its

electric vector perpendicular and parallel to the plane of scattering, respectively. The I_1 and I_2 values can be computed by a rather involved technique involving Ricatti-Bessel functions and associated Legendre polynomials of the first order. For the present purpose, employing a wavelength of 2000Å and the average of the measured r-value distributions,[172] the calculations were performed for $0 \leq \theta \leq 180^{\circ}$.

The selection of an appropriate value of the refractive index for typical noctilucent cloud particles must now be made. Recently, VUV reflectivity measurements were performed by this laboratory for a number of materials as a function of incidence angle. From these data, the real and imaginary components of the refractive index were calculated and the results, which are directly applicable to the present problem, are presented in Table 4 below.

TABLE 4

MEASURED REFRACTIVE INDICES FOR SEVERAL SELECTED MATERIALS FOR $\lambda \cong 2000$Å

Material	n-value	k-value
nickel	1.04	0.80
304 stainless steel	1.30	1.05
50-52 aluminum	0.72	0.98
sapphire	1.80	0.20
glass	1.53	0.26
quartz	1.46	0.43

The Mie calculations can be performed most conveniently for indices of refraction of 1 - i and 1 - i/2. Furthermore, similar results are obtained for varying indices of refraction of

0.8 - i/2 to 2.0 - i/10. As such, from the data of Table 4, the calculated curves can be considered representative and of sufficient accuracy for the present requirements. The computed angular scattering cross sections are shown in Figure 29 as a function of scattering angles which vary between 20^{o} and 180^{o} for the cases of m = 1 - i and 1 - i/2 and for the measured particle size distribution. The effect of increasing the real component of the refractive index is to accentuate the maxima and minima at the extreme scattering angles whereas an increased imaginary component generally results in curve smoothing. Notwithstanding, the results of Figure 29 indicate that for scattering angles between 90 and 180 degrees, the two curves are relatively flat so that a representative cross-section value of about 10^{-12} cm^2-$ster^{-1}$ can be selected. At lower scattering angles between 20 and 40 degrees, a more representative cross section of about 10^{-11} cm^2-$ster^{-1}$ appears to be appropriate.

Having evaluated the required scattering parameters, it is now propitious to estimate the signal intensity from a representative noctilucent cloud under the assumed geometrical conditions. Thus, the pertinent signal intensity is given by $4\pi\ \sigma_\theta\ N_T\ \Phi\ \Delta\lambda$ where Φ is the incident solar flux (6×10^{11} photons/cm^2-sec-Å). Thus, for the selected overhead sun conditions and tangent ray look angle geometry where a σ_θ-value of 10^{-12} cm^2-$ster^{-1}$ is appropriate, the signal intensity is given by

$$4\pi \text{ ster} \cdot \frac{1 \times 10^{-12} \text{ cm}^2}{\text{ster-particle}} \cdot 1.6 \times 10^{9} \text{ particles-cm}^2 \cdot \frac{6 \times 10^{11} \text{ photons}}{\text{cm}^2\text{-sec-Å}} \cdot 200\text{Å} =$$

$$2.4 \times 10^{12} \frac{\text{photons}}{\text{cm}^2\text{-sec}}.$$

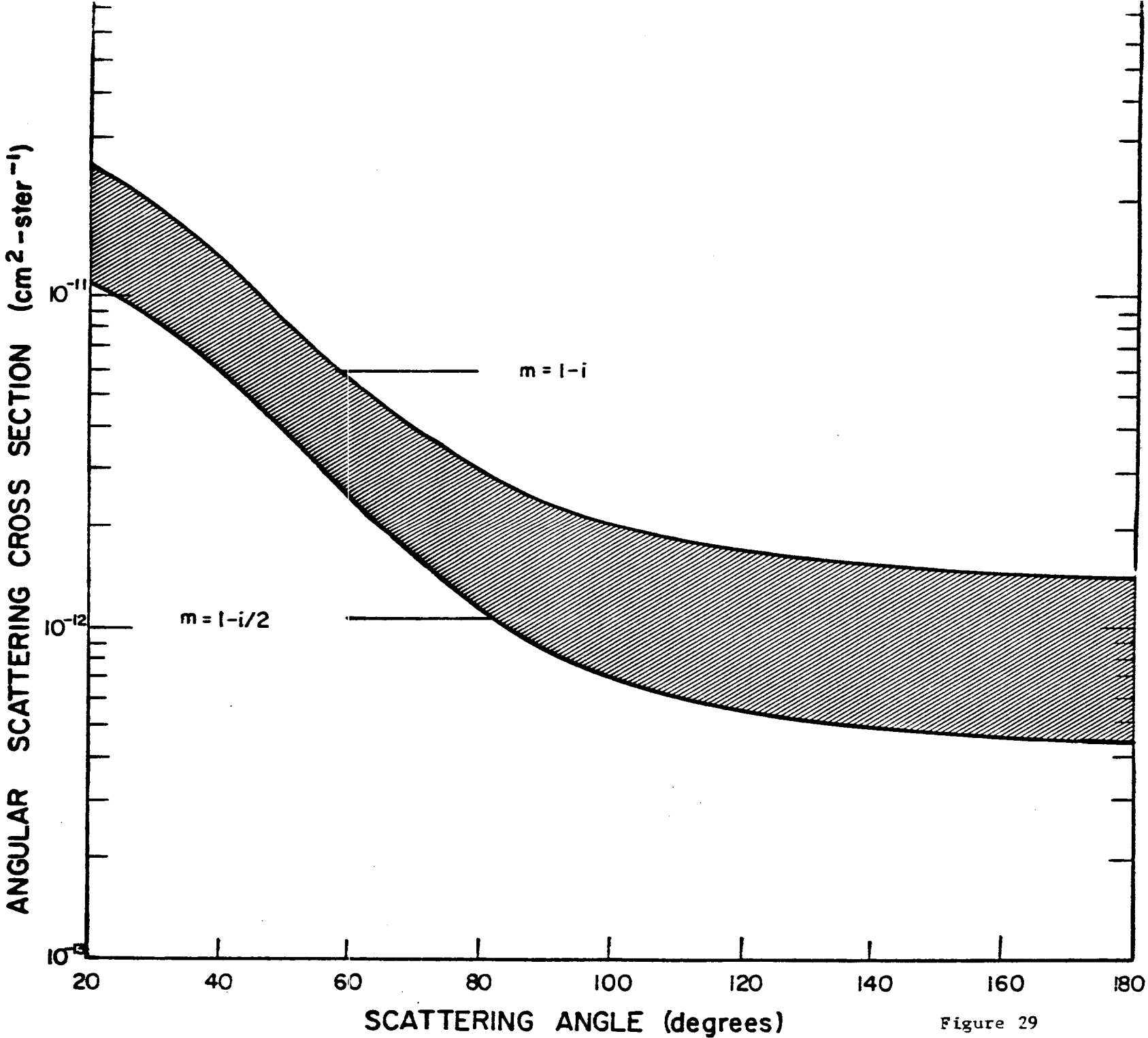
ANGULAR SCATTERING CROSS SECTION (cm²-ster⁻¹)
10⁻¹¹
10⁻¹²
10⁻¹³
m = 1-i
m = 1-i/2
20
40
60
80
100
120
140
160
180
SCATTERING ANGLE (degrees)

Figure 29

At the more forward scattering angles, a signal intensity of 2.4×10^{13} photons cm^{-2} sec^{-1} would be pertinent. For cogent comparison of these signal values with the background data shown in Figures 27 and 28, it should be noted that these signal levels are 2400 and 24,000 kR, respectively (where 1 kR = 10^9 photons cm^{-2} sec^{-1}), over the spectral bandpass of the system. Reference to Figure 27 indicates that the largest background emission rate is about 1500 kR. As such, it appears that if a fully-developed noctilucent cloud is observed photographically, it would represent the brightest feature on the entire film format. The following section contains a discussion of the optimum exposure selection to obtain useful experimental results.

(5) Photographic detection capability

The present discussion includes a description of the techniques employed to estimate the range of exposure times to optimize the probability of successfully photographing terrestrial dust against the background intensities presented in Figures 27 and 28. For the present purpose, it is appropriate to derive exposure times predicated on the background intensities against which such signals must be observed.

The general features of the ultraviolet photographic system were discussed previously. Unfortunately, characteristic curves for Kodak IO film are not available for spectral regions other than the visible. In addition, there is no established, reliable technique for extrapolating the available visible data to the ultraviolet spectral region

of interest here. This lack of basic film data necessitated resorting to an alternative scheme to derive the exposure time estimates.

In this regard, Dr. Henize[173] has employed the present imaging system (less the interference filter) in a previous Gemini experiment to perform ultraviolet stellar photography. He utilized a predispersing element (for which a transmissivity of 100 percent is assumed for the present purpose) to generate a stellar spectrum on the film format which measured 1 mm in height with a mean dispersion of about 180Å per mm. Thus, the stellar spectrum corresponding to the bandpass of the present experiment was represented by an image area of about 1 mm square. Furthermore, Dr. Henize has advised that for this spectral region, a suitable film density was obtained using a 0.5-second exposure time to photograph a -0.8 magnitude AO star. With the above information, it is possible to calculate exposure times based on a normalized value derived in the following discussion.

Over the present experimental bandpass, a -0.8 magnitude AO star yields an irradiance, I_r, of about 3×10^5 photons cm^{-2} sec^{-1}.[179] Furthermore, for any imaging system,

$$B_I = T B_S \tag{17a}$$

or

$$\frac{B_I t}{T} = B_S t \tag{17b}$$

where

B_I = the surface brightness, in units of photons cm^{-2} sec^{-1} $ster^{-1}$, of the image in the focal plane

T = the optical transmission factor

B_S = the surface brightness, in units of photons cm^{-2} sec^{-1} $ster^{-1}$, of the source

t = exposure time.

The $B_I t/T$-value of Equation (17b) can be evaluated from the data supplied by Dr. Henize. For this purpose, it is convenient to express $B_I t/T$ in terms of the irradiance by

$$\frac{B_I\ t}{T} = \frac{I_r\ f^2\ t}{a\ T} = 1.6 \times 10^{10} \text{ photons cm}^{-2}$$

where, in accordance with the data supplied by Dr. Henize,

I_r = irradiance due to a -0.8 magnitude AO star, 3×10^5 photons cm^{-2} sec^{-1}

f = camera focal length, 7.3 cm

t = exposure time, 0.5 second

a = image area, 1 mm^2 or 10^{-2} cm^2

T = mean transmission, 5 percent (as indicated in Figure 25); for this case, the camera transmission factors are equivalent.

Since $B_S = I_S/4\pi$, where I_S represents the source emission rate, it follows that

$$I_S\ t = 4\pi(1.6 \times 10^{10}) = 2.2 \times 10^{11} \text{ photons cm}^{-2}. \qquad (18)$$

The appropriate background emission rates shown in Figures 27 and 28 are now employed to derive corresponding exposure times as a function of tangential altitude, as shown in Figure 30, between 0 and 120 km. These data can be applied to the problem of deriving a range of recommended exposure times; however, several additional factors must be considered first as described below.

It is safe to assume that a signal intensity amounting to about 10 percent of the background would result in sufficient contrast for its detection on the film format. This criterion, in fact, establishes the ultimate detection capability for the present imaging system. Accordingly, a definition of minimum signal detection capability with altitude can be obtained directly by reference to Figures 27 and 28 by a corresponding reduction in the plotted values by a factor of 10. Additionally, the exposure times to achieve the indicated capability for any specific altitude are essentially those required to successfully photograph the background so that the values of Figure 30 pertain. It is evident that a questionable practicality exists in the operational performance of the present experiment using the long exposure times indicated for the higher altitudes above 100 km. On the other hand, if a faster system were employed, this difficulty would be avoided. For the present experimental goals, it is instructive to consider the specific case involving the observation of a fully-developed noctilucent cloud at 80 km.

In Figure 31, the solid curve refers to the expected signal intensity from a solar-illuminated, fully-developed

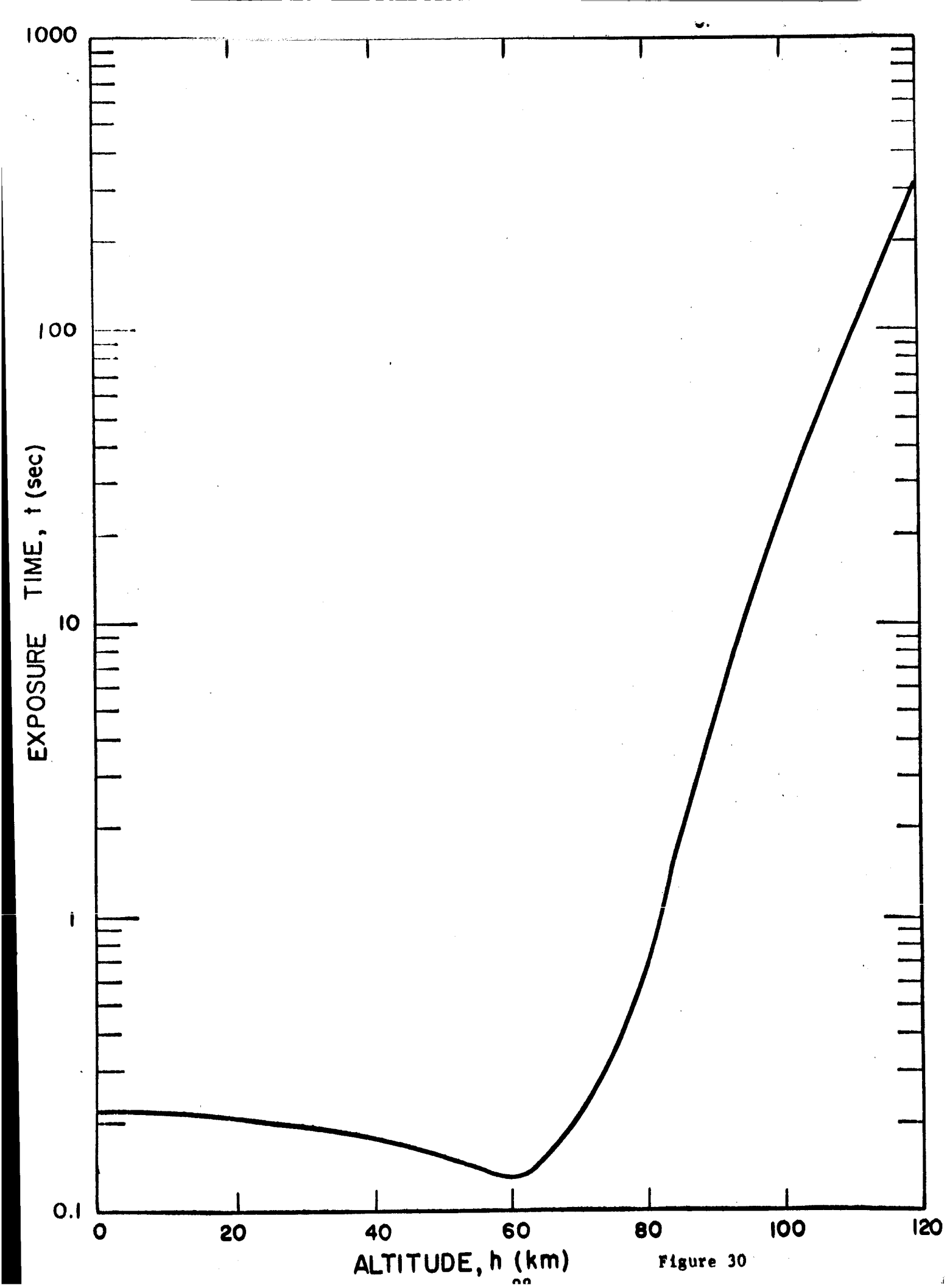
1000
100
10
1
0.1
EXPOSURE TIME, t (sec)
0
20
40
60
80
100
120
ALTITUDE, h (km)

Figure 30

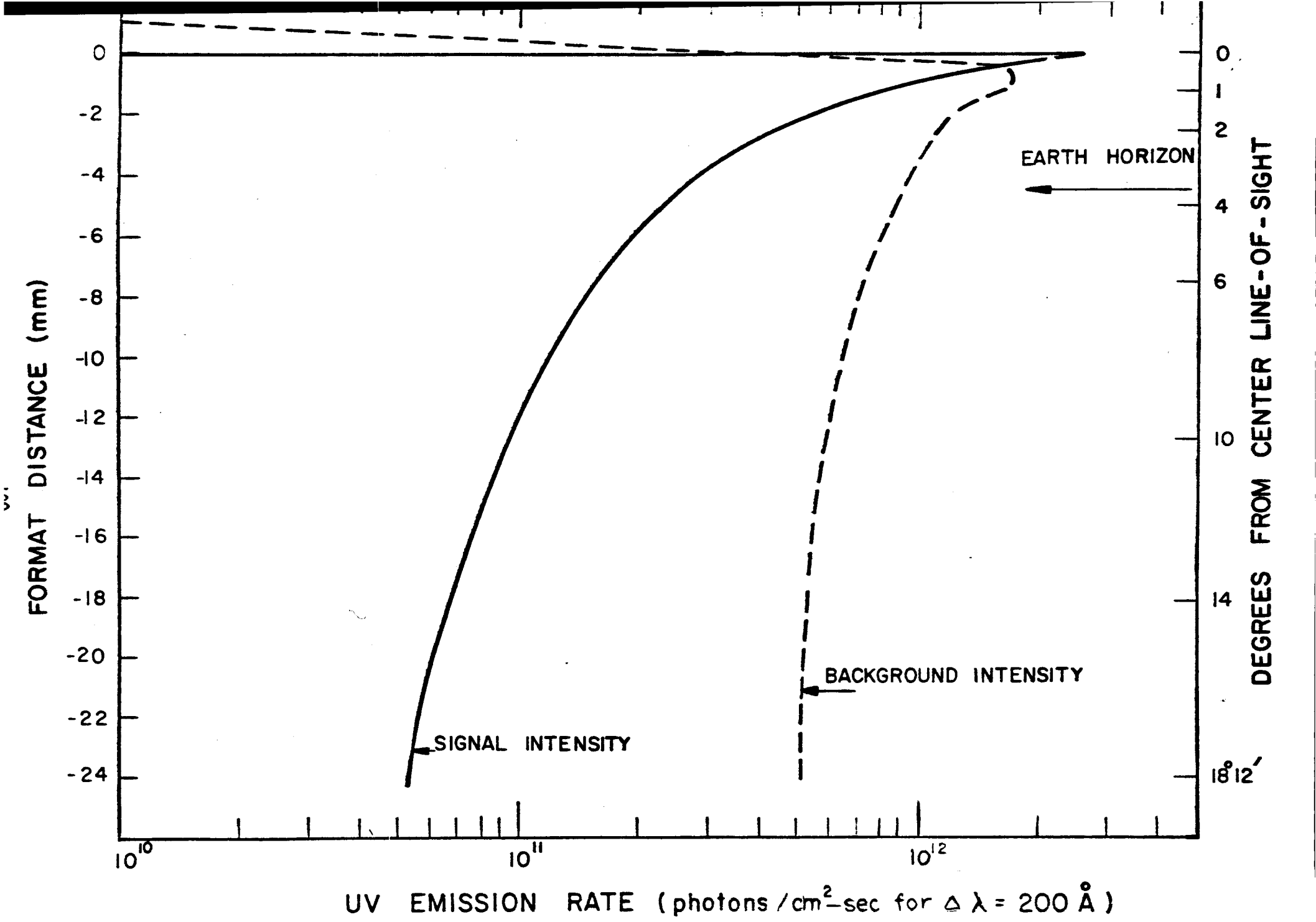
FORMAT DISTANCE (mm)
0
-2
-4
-6
-8
-10
-12
-14
-16
-18
-20
-22
-24
EARTH HORIZON
BACKGROUND INTENSITY
SIGNAL INTENSITY
DEGREES FROM CENTER LINE-OF-SIGHT
0
1
2
4
6
10
14
18°12'
10^{10}
10^{11}
10^{12}
UV EMISSION RATE (photons/cm^2-sec for $\Delta\lambda$ = 200 Å)

Figure 31

(50 particles cm^{-3} with a 2-km thickness located at 80 km) noctilucent cloud as a function of viewing angle and film format. The dotted curve is a duplicate of Figure 27 and represents the background intensity as a function of the same parameters. This figure can be employed to discuss a number of pertinent facts. First, the data indicate that at the 80 km level it would be possible to detect a signal intensity of only about 1.3×10^{10} photons cm^{-2} sec^{-1} (10 percent of the background intensity). Since the expected signal amounts to 2.4×10^{12} photons cm^{-2} sec^{-1}, it is clear that the photographic system is capable of imaging significantly under-developed noctilucent clouds to the extent wherein the local number particle density is much less than 1 cm^{-3}. Another feature made evident by the figure is that a fully-developed noctilucent cloud would appear as the brightest feature on the entire film format. It should also be noted that the above cloud can be detected photographically for viewing angles as low as -18^{o} from center line-of-sight. The latter angle is well below the real Earth horizon which, incidentally, cannot be distinguished due to absorption by atmospheric ozone. All the above factors indicate that fully-developed noctilucent clouds would be readily detectable on the film format display. Additionally, further information on the physical characteristics, geographical extent, inhomogeneities, wave structure, etc., can be derived against the near ideal, homogeneous, constant background level. In this manner, it can be anticipated that the characteristic noctilucent cloud structure will be easily distinguished on the film format. Coupled with this capability is the requirement of utilizing relatively-short exposure times to minimize distortion due to the movements of the astronaut and the vehicle.

The data in Figure 30 suggest a recommended exposure-time range between about 0.1 second to more than 100 seconds. The final time range selection is predicated on the scientific goals of the experiment. For example, it has been shown that for low-altitude observations of fully-developed noctilucent clouds, it would be propitious to employ relatively-short exposure times between a few seconds and about 0.1 second. On the other hand, to achieve optimum capability at the higher altitudes, longer exposure times are indicated. Thus, if the major scientific objective is to photograph high-altitude dust such as reported by Fiocco et al.[169] and implied by the data of Mikirov,[180] it would be an experimental requirement to employ the indicated relatively-long exposures since the local number densities are expected to be low. Accordingly, even to establish meaningful upper-limit particulate-matter number densities, the indicated exposures would be required in spite of the fact that a corresponding degradation of imaging capability would be necessarily involved.

As a final comment, it is appropriate here to point out a significant advantage of performing this experiment in the region λλ 2250 to 2450Å. If the present experiment were performed in the visible region, there would be little or no capability of observing the physical characteristics, geographical extent, wavelike structure, etc., of a noctilucent cloud. On the other hand, the minimum detectable photographic capability is enhanced compared to that in the ultraviolet. To illustrate this point, it can be shown that for the assumed particle distribution, the Mie scattering efficiency in the visible region (i.e., 5000Å)

is essentially equivalent to the value calculated in the ultraviolet. In addition, at least within a factor of 2, the Rayleigh scattering cross section at 5000Å is about 20 times less than the value at 2300Å. On this basis, it would appear that more optimum experimental conditions prevail in the visible region. The fallacy in the above argument is illustrated in Figure 32 where the signal and background emission rates (for $\Delta\lambda$ = 200Å) in the visible are plotted against degrees from center line-of-sight and format distance. The solid curve depicts the signal intensity whereas the dotted curve refers to the background intensity due only to Rayleigh scattering, which represents a somewhat conservative estimate. On comparing these data with those if Figure 31, it is apparent that the signal-to-background ratio is greater in the visible region than in the far ultraviolet over the altitude region corresponding to center line-of-sight observations (80 km) to as low as about -1.0 degrees (50 km). Accordingly, if the purpose of the experiment is confined to the detection of noctilucent clouds, operation in the visible rather than in the far ultraviolet region appears to be more efficient. However, employing the detection criterion that the signal level must be 10 percent of the background, the data of Figure 32 indicate that even a fully-developed noctilucent cloud could not be detected below about 40 km. Thus, in the visible region, the noctilucent cloud image on the film format would result in a relatively-narrow line (i.e., 2 mm in height) containing essentially no information concerning the extent, dimensions, structure, or other characteristics of the clouds, whereas in the ultraviolet, where the cloud image covers the entire bottom portion of the film format, the

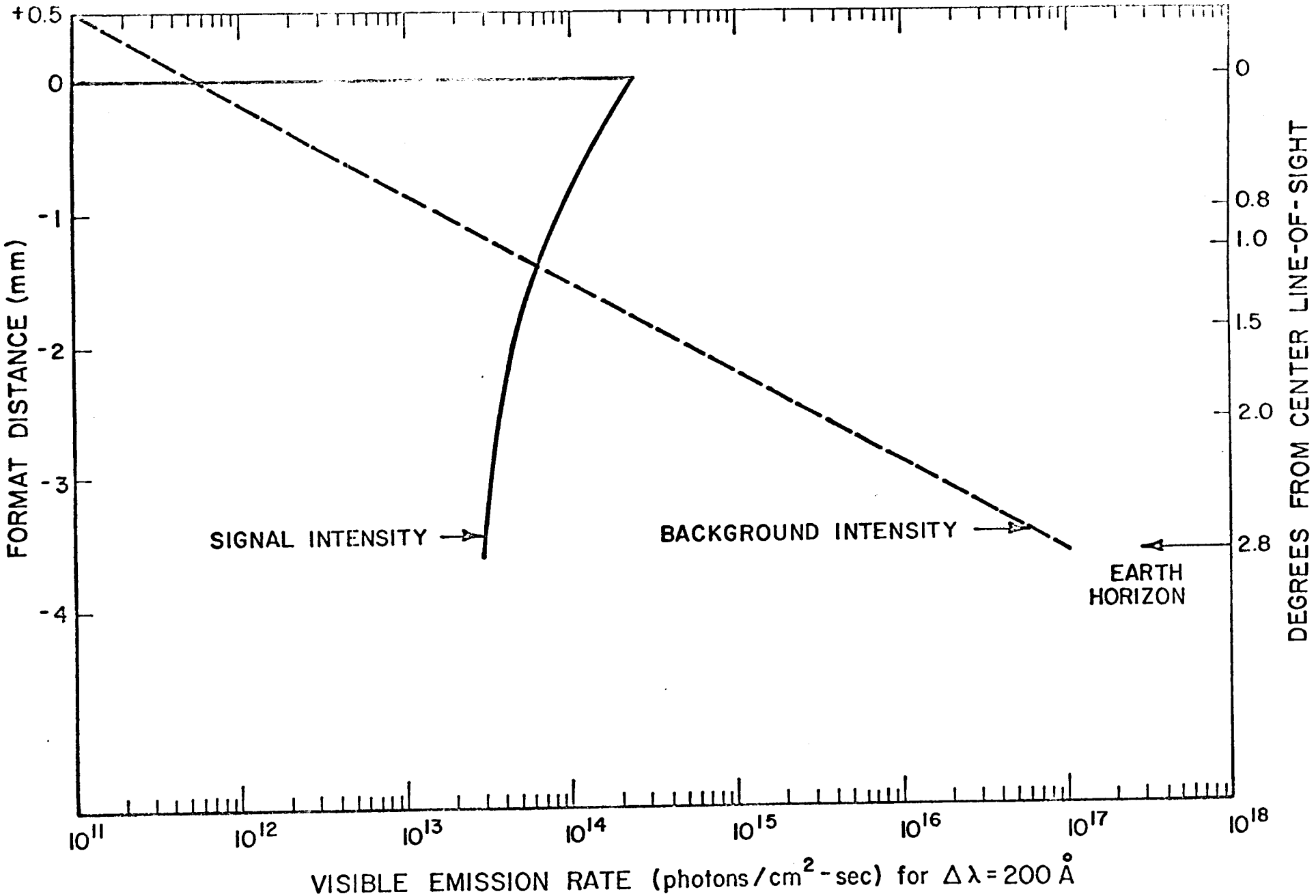
+0.5
0
-1
-2
-3
-4
FORMAT DISTANCE (mm)
0
0.8
1.0
1.5
2.0
2.8
DEGREES FROM CENTER LINE-OF-SIGHT
SIGNAL INTENSITY
BACKGROUND INTENSITY
EARTH HORIZON
10^{11}
10^{12}
10^{13}
10^{14}
10^{15}
10^{16}
10^{17}
10^{18}
VISIBLE EMISSION RATE (photons/cm^2-sec) for $\Delta\lambda = 200$ Å

Figure 32

above physical characteristic cloud data would be easily obtained. Furthermore, it should be noted that a significant degradation in experimental capability in the visible region can be expected due to the high instrumental scattered light level. As such, it is concluded that photographic observation of noctilucent clouds is performed more efficiently in the spectral region under investigation, i.e., 2250 to 2450Å.

(6) Brief summary of recommended experimental format

The foregoing discussions have demonstrated the feasibility of photographically observing noctilucent clouds in the Earth's atmosphere in the spectral region from 2250 to 2450Å. As discussed previously, the optical system to be employed in the present experiment does not represent an optimum selection. Notwithstanding, it has been shown that, for a noctilucent cloud situated at 80 km and consisting of a uniform distribution of 50 particles cm^{-3} over a 2-km height interval, the resulting photographic image obtained over the spectral bandpass represents the brightest feature on the entire film format. Furthermore, it has been shown that somewhat underdeveloped noctilucent clouds (containing less than one particle cm^{-3}) can be observed photographically in the present experimental configuration. Finally, for the case of a fully-developed cloud, it is possible to observe pertinent physical characteristics, geographical extent, wave-like structure, etc.

Other sources of terrestrial dust, such as those reported by Fiocco, can only be observed if they exist in sufficient quantity. Although no quantitative information is available in this regard, upper limit particle number density values could be established as a function of altitude from the results of the present experiment if the dust exists in relatively-well-defined belt-like structured form. It is also interesting to note that since altitudes below about 70 km do not contribute, a relatively-homogeneous and low-level background situation is anticipated. It has also been shown that the horizon is not imaged in the present experiment due to ozone absorption. It is expected that orientation information will be available by the inclusion of specific stellar images within the field of view to facilitate the data reduction and analysis efforts. In this regard, Ed Barr[174] has supplied the following pertinent information regarding the ultraviolet filter employed. For 10-degree deviations from center line-of-sight observations, there is no measurable loss in filter transmissivity and the center band position shift amounts to only about 12Å. Furthermore, even for 20-degree deviations from center line-of-sight observations, there is still no significant loss in filter transmissivity but the center band position shift can amount to as much as 50Å. In any case, this information makes it evident that there is no significant information degradation throughout the entire film format for the present optical system.

Finally, it can be shown that radiation due to such other sources as fluorescence, scattering, airglow, etc., associated

with solar-illuminated atomic and molecular atmospheric constituents does not constitute a serious interference problem since these emissions are generally weak and confined to extremely-narrow wavelength intervals as compared to the experimental spectral bandpass.

(7) Sunrise experiment calculations

Prior to the Gemini XII flight, it was decided on the basis of the results of the preceding investigation that a more appropriate trade-off experiment would involve atmospheric dust observations at sunrise. As discussed previously in the overhead sun situation, although the entire film format would contain useful data as defined by the 10 percent contrast criterion, it was felt that higher contrast information could be obtained during sunrise conditions.

On the basis of preliminary calculations, it has been verified that higher contrast observations could be performed during sunrise, albeit over a limited portion of the available film format. The results of a representative sunrise calculation are shown in Figure 33 for a solar depression angle of 4^{o}. These can be compared with the results of the overhead sun calculation shown in Figure 31. Although the total amount of information is clearly more limited during sunrise than in the overhead sun situation, the greater contrast for the tangent ray altitude region between about 60 and 80 km is apparent. Since the Gemini XII orbit was confined to relatively-low latitudes as discussed previously, it was felt that an initial yes-no answer on the presence of dust in the Earth's atmosphere in the vicinity of 80 km would be more

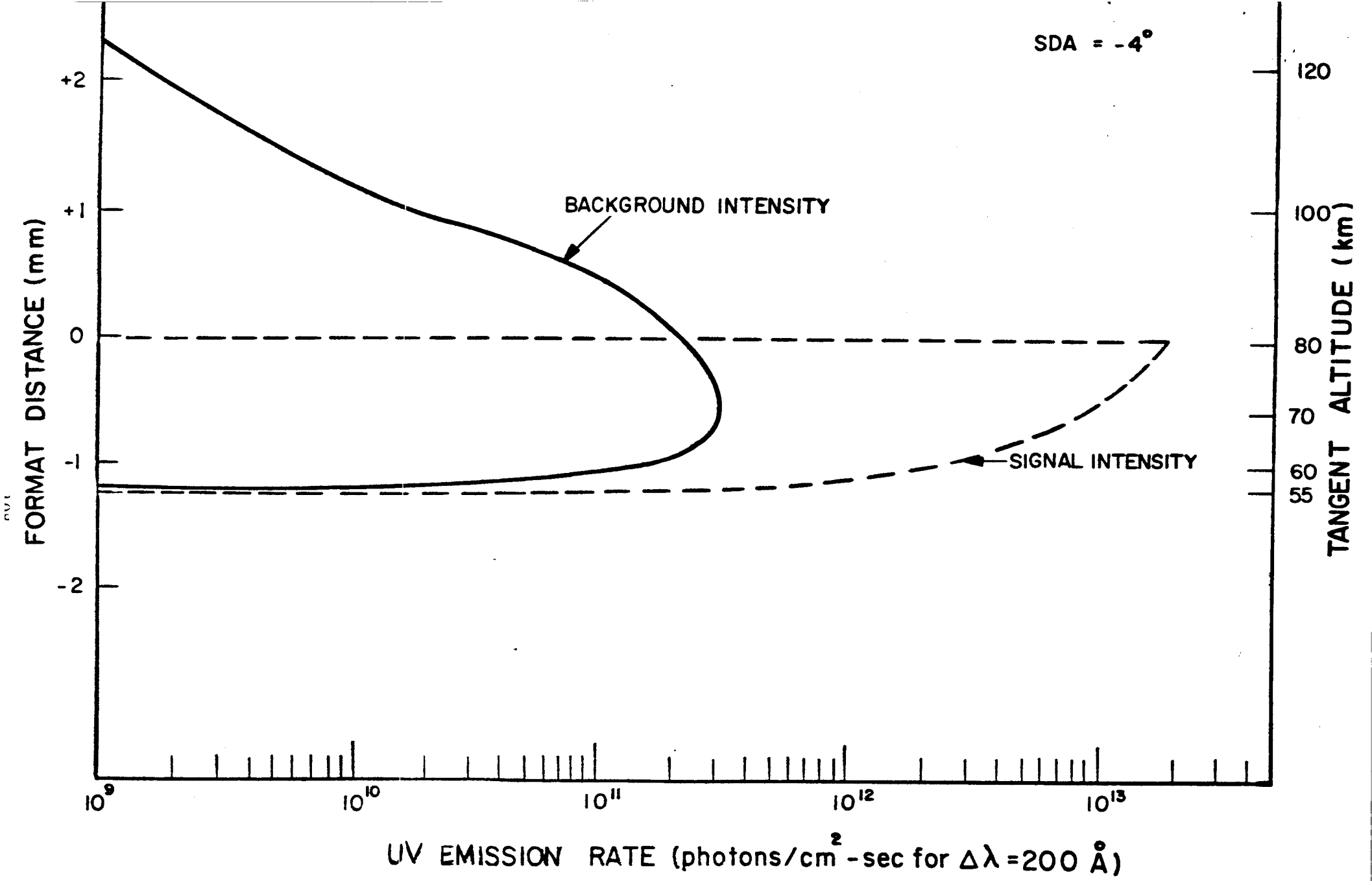
SDA = -4°
BACKGROUND INTENSITY
SIGNAL INTENSITY
FORMAT DISTANCE (mm)
+2
+1
0
-1
-2
TANGENT ALTITUDE (km)
120
100
80
70
60
55
10^9
10^{10}
10^{11}
10^{12}
10^{13}
UV EMISSION RATE (photons/cm^2-sec for $\Delta\lambda$ = 200 Å)

Figure 33

worthwhile than the overhead sun experiment. The calculation techniques employed to derive the results of Figure 33 are similar to those discussed for the overhead sun analysis. It should be noted that the higher Mie scattering cross section for forward scattering was employed in the sunrise case, i.e., $\sigma_\theta = 4\pi \times 10^{-11}$ cm^2/ster-particle. The sunrise results also indicate strongly decreasing signal and background intensities below a tangent ray altitude of about 60 km due to the predominance of ozone absorption. Clearly, with the contrast indicated in Figure 33, the presence of noctilucent clouds at relatively-low latitudes should be determinable with relatively-high sensitivity.

2. Experimental Investigations in Planetary Aeronomy

In the area of experimental planetary aeronomy, the following parameters will be derived from laboratory investigations for selected atmospheric gases: (a) the efficiency of visible, UV, and VUV fluorescence due to electron impact interaction, (b) the VUV photon scattering cross sections, and (c) the efficiency of visible UV and VUV fluorescence due to alpha particle interactions.

During the current reporting period, preliminary work has been performed under Items (a) and (b) as reported below.

a. Electron impact studies

A brief review has been performed on the VUV fluorescence of atmospheric gases due to electron bombardment. The results indicate that little useful information exists regarding this important process.

For this reason, a systematic experimental study is being planned to obtain the empirical data required to explain some recent VUV rocket airglow observations. At present, the experimental apparatus to be employed in this experimental investigation has been designed as shown in Figure 34. In brief, the arrangement consists of a Pierce-type electron gun (Ve B-6 from Veeco Instrument Company) with a perveance of $\sim 10^{-7}$ $A/V^{3/2}$ which can deliver about 1 mA current at about 400 eV. It is planned to maintain pressures in the electron gun section of between 10^{-4} and 10^{-5} torr and in the collision chamber between 10^{-2} and 10^{-3} torr. The variation of the intensity of various spectral features will be investigated as a function of electron energy and pressure. The above laboratory data will be utilized to obtain information regarding the excitation function and to delineate the effect of secondary processes; e.g., excitation by the secondary electrons, quenching, etc.

The following atmospheric gases have been selected for the study: nitrogen, carbon monoxide, carbon dioxide, and oxygen.

b. Measurement of VUV photon scattering cross sections

The measurement of VUV scattering cross sections involving monochromatic light requires a highly-sensitive photon detection probe. For this purpose, photon counter techniques will be employed, which offer a significant advantage over a Geiger counter, since a broader spectral range can be examined. During the current reporting period, the appropriate instrumentation has been designed and fabricated, and the

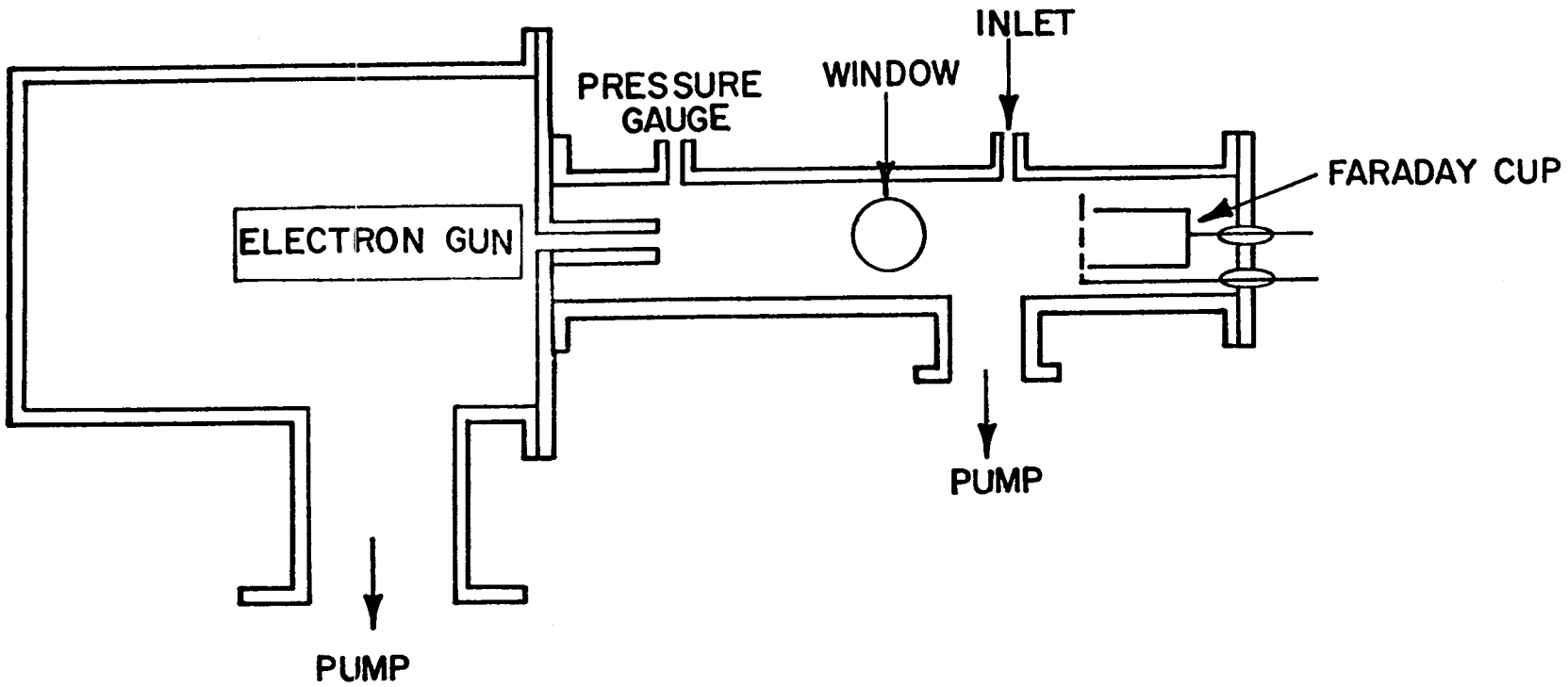

Figure 34. Experimental arrangement for the study of spectra excited by electron bombardment.

tedious task of calibration has been initiated. In addition, a scattering chamber has been designed and fabricated, and mounted on the ½-meter Seya monochromator. Initial control measurements have been performed wherein intentionally-weak monochromatic signals have been recorded at the exit slit using photon counting techniques in conjunction with both EMI and EMR photomultiplier tubes. These preliminary experiments provide valuable data which will be employed to optimize the final pulse circuit design and to determine the absolute sensitivity of this system. It is anticipated that this phase will be completed within the subsequent reporting period so that some preliminary VUV photon scattering cross-section measurements may be included in the next report.

III. OTHER PERTINENT INFORMATION

During the current reporting period, Dr. P. Warneck presented a paper entitled "Reactions of ^1D Oxygen Atoms" at the 152nd Meeting of the American Chemical Society in New York City on 12-14 September 1966. This paper was received enthusiastically on the basis of a detailed discussion with Edward Bair (Indiana University) who is also active in $O(^1D)$ reaction kinetics. Other presented papers in photochemistry included work by McNesby's group on the flash photolysis of methane, and by Stief and deCarlo on the photolysis of ammonia and hydrazine. Of particular interest to our work on ion-neutral reactions was a symposium on this subject, providing opportunity for discussions with Drs. Paulson, Giese, Lindholm, Calcote, and Franklin, during which new results in this area were disclosed.

IV. QUARTERLY PROGRESS REPORT FOR HOURS WORKED IN THE PERIOD 17 SEPTEMBER THROUGH 30 NOVEMBER 1966

In compliance with the requirements of the subject contract, the following is an integrated tabulation of total hours worked by labor category and grade.

Labor Category	Labor Grade	Total Hours
*Junior Key Punch Operator	1	---
*Junior Technician	2	176
*Technician Experimental Machinist	3	185
*Senior Technician Senior Experimental Machinist	4	222
*Junior Scientist Junior Engineer	5	332
*Scientist Engineer	6	1016
Senior Scientist Senior Engineer	7	621
Staff Scientist	8	670
Principal Scientist	9	432
Group Scientist	10	173

*and other equivalent categories

REFERENCES

1. Quarterly Progress Report No. 6, Contract No. NASW-1283, GCA Corporation, Bedford, Mass. (September 1966).
2. Bates, D. R. and H.S.W. Massey, "The Basic Reactions in the Upper Atmosphere II. The Theory of Recombination in the Ionized Layers," Proc. Roy. Soc. (London) A192, 1 (1947).
3. Bates, D. R., "Charge Transfer and Ion-Atom Interchange Collisions," Proc. Phys. Soc. 68, 344 (1955).
4. Bates, D. R. and M. Nicolet, "Ion-Atom Interchange," J. Atmos. Terrest. Phys. 18, 65 (1960); 21, 286 (1961).
5. Norton, R. B., T. E. Van Zandt, and J. S. Dennison, "A Model of the Atmosphere and Ionosphere in the E and F_1 Regions," Proc. Intern. Conf. Ionosphere, Physical Society, London, p. 26 (1963).
6. Nicolet, M. and W. Swider, "Ionospheric Conditions," Planet. Space Sci. 11, 1459 (1963).
7. Dalgarno, A., "Thermal Reactions Involving Charged Particles," Disc. Faraday Soc. 37, 142 (1964).
8. Ferguson, E. E., F. C. Fehsenfeld, P. D. Goldan, and A. L. Schmeltekopf, "Positive Ion-Neutral Reactions in the Ionosphere," J. Geophys. Res. 70, 4323 (1965).
9. Donahue, T. M., "Ionospheric Reaction Rates in the Light of Recent Measurements in the Ionosphere and the Laboratory," Planet. Space Sci. 14, 33 (1966).
10. Johnson, C. Y., "Aeronomic Parameters from Mass Spectrometry," Ann. Geophys. 17, 100 (1961).

REFERENCES (continued)

11. Taylor, H. A. and H. C. Brinton, "Atmospheric Ion Composition Measured Above Wallops Island, Virginia," J. Geophys. Res. 66, 2587 (1961).

12. Holmes, J. C., C. Y. Johnson, and J. M. Young, "Ionospheric Chemistry," Space Res. V, 756 (1965).

13. Paulson, J. F., "Low Energy Charge Exchange and Ion-Molecule Reactions," Ann. Geophys. 20, 75 (1964).

14. Dickinson, P.H.G. and J. Sayers, "Ion Charge-Exchange Reactions in Oxygen Afterglow," Proc. Phys. Soc. 76, 137 (1960).

15. Fehsenfeld, F. C., A. L. Schmeltekopf, P. D. Goldan, H. I. Schiff, and E. E. Ferguson, "Thermal Energy Ion-Neutral Reaction Rates I. Some Reactions of Helium Ions," J. Chem. Phys. 44, 4087 (1966).

16. Goldan, P. D., A. L. Schmeltekopf, F. C. Fehsenfeld, H. I. Schiff, and E. E. Ferguson, "Thermal Energy Ion-Neutral Reactions Rates II. Some Reactions of Ionospheric Interest," J. Chem. Phys. 44, 4095 (1966).

17. Warneck, P., "Studies of Ion-Neutral Reactions by a Photoionization Mass Spectrometer Technique," J. Chem. Phys. (1966) (in press).

18. Poschenrieder, W. and P. Warneck, "Gas Analysis by Photoionization Mass Spectrometry," J. Appl. Phys. 37, 3812 (1966).

19. Galli, A., A. Giardini-Guidoni, and G. G. Volpi, "Ion-Molecule Reactions Leading to NO^+ Formation," J. Chem. Phys. 39, 518 (1963).

20. Fite, N. L., A. Rutherford, W. R. Snow, and V. A. J. Van Lint, "Ion-Neutral Collisions in Afterglows," Disc. Faraday Soc. 33, 264 (1962).

21. Warneck, P., "Ion-Molecule Reaction Rates in an Oxygen-Nitrogen Atmosphere," Final Report, Contract No. NAS5-9161, GCA Technical Report No. 66-13-N, GCA Corporation, Bedford, Massachusetts (1966).

22. Ferguson, E. E., F. C. Fehsenfeld, P. D. Goldan, A. L. Schmeltekopf, and H. I. Schiff, "Laboratory Measurement of the Rate of the Reaction $N_2^+ + O \rightarrow NO^+ + N$ at Thermal Energy," Planet. Space Sci. 13, 823 (1965).

23. Warneck, P., Unpublished data (1966).

24. Fehsenfeld, F. C., P. D. Goldan, A. L. Schmeltekopf, and E. E. Ferguson, "Laboratory Measurements of the Rate of the Reaction $O^+ + O_2 \rightarrow O_2^+ + O$ at Thermal Energy," Planet. Space Sci. 13, 579 (1965).

25. Fehsenfeld, F. C., A. L. Schmeltekopf, and E. E. Ferguson, "Some Measured Rates for Oxygen and Nitrogen Ion-Molecule Reactions of Atmospheric Importance, Including $O^+ + N_2 \rightarrow NO^+ + N$," Planet. Space Sci. 13, 219 (1965).

26. Copsey, M. J., D. Smith, and J. Sayers, "Laboratory Afterglow Studies of O^+ Ions in Helium-Oxygen and Helium-Oxygen-Nitrogen Mixtures," Planet. Space Sci. (1966) (in press).

27. Dalgarno, A., "Thermal Reactions Involving Charged Particles," Disc. Faraday Soc. 37, 142 (1964).

28. Schmeltekopf, A. L., F. C. Fehsenfeld, G. I. Gilman, and E. E. Ferguson, "Reaction of Atomic Oxygen Ions with Vibrationally Excited Nitrogen Molecules," Planet. Space Sci. (1966) (to be published).

29. Boggess, R. L., L. H. Brace, and N. W. Spencer, J. Geophys. Res. 64, 1627 (1959).

30. Spencer, N. W., L. H. Brace, and G. R. Carignan, J. Geophys. Res. 67, 157 (1962).

31. Brace, L. H., N. W. Spencer, and G. R. Carignan, J. Geophys. Res. 68, 5397 (1963).

32. Bowen, P. J., R.L.F. Boyd, C. L. Henderson and A. P. Willmore, Proc. Roy. Soc. (London) A281, 526 (1964).

33. Nagy, A. F., L. H. Brace, G. R. Carignan, and M. Kanal, J. Geophys. Res. 68, 6401 (1963).

34. Brace, L. H., N. W. Spencer and A. Dalgarno, Planet. Space Sci. 13, 647 (1965).

35. Spencer, N. W., L. H. Brace, G. R. Carignan, D. R. Taeusch and H. Niemann, J. Geophys. Res. 70, 2665 (1965).

36. Bowles, K. L., C. R. Ochs and J. L. Green, J. Res. Nat. Bur. Stand. 66D, (1962).

37. Evans, J. V., J. Geophys. Res. 67, 4914 (1962).

38. Evans, J. V., Planet. Space Sci. 13, 1031 (1965).

39. Evans, J. V. and M. Loewenthal, Planet. Space Sci., 12, 915 (1964).

40. Carlson, H. C., J. Geophys. Res. 71, 195 (1966).

41. Hanson, W. B., and F. S. Johnson, Memoires Roy. Soc. Leige, Series 5, 4, 390 (1961).

42. Hanson, W. B., Space Research III, 282 (1963).

43. Dalgarno, A., M. B. McElroy and R. J. Moffett, Planet. Space Sci. 11, 463 (1963).

44. Dalgarno, A., GCA Technical Report No. 63-11-N, GCA Corporation, Bedford, Mass. (1963).

45. Geisler, J. E. and S. A. Bowhill, J. Atmos. Terrest. Phys. 27, 457 (1965).

46. Jacchia, L. G., Res. in Space Sci., Smithsonian Astrophys. Obs., Special Report 170, 53 (1964).

47. Walker, J. C. G., J. Atmos. Sci. 22, 462 (1965).

48. Bates, D. R., Proc. Soy. Soc. London A253, 451 (1959).

49. Stein, J. A. and J. C. G. Walker, J. Atmos. Sci. 22, 11 (1965).

50. Hinteregger, H. E., L. A. Hall, and G. Schmidtke, Space Research V, 1175 (1965).

51. Pokhunkov, A. A., Planet. Space Sci. 11, 441 (1963).

52. Schaefer, E. J., J. Geophys. Res. 68, 1175 (1963).

53. Schaefer, E. J. and M. H. Nichols, Space Research IV, 205 (1964).

54. Schaefer, E. J. and M. H. Nichols, J. Geophys. Res. 69, 4649 (1964).

55. Schaefer, E. J. and J. Brown, J. Geophys. Res. 69, 1455 (1964).

56. Nier, A. O., J. H. Hoffman, C. Y. Johnson, and J. C.Holmes, J. Geophys. Res. 69, 979 (1964).

57. Hedin, A. E., C. P. Avery, and C. D. Tschetter, J. Geophys. Res. 69, 4637 (1964).

58. Hedin, A. E. and A. O. Nier, J. Geophys. Res. 70, 1273 (1965).

59. Reber, C. A. and M. Nicolet, Planet. Space Sci. 13, 617 (1965).

60. Evans, J. V., J. Geophys. Res. 70, 1175 (1965).

61. Dalgarno, A., M. B. McElroy and A. I. Stewart (to be published).

62. Dalgarno, A., R.J.W. Henry, and A. L. Stewart, Planet. Space Sci. 12, 235 (1964).

63. Samson, J.A.R. and R. B. Cairns, Phys. Res. 139, A1403 (1965).

64. Dalgarno, A. and R.J.W. Henry, Proc. Roy. Soc. (London) A288, 521 (1965).

65. Mentzoni, M. H. and R.V.N. Rao, Phys. Rev. Letters 14, 779 (1965).

66. Geltman, S. and K. Takayanagi, Phys. Rev. 143 , 25 (1966).

67. Sampson, D. H. and R. C. Mjolness, Phys. Res. 144, 116 (1966).

68. Chen, J.B.Y., J. Chem. Phys. 40, 3513 (1964).

69. Dalgarno, A. and M. B. McElroy, Planet. Space Sci. 13, 143 (1965).

70. Seaton, M. J., The Airglow and the Aurora, eds. E.P. Armstrong and A. Dalgarno, (Pergamon Press, London)(1956) p. 289.

71. Smith, K., R.J.W. Henry and P.G. Burke, Phys. Rev. 147, 21 (1966).

72. da Rosa, A.V., J. Geophys. Res. (1966) (in press).

73. Spitzer, L., Physics of Fully Ionized Gases, (Interscience Publishers Inc., New York, 1956).

74. Lin, S. C. and B.Kivel, Phys. Rev. 114, 1026 (1959).

75. Neynaber, R. N., L. L. Marino, E. W. Rothe, and S. M. Trujillo, Phys. Rev. 123, No. 1, 148 (1961).

76. Frost, L. S. and A. V. Phelps, Phys. Rev. 127, 1621 (1962).

77. Chanin, L. M., A. V. Phelps, and M. A. Biondi, Phys. Rev. 128, 219 (1962).

78. Dalgarno, A. and J.C.G. Walker, Planet. Space Sci. (1966) (in press).

79. Evans, J. V., J. Geophys. Res. 69, 1436 (1964).

80. Evans, J. V., J. Geophys. Res. 70, 4365 (1965).

81. Smith, L. G., C. A. Accardo, L. H. Weeks and P. J. McKinnon, J. Atmos. Terrest. Phys. 27, 803 (1965).

82. Henry, R.J.W., "Photoionization Cross Sections for C^-, N and O^+," J. Chem. Phys. 44, 4357 (1966).

83. Samson, J.A.R. and R. B. Cairns, J. Opt. Soc. Am. 55, 1035 (1965).

84. Carroll, P. K., R. E. Huffman, J. C. Larrabee and Y. Tanaka, Astrophysical Journal (1966).

85. Huffman, R. E., J. C. Larrabee, and Y. Tanaka, Phys. Rev. Letters 16, 1033 (1966).

86. Cairns, R. B. and J.A.R. Samson, Phys. Rev. 139, 1403 (1965).

87. Boyce, J. C., Rev. Mod. Phys. 13, 1 (1941).

88. Inn, E.C.Y., Spectrochimica Acta 7, 65 (1955).

89. Weissler, G. L., Handbuch der Physik, (Springer-Verlag, Berlin, 1956), Vol. 21.

90. Wilkinson, P. G., J. Mol. Spectry. 6, 1 (1961).

91. Milazzo, G., Pure. Appl. Chem. 4, 135 (1962).

92. Garton, W.R.S., Proc. Fifth Intern. Conf. On Ionization Phenomena in Cases, (North-Holland Publishing Co., Amsterdam, 1962) Vol. II, p. 1884; Advances in Atomic and Molecular Physics, eds. D. R. Bates and I. Estermann (Academic Press, New York, 1966). Vol. 2.

93. Henke, B. L., Advances in X-Ray Analysis 4, 244 (1961) and in X-Ray Optics and X-Ray Microanalysis, eds. H. H. Patee, V. E. Cosslett, and A. Engstrom (Academic Press, New York, 1963) p. 157.

94. Edlen, B., Reports on Progress in Physics (Institute of Physics and the Physical Society, London, SW1, 1963) Vol. 26, p. 181.

95. Uchida, Y., Appl. Optics 3, 799 (1964).

96. McNesby, J. R. and H. Okabe, Advances in Photochemistry, Vol. 3, eds. W. A. Noyes, G. S. Hammond, and J. N. Pitts (Interscience Publishers, New York, 1964) p. 157.

97. Price, W. C., Advances in Spectroscopy, ed. H. W. Thompson, (Academic Press, New York, 1961) Vol. I, p. 56 and Ann. Rev. Phys. Chem. 11, 133 (1960).

98. Samson, J.A.R., Techniques of Vacuum Ultraviolet Spectroscopy (John Wiley and Sons, New York, 1967) and in Advances in Atomic and Molecular Physics, eds. D. R. Bates and I. Estermann (Academic Press, New York, 1966) Vol. 2.

99. Samson, J.A.R. and G. L. Weissler, Methods of Experimental Physics, eds. B. Bederson and W. L. Fite (Academic Press, New York, 1967) Vol. 8.

100. Sandström, A. E., Handbuch der Physik (Springer-Verlag, Berlin, 1957) Vol. 30, p. 78.

101. Tomboulian, D. H., Handbuch der Physik (Springer-Verlag, Berlin, 1957) Vol. 30, p. 246.

102. Vodar, B., Proc. Xth Colloquium Spectry. Intern., eds. E. R. Lippincott and M. Margoshes (Spartan Books, Washington, D. C., 1963) p. 217.

103. Boyd, R.L.F., Space Science Reviews 4, 35 (1965).

104. Proceedings First Intern. Conf. Vacuum UV Radiation Physics, J. Quant. Spectry. Radiat. Transfer 2, 313-728 (1962).

105. Lossing, I. P. and I. Tanaka, J. Chem. Phys. 25, 1031 (1956).

106. Herzog, R.F.K. and F. F. Marmo, J. Chem. Phys. 27, 1202 (1957).

107. Hurzeler, H., M. G. Inghram and J. P. Morrison, J. Chem. Phys. 27, 313 (1958); 28, 76 (1958).

108. Weissler, G. L., J.A.R. Samson, M. Ogawa, and G. R. Cook, J. Opt. Soc. Am. 49, 338 (1959).

109. Murad E. and M. G. Inghram, J. Chem. Phys. 40, 3263 (1964).

110. Dibeler, V. H., R. M. Reese, M. Krauss, J. Chem. Phys. 42, 2045 (1965).

111. Person, J. C., J. Chem. Phys. 43, 2553 (1965).

112. Schoen, R. I., J. Chem. Phys. 37, 2032 (1962).

113. Comes, F. J. and W. Lessman, Z. Naturforsch. 19a, 508 (1964).

114. Schönheit, E., Z. Angew. Phys. 9, 171 (1957). See also Z. Naturforsch. 15a, 841 (1960) and 16a, 1096 (1961).

115. Giese, C., Physikalische Verhandlungen Vol. 1, 2, and 3 (1962). In English.

116. Brehm, B., Z. Naturforsch. 21a, 196 (1966).

117. Warneck, P., J. Chem. Phys. (to be published). See also W. Poschenrieder and P. Warneck, J. Appl. Phys. 37, 2812 (1966).

118. Samson, J.A.R. and G. L. Weissler, Phys. Rev. 137, A381 (1965).

119. Schoen, R. I., Boeing Scientific Research Laboratory, Seattle. Work on the kinetic energies of ions is currently in progress.

120. Vilesov, F. I., B. L. Kurbatov, and A. N. Terenin, Soviet Physics-Doklady 6, 490 (1961) and 6, 883 (1962).

121. Turner, D. W. and M. I. Al-Joboury, J. Chem. Phys. 37, 3007 (1962);

122. Al-Joboury, M. I. and D. W. Turner, J. Chem. Soc. 5141 (1963; 4434 (1964).

123. Al-Joboury, M.I., D. P. May, and D. W. Turner, J. Chem. Soc. 616 (1965); 6350 (1965).

124. Turner, D. W. and D. P. May, J. Chem. Phys. 45, 471 (1966).

125. Radwan, T. N. and D. W. Turner, J. Chem. Soc. 85 (1966).

126. Schoen, R.I., J. Chem. Phys. 40, 1830 (1964).

127. Doolittle, P. H. and R. I. Schoen, Phys. Rev. Letters 14, 348 (1965).

128. Comes, F. J. and H. G. Sälzer, Z. Naturforsch. 19a, 1230 (1964).

129. Blake, A. J. and J. H. Carver, Physics Letters 19, 387 (1965).

130. Samson, J.A.R. and R. B. Cairns, unpublished data.

131. Frost, D. C., C. A. McDowell, and D. A. Vroom, Phys. Rev. Letters 15, 612 (1965).

132. Carlson, T. A. and M. O. Krause, Phys. Rev. 137, A1655 (1965); 140, A1057 (1965).

133. Krause, M. O., Phys. Rev. 140, A1845 (1965).

134. Bethe, H. A., "Quantenmechanik der Ein-und Zwei-Electronprobleme," in Handbuch der Physik (Springer-Verlag, Berlin, 1933). Vol. 24/1.

135. Berkowitz, J. and H. Ehrhardt, Physics Letters 21, 531 (1966).

136. Dalgarno, A., M. B. McElroy, and R. J. Moffett, Planet. Space Sci. 11, 463 (1963) and 13, 143 (1965).

137. Shoen, R. I., D. L. Judge, and G. L. Weissler, in Proc. V Intern. Conf. on "Ionization Phenomena in Gases," ed. H. Maecker (North-Holland Publishing Company, Amsterdam, 1962) Vol. I, p. 25.

138. Judge, D. L., A. L. Morse, and G. L. Weissler, in Proc. VI Intern. Conf. on "Ionization Phenomena in Gases," eds. P. Hubert and E. Cremieu-Alcan (S. E. R. M. A., Paris 8, 1963) Vol. III, p. 373; and Bull. Am. Phys. Soc. 10, 739 (1965); 10, 1210 (1965).

139. Becker, K. H. and K. H. Welge, Z. Naturforsch. 18a, 600 (1963); 19a, 1006 (1964); 20a, 442 (1965); and 20a, 1692 (1965).

140. Beyer, K. D. and K. H. Welge, Z. Naturforsch. 19a, 19 (1964).

141. Tousey, R. J. Opt. Soc. Am. 29, 235 (1939).

142. Hunter, W. R., J. Opt. Soc. Am. 54, 208 (1964); J. de Physique 25, 154 (1964).

143. Cardona, M. and D. L. Greenaway, Phys. Rev. 133, A1685 (1964).

144. Cardona, M. and G. Harbeke, Phys. Rev. 137, A1467 (1965).

145. Ehrenreich, H. and H. R. Phillip, Phys. Rev. 128, 1622 (1962); IEEE Spectrum 2, 162 (1965).

146. Phillip, H. R. and E. A. Taft, Phys. Rev. 127, 159 (1962); 120, 37 (1960); 113, 1005 (1959).

147. Weissler, G. L., et al. (to be published).

148. Walker, W. C., J. Opt. Soc. Am. 52, 223 (1962).

149. Seitz, F., Modern Theory of Solids (McGraw-Hill, New York, 1940) Chapter 17.

150. Pines, D., Solid State Physics, eds. F. Seitz and D. Turnbull (Academic Press, New York, 1955) Vol. 1, p. 367.

151. Walker, W. C., O. P. Rustgi, and G. L. Weissler, J. Opt. Soc. Am. 49, 471 (1959); 51, 1357 (1961).

152. Rustgi, O. P., J. Opt. Soc. Am. 55, 630 (1965).

153. Hunter, W. R., D. W. Angel, and R. Tousey, Appl. Optics 4, 891 (1965).

154. Arakawa, E. T., R. J. Herickhoff, and R. D. Birkhoff, Phys. Rev. Letters 12, 319 (1964); Phys. Rev. 137, A1433 (1965).

155. Walker, W. C., J. Phys. Chem. Solids 24, 1667 (1963).

156. Uchida, Y., R. Kato, and E. Matsui, J. Quant. Spectrosc. Rad. Transfer 2, 589 (1962).

157. Uchida, Y., K. Fukada, and A. Okuda, J. Appl. Phys. 27, 535 (1958); 29, 492 (1960).

158. Onaka, R. and I. Fujita, Phys. Rev. 119, 1597 (1960); J. Phys. Soc. Japan 18, Supplement II, 262 (1963).

159. Walker, W. C. (to be published).

160. Spicer, W. E. and C. N. Berglund, Rev. Sci. Instr. 35, 1665 (1964).

161. Spicer, W. E. and R. E. Simon, Phys. Rev. Letters 9, 385 (1962).

162. Berglund, C. N. and W. E. Spicer, Phys. Rev. 136, A1030 (1964); 136, A1044 (1964).

163. Hunter, W. R. and R. Tousey, Le Journal de Physique 25, 148 (1964).

164. Rustgi, O. P., J. Opt. Soc. Am. 55, 630 (1965).

165. Hass, G., A. Anorg. u. allgem. Chem. 254, 96 (1947).

166. Philipp, H. R. and H. Ehrenreich, J. Appl. Phys. 35, 1416 (1964).

167. Samson, J.A.R. and R. B. Cairns, Rev. Sci. Inst. 36, 19 (1965).

168. Marmo, F. F. and T. C. Degges, "A Satellite Experiment on the Detection of Noctilucent Clouds in the VUV Region," Trans. AGU 47 (No. 1), 126 (March 1966). (47th Annual Meeting AGU, Washington, D. C., April 19-22, 1966; GCA Technical Report No. 66-19-N, Interim Technical Report, Contract No. NASW-1283, GCA Corporation, Bedford, Mass. (September 1966).

169. Fiocco, G. and Colombo, G., J. Geophys. Res. 69, 1795-1803 (1964).

170. "The Study of Noctilucent Clouds," FTD-TT-62-1341, DDC AD-292196, NASA N64-23665, Translation by Air Force Foreign Technology Division, Wright-Patterson Air Force Base, Ohio, 30 October 1962 (date of original Russian material, 1960).

171. Deirmendjian, D. and E. H. Vestine, "Some Remarks on the Nature and Origin of Noctilucent Cloud Particles," Planet. Space Sci. 1, 146 (1959).

172. Hemenway, C. L. et al., Tellus 16, 96-102 (1964).

173. Henize, C., Dearborn Observatory, Evanston, Illinois (private communication).

174. Barr, E., Thin Film Products, Inc., Cambridge, Mass. (private communication).

175. Swider, W. Jr., Planet. Space Sci. 12, 761-782 (1964).

176. Rawcliffe, R. D., Melay, G. E., et al., J. Geophys. Res. 68, 6427 (1963).

177. Handbook of Geophysics for Air Force Designers, Geophysics Research Directorate, Air Force Cambridge Research Laboratories (1957).

178. Penndorf, R., J. Opt. Soc. Am. 52, 402-408 (1962).

179. "Project Celescope," Smithsonian Institution Astrophysical Observatory, Special Report No. 83 (January 1962).

180. Mikirov, A. E., "Investigations of Atmospheric Brightness at Heights of 120-450 km," Space Research V, 815-819 (1965).